An Experimental Investigation on the Aerodynamic Characteristics of NACA 4412 Aerofoil with Curved-Edge Planform

by

Muhammad Nazmul Haque

MASTER OF SCIENCE IN MECHANICAL ENGINEERING

Department of Mechanical Engineering
BANGLADESH UNIVERSITY OF ENGINEERING AND TECHNOLOGY

March, 2015

An Experimental Investigation on the Aerodynamic Characteristics of NACA 4412 Aerofoil with Curved-Edge Planform

by

Muhammad Nazmul Haque

A THESIS SUBMITTED TO THE DEPARTMENT OF MECHANICAL ENGINEERING, BANGLADESH UNIVERSITY OF ENGINEERING AND TECHNOLOGY (BUET) IN PARTIAL FULFILLMENT OF THE REQUIREMENTS FOR THE DEGREE OF MASTER OF SCIENCE IN MECHANICAL ENGINEERING

Department of Mechanical Engineering
BANGLADESH UNIVERSITY OF ENGINEERING AND TECHNOLOGY

March, 2015

The thesis titled **"An Experimental Investigation on the Aerodynamic Characteristics of NACA 4412 Aerofoil with Curved-Edge Planform"** submitted by MUHAMMAD NAZMUL HAQUE, Roll No : 0409102010, Session : April 2009 has been accepted as satisfactory in partial fulfillment of the requirements for the degree of Master of Science in Mechanical Engineering on 21 March, 2015.

BOARD OF EXAMINERS

1.	--- Dr. Mohammad Ali Professor, Dept. of Mechanical Engineering, Bangladesh University of Engineering and Technology Dhaka, Bangladesh.	Chairman (Supervisor)
2.	--- Dr. Md. Zahurul Haq Professor & Head, Dept. of Mechanical Engineering, Bangladesh University of Engineering and Technology Dhaka, Bangladesh.	Member (Ex-Officio)
3.	--- Dr. Md. Quamrul Islam Professor, Dept. of Mechanical Engineering, Bangladesh University of Engineering and Technology Dhaka, Bangladesh.	Member
4.	--- Dr. Mohammad Mamun Professor, Dept. of Mechanical Engineering, Bangladesh University of Engineering and Technology Dhaka, Bangladesh.	Member
5.	--- Dr. A. K. M. Sadrul Islam Professor, Dept. of Mechanical & Chemical Engineering, Islamic University of Technology Gazipur, Bangladesh.	Member (External)

CANDIDATE'S DECLARATION

It is hereby declared that this thesis or any part of it has not been submitted elsewhere for the award of any degree or diploma.

Signature of the Candidate:

Muhammad Nazmul Haque

ACKNOWLEDGEMENT

This research work was performed under close supervision and thorough guidance of Dr. Mohammad Ali, Professor, Department of Mechanical Engineering, Bangladesh University of Engineering and Technology (BUET). The author would like to expresses his profound gratitude to Professor Dr. Mohammad Ali for his delicate supervision, ceaseless inspiration, deliberate encouragement and untiring support throughout this research work.

The author is also grateful to all the staffs of Turbulence Laboratory of Department of Mechanical Engineering, BUET for providing helping hands while preparing the experimental set up for this research and collecting experimental data.

Finally, the author would like to express his sincere thanks to all other teachers of the Mechanical Engineering Department, BUET, his friends and family members who encouraged him throughout the research work and helped to accomplish the work successfully.

ABSTRACT

Aircraft wings are the lifting surfaces with the chosen aerofoil sections. The lift generated by the wing sustains the weight of the aircraft to make flight in the air. Again, from an aerodynamic perspective, the main source of the airplane drag is associated with the wing. Therefore, the effects of wing shape and size are crucial to aerodynamic characteristics (lift, drag, lift to drag ratio, pitching moment, etc.) on which the efficiency as well as the performance of aircraft depend. The shape/geometry of wing can be varied span wise to search better performance. This thesis represents the experimental investigation to explore better aerodynamic performance by incorporating curvature at the leading edge and trailing edge of wing. The curvature is incorporated in the wing geometry without changing the overall surface area to reduce the chord length towards the tip of the wing.

The experimental investigation is carried out in the wind tunnel to explore aerodynamic characteristics of two different wings of curved-edge planforms; one having curve at leading edge and the other having curve at trailing edge. Similar characteristics of a rectangular wing of equal span and surface area are also investigated in the same way for reference. Wooden wing models for rectangular planform and curved-edge planforms are prepared having the same span and equal surface area. All the models are tested at air speed of 85.35 kph (0.07 Mach) i.e. at Reynolds Number 1.82 x 10^5 in the closed circuit wind tunnel. The static pressure at different Angle of Attack (-4˚, 0˚, 4˚, 8˚, 12˚, 16˚, 20˚ & 24˚) are measured from both upper and lower surfaces of the wing models through different pressure tapings by using a multi-tube water manometer. The aerodynamic characteristics (Coefficient of Lift, Coefficient of Drag and Lift to Drag ratio) for different models are determined from the static pressure distribution.

After analyzing the data, it is found that the curved leading edge wing planform is having higher lift coefficient and lower drag coefficient than the rectangular planform. Again, the curved trailing edge planform is having higher lift coefficient and lower drag coefficient than the curved leading edge wing. Thus, the curved trailing edge planform is having the highest lift to drag ratio among the three types of planforms. Due to reduction in the chord length near the tip of the curved-edge wings, the tip loss is also reduced. As such, aerodynamic performance of the curved edge planforms are found better than that of the rectangular planform.

CONTENTS

LIST OF FIGURES

Page No.

Page No.

LIST OF TABLES

NOMENCLATURE

A	Axial force
b	Wing span
C	Wing chord
C_D	Coefficient of drag
C_L	Coefficient of lift
C_P	Coefficient of pressure
C_{Pl}	Lower surface pressure coefficient
C_{Pu}	Upper surface pressure coefficient
D	Drag force
L	Lift force
L/D	Lift to drag ratio
L.E.	Leading edge
N	Normal force
p	Pressure
P_∞	Free stream pressure
R_N	Reynolds number
S	Wing surface area
T.E.	Trailing edge
U_∞	Free stream velocity of air
v	Velocity of air
α	Angle of attack
τ	Shear stress
ρ or, ρ_a	Density of air
ρ_w	Density of water
μ_a	Absolute viscosity of air
μ_w	Absolute viscosity of water
$\frac{1}{2}\rho\, U_\infty^2$	Free stream dynamic pressure

1. INTRODUCTION

1.1 General

Similar to a bird's wing, an aircraft wing is the lifting surface with the chosen aerofoil section, whose shape/geometry can be varied span wise to search better performance. The lift generated by the wing sustains the weight of the aircraft to make flight in the air. Again, from an aerodynamic perspective, the main source of the airplane drag is associated with the wing. Around two-thirds of the total drag of typical transport aircraft at cruise conditions is produced by the wing [1].

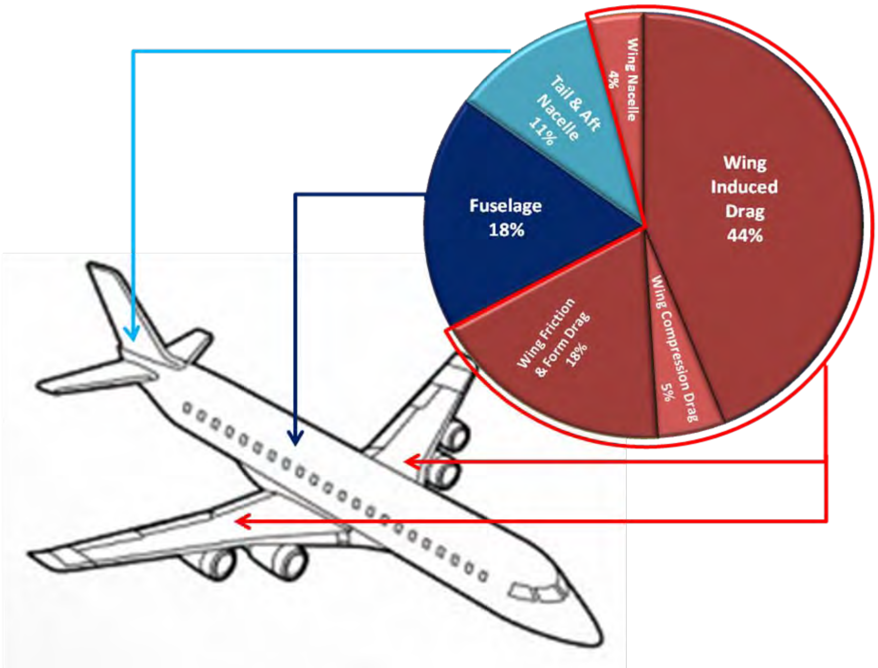

Figure 1.1: Typical Drag Breakdown by Components of Transport Aircraft [1]

Therefore, the effects of wing shape and size are crucial to aerodynamic characteristics on which the efficiency as well as the performance of aircraft depends. As such, researches on different wing shapes/geometries are still on throughout the world to explore the maximum possible lift and minimum possible drag. The present research is also focusing on the improved aerodynamic characteristics and performance through variation in wing planforms.

1.2 Aerodynamic Characteristics of Wing

The wing is a 3D object, but is usually treated as a set of two 2D geometric features; planform (x-y plane) and airfoil (x-z plane) as shown in Figure 1.2:

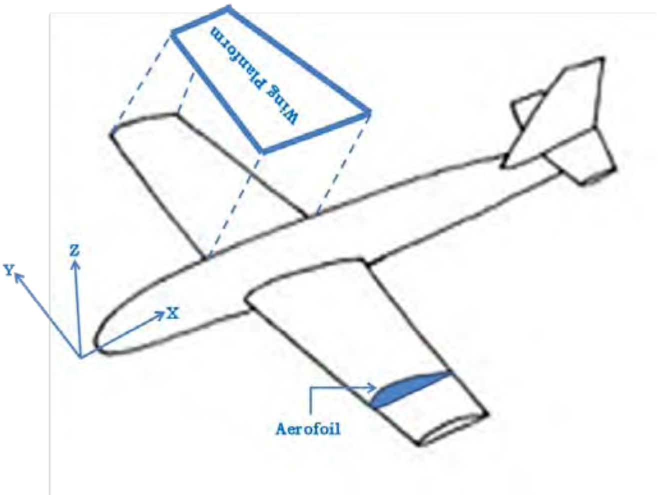

Figure 1.2: Geometric Features of a Typical Aircraft Wing

The flow of air through the surfaces of an aircraft produces the lifting force. The shape of the wings of an aircraft is designed to make the airflow through the surface to produce a lifting force in the most efficient manner. In addition to the lift, a force directly opposing the motion of the wing through the air is always present, which is called drag force. The angle between the relative wind and the chord line is the Angle of Attack of the airfoil.

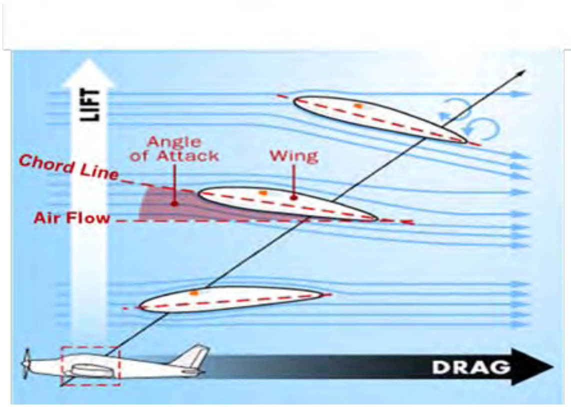

Figure 1.3: Aerodynamic Characteristics of Aircraft Wing

The lift and drag forces developed by the wing vary with the change of angle of attack. The lift force increases almost linearly with angle of attack until a maximum value is reached, whereupon the wing is said to stall. The variation of the drag force with angle of attack is approximately parabolic. It is desirable for the wing to have the maximum lift and smallest possible drag i.e. the maximum possible lift to drag ratio. The variation of all these aerodynamic characteristics (lift force, drag force and lift to drag ratio) with angle of attack for a typical aircraft are shown in Figure 1.4:

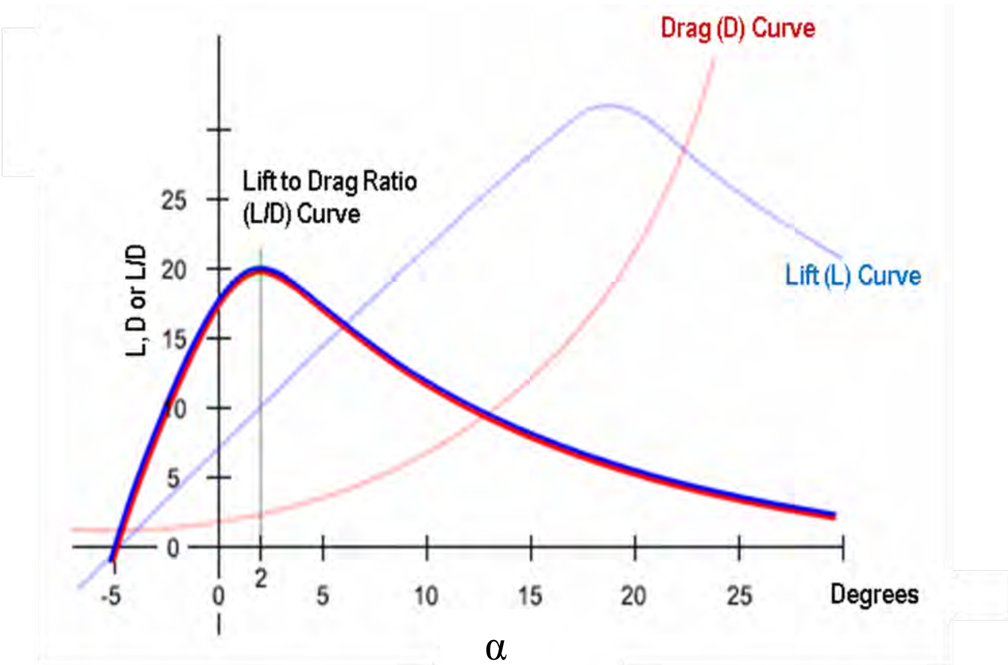

Figure 1.4: Variation of Aerodynamic Characteristics with Angle of Attack

The aerodynamic characteristics of a wing depend on several parameters; the wing's geometry, density of air, airspeed and the Angle of Attack. In this research, NACA 4412 aerofoil has been used for different planforms in the same airspeed, density of air and Angle of Attack with a view to search the effect of variation of wing planform/geometry on the aerodynamic characteristics.

1.3 Motivation of the Present Work

Literature review as discussed in the next chapter reveals that researches on different airfoils and conventional wing geometries like rectangular, sweepback, tapered or, delta shapes have been carried out in many places around the world in an extensive way. But aerodynamic characteristics of curved-edge wing planforms are yet to be explored. As such, effort was taken to investigate aerodynamic characteristics of such wings through experimental method (wind-tunnel test).

1.4 Scope and Objectives of the Research

The proposed experimental investigation is carried out in the wind tunnel to explore aerodynamic characteristics of two different wings of curved-edge planforms; one having curve at leading edge and the other having curve at trailing edge. Similar characteristics of a rectangular wing of equal span and surface area are also investigated in the same way for reference. At the end, the characteristics of the curved-edge wings are compared with that of the rectangular wing. So the specific objectives and scope of the research are as follows:

a. To obtain the pressure distribution over the surfaces of different shapes of wing with NACA 4412 aerofoil (rectangular, curved leading edge and curved trailing edge).

b. To obtain the pressure distribution at different Angles of Attack of the wing models with a suitable fixture required during the experiment in the wind tunnel available at turbulence lab of BUET.

c. To determine the aerodynamic characteristics (Coefficient of Pressure-C_p, Coefficient of Lift-C_L, Coefficient of Drag-C_D and Lift to Drag Ratio-L/D) from static pressure distributions of the wing models.

d. To analyze and compare all the above characteristics with the variation of Angle of Attack.

1.5 Outline of the Research Report

The research report is organized as follows:

a. The first chapter presents the background information along with scope and objectives of the research.

b. The second chapter reviews the available literature related to the present research work.

c. The third chapter presents the overview of the aerodynamics of wing.

d. The fourth chapter describes theory of calculations and mathematical modeling in details.

e. The fifth chapter illustrates the details of experimental set up and procedures.

f. The sixth chapter presents the experimental results and discussion on the important aspects of the results.

g. Finally, the seventh chapter concludes the overall research and recommends few scopes for further research related to the present outcome.

2. LITERATURE REVIEW

The available literature directly or indirectly related with the aerodynamics of wings and aerofoils focus on the following areas:

Hossain et al. [2] conducted an experimental analysis for the aerodynamic characteristics of rectangular wing with and without bird feather like winglets for different Reynolds Number. The experimental result shows 25~30% reduction in drag coefficient and 10~20% increase in lift coefficient by using bird feather like winglet at 8 degree angle of attack.

Dwivedi et al. [3] adopted a simple approach for experiment on aerodynamic static stability analysis of different types of wing shapes. They tested the reduced scale size wings of different shapes like rectangular, rectangular with curved tip, tapered, tapered with curved tip, etc. in low speed subsonic wind tunnel at different air speeds and different angles of attack. The authors found that the tapered wing with curved tip was the most stable at different speeds and ranges of working angles of attack.

Mineck et al. [4] tested three planar, untwisted wings with the same elliptical chord but with different curvatures of the quarter-chord line. They found that the elliptical wing with the unswept quarter-chord line has the lowest lifting efficiency, the elliptical wing with the unswept trailing edge has the highest lifting efficiency and the crescent-shaped wing has efficiency in between.

Recktenwald [5] tested a circular planform non-spinning body with an airfoil section configuration developed and produced by Geobat Flying Saucer Aviation Inc. in the Auburn University wind tunnel facility. For comparison purpose, a Cessna 172 model was also tested. The author found that the lift curve slope of the Geobat was less than that of Cessna 172 but displayed better stall characteristics.

Wakayama [6] studied and presented basic results from wing planform optimization for minimum drag with constraints on structural weight and maximum lift. Analyses in each of these disciplines were developed and integrated to yield successful optimization of wing planform shape. Results demonstrated the importance of weight constraints, compressibility drag, maximum lift, and static aero-elasticity on wing shape, and the necessity of modeling these effects to achieve realistic optimized planforms.

Paulo et al. [7] studied Multi-disciplinary Design and Optimization (MDO) of a transport aircraft wing. They developed a mathematical model of the MDO framework using MATLAB which includes the calculation of aircraft drag polar (based on geometrical characteristics), stability derivatives and performance for some flight phases.

Aerodynamic characteristics analyses for different airfoils have also been conducted at different corners of the world like Mahmud [8] analyzed the effectiveness of an airfoil with bi-camber surface. Kandwal et al. [9] presented a computational method to deduce the lift and drag properties, which can reduce the dependency on wind tunnel testing. The study is done on air flow over a two-dimensional NACA 4412 Airfoil using ANSYS FLUENT (version 12.0.16), to obtain the surface pressure distribution, from which drag and lift were calculated using integral equations of pressure over finite surface areas. In addition, the drag and lift coefficients were also determined. The CFD simulation results show close agreement with those of the experiments, thus suggesting a reliable alternative to experimental method in determining drag and lift. Robert [10] studied the variation of pressure distribution over an airfoil with Reynolds Number. Sharma [11] analyzed the flow behaviour around an airfoil body.

Ismail [12] presented a preliminary analytic method for estimation of load and pressure distributions on low speed wings with flow separation and wake rollup phenomena. A higher order vortex panel method was coupled with the numerical lifting line theory by means of iterative procedure including models of separation and wake rollup. The presented method was investigated through a number of test cases with different types of wing sections (NACA 0012 and GA (W)-1) for different aspect ratios and angles of attack, the results include the lift and drag curves, lift and pressure distributions along the wing span taking into the consideration the effect of the angles of attack and the aspect ratios on the wake rollup. The pressure distribution on the wings showed that there is a region of constant pressure on the upper surface of the wings near the trailing edge in the middle of the wing, also there is a region of flow separation on the upper surface of the wings. A good agreement was found between the presented work results and other from previous researches.

Wells [13] made an effort to verify the high performance characteristics of the co-flow jet (CFJ) airfoil experimentally. The CFJ utilizes tangentially injected air at the leading edge and tangentially removed air at the trailing edge to increase lift and stall margin and also to decrease drag. The mass flow rates of the injection and suction are equal, so there is a zero net mass flow rate. Two airfoils were tested at the University of Florida. One airfoil had an injection slot size of 0.65% chord length and the other had an injection slot size twice as large or 1.31% chord length. Both airfoils had a suction slot size of 1.96% chord length. The smaller injection slot size performed superior for increased lift and stall margin, whereas the larger injection slot size performed superior for decreased drag. The smaller injection slot airfoil had an increase in maximum lift of 113% to 220% and an increase in stall margin of 100% to 132% when compared to the baseline airfoil.

Demasi [14] presented an original method of predicting the minimum induced drag conditions in conventional or innovative lifting systems. The procedure shown is based on the lifting line theories and the small perturbation acceleration potential. Under the hypothesis of linearity and rigid wake aligned with the free stream, the optimal condition was formulated using the Euler-Lagrange integral equation under the conditions of fixed total lifting force and wing span. The minimum induced drag problem was then formulated and solved numerically and analytically when possible. Classical configurations and non-planar lifting systems were extensively analyzed. In particular, the configurations examined were: Classical cantilever wing and biplane, Circular annular wing, Elliptical annular wing, Elliptical lifting arcs. For each system, the optimal circulation distribution and the minimum induced drag were calculated. Also, comparison with the theoretical and experimental reference values was made.

McArthur [15] studied three airfoil shapes at Reynolds numbers of 1 and 2×10^4; a flat plate airfoil, a circular arc cambered airfoil, and the Eppler 387 airfoil. Lift and drag force measurements were made on both 2D and 3D conditions, with the 3D wings having an aspect ratio of 6, and the 2D condition being approximated by placing end plates at the wing tips. Comparisons to the limited number of previous measurements showed adequate agreement. Previous studies had been inconclusive on whether lifting line theory could be applied to this range of R_N, but this study showed that lifting line theory could be applied when there were no sudden changes in the slope of the force curves.

Alam [16] made an effort to determine the interference effect of different biplane configurations. NACA 0024 symmetric aerofoil with chord length of 100mm was used for four biplane configurations. The interference effects were analyzed by varying the distance between the aerofoils and the angle of attack numerically with the help of CFD software. The interference effect is more for biplane configuration at 0.40 of chord length and reduces when the distance between the aerofoils increases.

Hassan et al. [17] investigated the aerodynamic characteristics of forward swept wing theoretically and experimentally. Theoretically, a computer program was constructed to predict the pressure distribution about surface of the wing using three dimensional Low Order Subsonic Panel method. The aerodynamic coefficients of the wing were calculated from the pressure distribution which gained from tangential velocities experimentally. Test were carried out by designing and manufacturing a wing model with special arrangement for pressure tapping suitable for wind tunnel testing. The entire wing was rotated about an axis in the plane of symmetry and normal to the chord to produce different sweep and incidence angles for wing by using rotating mechanism. Wind tunnel test was carried out at (U_∞=33.23m/s) for different swept angles and angles of attack. Comparisons were made between the predicted and experimental results. It was clear from the investigation that the lift and drag characteristics for the forward swept wing were less in values compared with the swept back wing. Therefore, a forward swept wing can fly at higher speed corresponding to a pressure distribution associated for lower speed.

Ahmed [18] studied the flow characteristics over a NACA 4415 airfoil experimentally at a Reynolds number of 2.4 x 10^5 by varying the angle of attack from 0 to 10° and ground clearance of the trailing edge from five percent of chord to eighty percent. The pressure distribution on the airfoil surface was obtained, velocity survey over the surface was performed, wake region was explored and lift and drag forces were measured. A strong suction effect was observed on the lower surface for angles of attack of 0 and 2.5° at small ground clearances. For the angle of attack of 0°, a separation bubble formed on the lower surface for the smallest ground clearance while for 2.5°, laminar separation occurred from the lower surface well ahead of the trailing edge. Increased suction was observed on the upper surface for small ground clearances. For the angle of attack of 10°, the flow on the upper surface could not withstand the adverse pressure gradient at small ground clearances and separated from the surface resulting in a loss of lift and an increase in drag.

Walter [19] investigated the effect of ground proximity on the lift, drag and moment coefficients of inverted, two-dimensional aerofoils. The purpose of the study was to examine the effect of ground proximity on aerofoils post stall, in an effort to evaluate the use of active aerodynamics to increase the performance of a race car. The aerofoils were tested at angles of attack ranging from 0°~135°. The tests were performed at a Reynolds number of 2.16 x 10^5 based on chord length. Forces were calculated via the use of pressure taps along the centre line of the aerofoils. The RMIT Industrial Wind Tunnel (IWT) was used for the testing. The IWT was chosen as it would allow enough height to reduce blockage effect caused by the aerofoils when at high angles of incidence. The walls of the tunnel were pressure tapped to allow monitoring of the pressure gradient along the tunnel. The results show a delay in the stall of the aerofoils tested with reduced ground clearance. Two of the aerofoils tested showed a decrease in C_L with decreasing ground clearance; the third showed an increase. The C_D of the aerofoils post-stall decreased with reduced ground clearance. Decreasing ground clearance was found to reduce pitch moment variation of the aerofoils with varied angle of attack.

Al-Kayiem et al. [20] investigated the wing-ground collision experimentally and numerically. The investigation involved a series of wind tunnel measurements of a 2-D wing model having NACA 4412 airfoil section. An experimental set up has been designed and constructed to simulate the collision phenomena in a low speed wind tunnel. The investigations were carried out at different Reynolds numbers ranging from 10^5 to 4×10^5, various model heights to chord ratios ranging from 0.1 to 1, and different angles of attack ranging from -4° to 20°. Numerical simulation of the wing-ground collision was carried out using FLUENT software. The results showed that the aerodynamic characteristics were considerably influenced when the wing is close to the ground, mainly at angles of attack 4° to 8°. The take-off and landing speeds were found to be very influencing parameters on the aerodynamic characteristics, mainly the lift of the wing in collision status.

Janiszewska [21] conducted a comprehensive experimental investigation on a LS (1)-0421MOD airfoil model. Surface pressure distributions were obtained for 2D baseline and 3D configurations under clean and surface grit conditions. Several vortex generator configurations were evaluated. The data were taken for steady state and unsteady conditions. The steady state data included angles of attack from 0° to 30° and Reynolds numbers of 1.0 million. The unsteady conditions were simulated using a face cam that provided a sinusoidal angle of attack variation with 10° amplitude for three frequencies of 0.6 and 1.8 Hz at mean angles of attack of 8°, 14° and 20°. Surface pressure data were obtained from six spanwise stations, which were integrated to local coefficients. The maximum 2D lift coefficient obtained for the 1.0 million Reynolds number was 1.58 at 14.4° angle of attack. For the 3D case the maximum lift coefficient at the wall was 1.58 at 19°.5 and at the tip was 1.20 at 18.3°. The results showed that the application of the grit roughness reduces the maximum lift coefficients in all configurations by as much as 50%. The Flat and Curled vortex generators increased the maximum lift coefficient for both the 3D tip and wall stations, up to 1.6 and 1.92, respectively. The application of the vortex generators shifted the stall angle of attack by approximately 30%. A gritted model with the vortex generators showed an increase in both the maximum lift and stall angle of attack by approximately 25% in comparison to grit only. The unsteady maximum lift coefficients were always higher than those for the steady state up to 60% and showed, generally, large hysteresis loops. The hysteresis loops were smaller for the 3D wing configuration due to the tip vortex influence, therefore smallest hysteresis loops occurred at the tip. The Flat and Curled vortex generators removed the hysteresis loops for all frequencies at 14° me an angle and significantly reduced the minimum value of the pitching moment and the pressure drag at stall.

Arora [22] studied aerodynamic characteristics for the aircraft model with NACA wing No. 65- 3-218 using subsonic wind tunnel of 1000 mm x 1000 mm rectangular test section. Tests were conducted on the aircraft model with and without winglet of two configurations at Reynolds numbers 1.7 x 10^5, 2.1 x 10^5, and 2.5 x 10^5. Lift curve slope increased more with the addition of the elliptical winglet and at the same time the drag decreased more for the aircraft model with elliptical shaped winglet giving an edge over the aircraft model without winglet as far as lift to drag ratio for the elliptical winglet is considered. Elliptical winglet of configuration 2 (winglet inclination 60°) showed, overall, the best performance, giving about 6% increase in lift curve slope as compared to without winglet configuration and it also provided the best lift to drag ratio.

Mashud [23] introduced a flow separation control mechanism to improve the aerodynamic characteristics of an airfoil. Control of flow separation over an airfoil which experiences a laminar separation bubble for a low Reynolds number was experimentally simulated under the effects of suction and injection. To perform the experiment a NACA 4215 airfoil profile was chosen to make the wing model. The wing model with control mechanism was tested in a subsonic wind tunnel for different angles of attack and different suction-injection frequency. The experimental results showed that the flow separation could be controlled by the proposed mechanism. The wing performance was significantly improved due to control of flow separation by suction and injection. It was also found that the lift increased about 14% and drag reduced about 23% at 8°angle of attack.

3. OVERVIEW OF WING AERODYNAMICS

3.1 Wing and Aerofoil

The wing may be considered as the most important component of an aircraft, since a fixed-wing aircraft is not able to fly without it. The primary function of the wing of an aircraft is to generate lift force to make the flight possible in the air. This will be generated by a special wing cross section called airfoil. Wing is a three dimensional component, while the airfoil is two dimensional section as shown in Figure 3.1. The wing may have a constant or a non-constant cross-section across the wing [24].

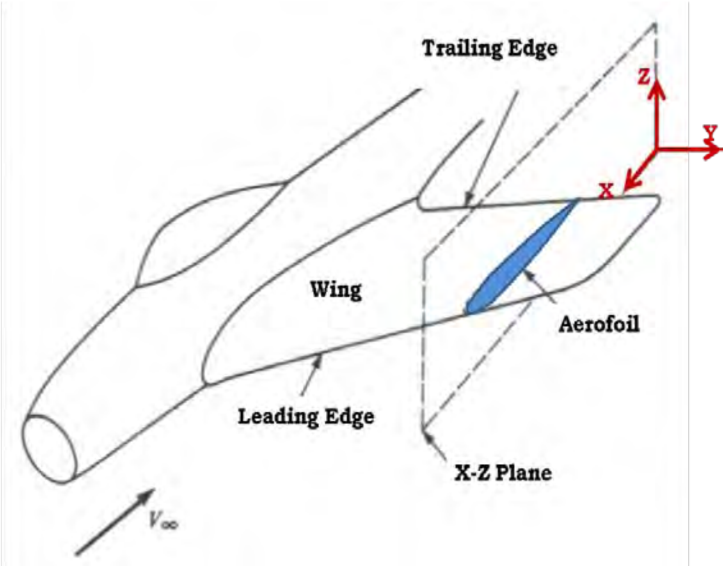

Figure 3.1: Wing and Aerofoil

3.2 General Features of an Aerofoil

Any section of the wing cut by a plane parallel to the aircraft xz plane is called an aerofoil. It is usually looks like a positive cambered section that the thicker part is in front of the aerofoil. A typical aerofoil section is shown in Figure 3.2, where several geometric parameters are illustrated [25, 26].

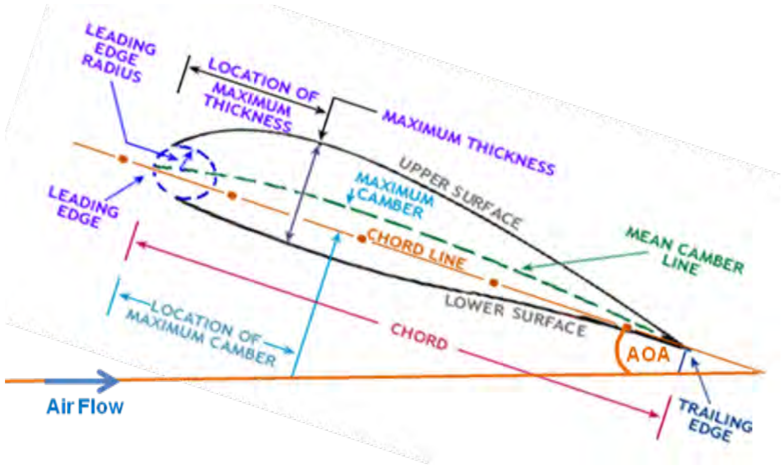

Figure 3.2: Geometric Features of an Aerofoil

The major feature of an aerofoil is the mean camber line, which is the locus of points halfway between the upper and lower surfaces. The most forward and rearward points of the mean camber line are the leading and trailing edges respectively. The straight line connecting the leading and trailing edges is the chord line of the aerofoil and the precise distance from the leading to the trailing edge measured along the chord line is called the chord of the aerofoil. The camber is the maximum distance between the mean camber line and chord line, measured perpendicular to the chord line. If the mean camber line in a straight line, the airfoil is referred to as symmetric airfoil, otherwise it is called cambered aerofoil. The camber of aerofoil is usually positive. The angle between the chord line and the direction of air flow is called the angle of attack.

3.3 Aerodynamic Forces Developed by Aerofoil

An airfoil-shaped body moved through the air will vary the static pressure on the top surface and on the bottom surface of the airfoil. In a positive cambered airfoil, the upper surface static pressure in less than ambient pressure, while the lower surface static pressure is higher than ambient pressure [24-26]. This is due to higher airspeed at upper surface and lower speed at lower surface of the airfoil as shown in Figure 3.3. As the airfoil angle of attack increases, the pressure difference between upper and lower surfaces will be higher as shown in Figure 3.4.

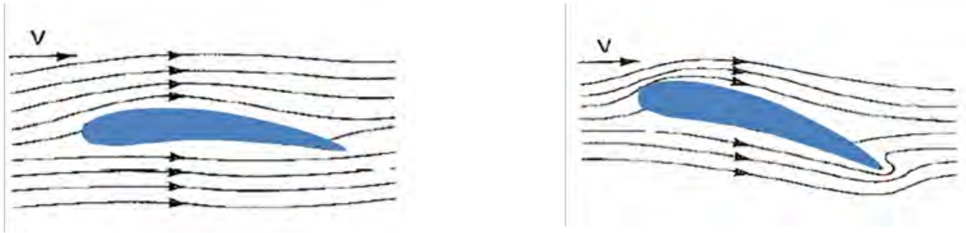

a. At Small Angle of Attack　　b. At Large Angle of Attack

Figure 3.3: Flow around an Aerofoil

a. At Small Angle of Attack　　b. At Large Angle of Attack

Figure 3.4: Pressure Distribution around an Aerofoil

The force divided by the area is called pressure, so the aerodynamic force generated by an airfoil in a flow field may be calculated by multiplication of total pressure by area. The total pressure is simply determined by integration of pressure over the entire surface. The magnitude, location, and direction of this aerodynamic force are functions of airfoil geometry, angle of attack, flow properties, and airspeed relative to the airfoil. The location of this resultant force out of the integration is called center of pressure. The location of this center depends on aircraft speed and the airfoil's angle of attack.

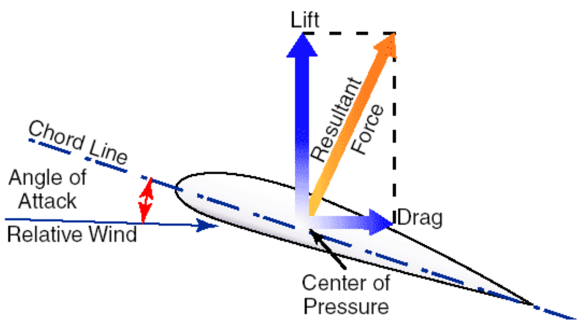

Figure 3.5: Aerodynamic Forces Acting on Aerofoil

Thus, the pressure and shear stress distributions over the airfoil generate an aerodynamic force. However, this resultant force is replaced with two aerodynamic forces as shown by the vector in Figure 3.5. On the other word, the aerodynamic force can be resolved into two forces, perpendicular (lift) and parallel (drag) to the relative wind. The lift is always defined as the component of the aerodynamic force perpendicular to the relative wind. The drag is always defined as the component of the aerodynamic force parallel to the relative wind.

3.4 Characteristics of an Airfoil

There are several graphs that illustrate the characteristics of each airfoil when compared to other airfoils in the wing airfoil selection process. These are mainly the variations of non-dimensionalized lift and drag relative to angle of attack [27, 28]. Two aerodynamic forces are usually non-dimensionalized by dividing them to appropriate parameters as follows:

$$C_L = \frac{L}{\frac{1}{2}\rho U_\infty^2 A} \tag{3.1}$$

$$C_D = \frac{D}{\frac{1}{2}\rho U_\infty^2 A} \tag{3.2}$$

Where, L and D are the lift force and drag force respectively.

A is the Planform area=Chord x Span.

U_∞ is the free stream air velocity.

$\frac{1}{2}\rho U_\infty^2$ is the dynamic pressure.

Another important parameter, the lift-to-drag ratio (L/D) is the amount of lift generated by an airfoil, divided by the drag it creates by moving through the air. An airplane has a high L/D if it produces a large amount of lift or a small amount of drag. A higher or more favourable L/D is typically one of the major goals in aircraft design.

$$Ratio = \frac{Lift}{Drag} = \frac{L}{D} \tag{3.3}$$

Thus, the performance and characteristics of an airfoil may be evaluated by looking at the following graphs:

a. The variations of lift coefficient with angle of attack

b. The variations of drag coefficient with angle of attack

c. The variations of drag coefficient with lift coefficient

d. The variations of lift-to-drag ratio with angle of attack

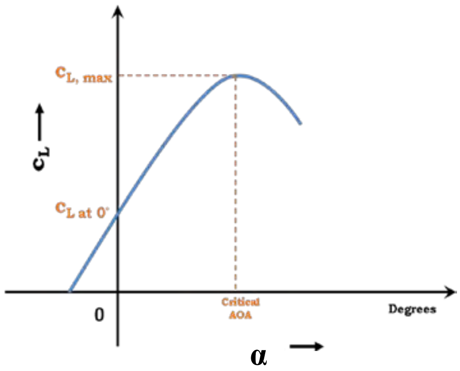

a. C_L vs α graph

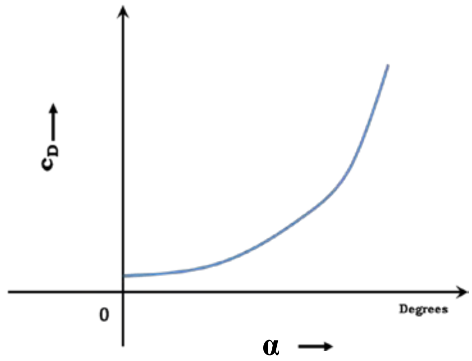

b. C_D vs α graph

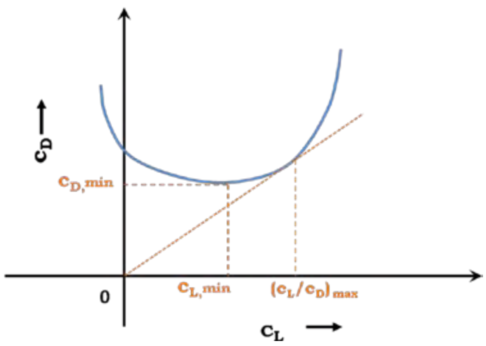

c. C_D vs C_L graph

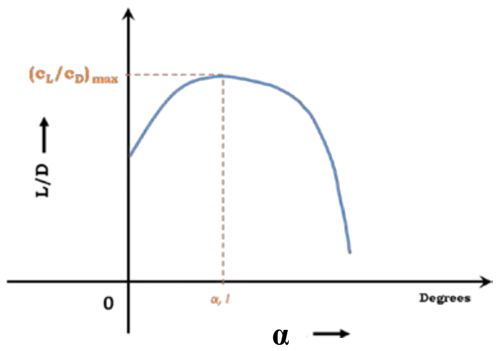

d. L/D vs α graph

Figure 3.6: Characteristics of Aerofoil

3.5 Aerofoil Data Sources

Selection of a proper airfoil is possible from the previously designed and published airfoil sections. Two reliable airfoil resources are NACA and Eppler. The details of Eppler airfoils have been published in [29]. NACA airfoils have been published in a book published by Abbott and Von Donehoff [30]. Eppler airfoil names begin with the letter "E" followed by three numbers. In general, the Eppler airfoils are for very low Reynolds number, Wortman airfoils for low (sailplane-ish) Reynolds number, and the NASA Low-Speed airfoils (e.g. LS(1)-0413) and Mid Speed Airfoils e.g. MS(1)-0313) are for "moderate" Reynolds numbers [31].

3.6 Familiarization with NACA Airfoils

One of the most reliable resources and widely used data base is the airfoils developed by National Advisory Committee for Aeronautics, NACA (predecessor of NASA) in 1930s and 1940s. Different groups of airfoils like Four-digit, Five-digit, 6-series, 7-series, 8-series and 16-series NACA airfoils are available. The Cambered airfoil sections of all NACA families are obtained by combining a mean line and a thickness distribution [32].

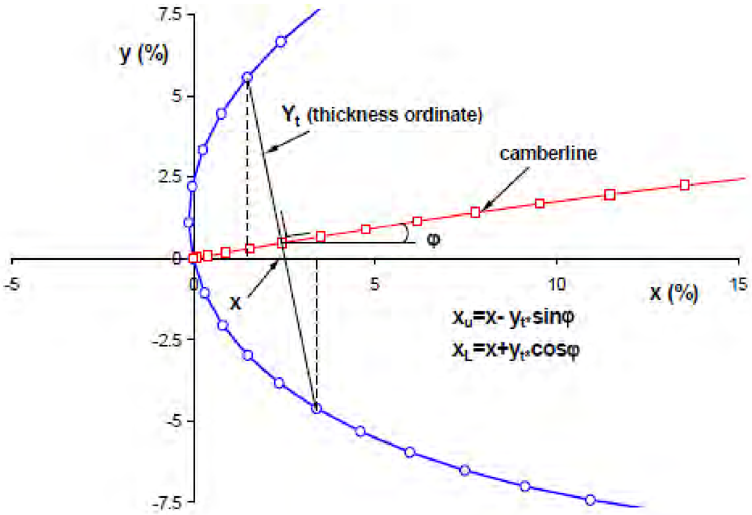

Figure 3.7: NACA Aerofoil Co-ordinates

The abscissas, ordinates and slopes of the mean line are designated as x_c , y_c and $\tan\theta$ respectively. If x_u and y_u represent the abscissa and ordinate of a typical point of the upper surface of the airfoil and y_t is the ordinate of the symmetrical thickness distribution at the chordwise position x, the upper and lower surface coordinates are given by the following relations (u denotes upper surface and l denotes lower surface):

$$x_u = x - y_t(x)Sin\theta \tag{3.4}$$

$$y_u = y_c(x) + y_t(x)Cos\theta \tag{3.5}$$

$$x_l = x + y_t(x)Sin\theta \tag{3.6}$$

$$y_l = y_c(x) - y_t(x)Cos\theta \tag{3.7}$$

Where, $y_t(x)$ is the thickness function

$y_c(x)$ is the camber line function

$\tan\theta = \frac{dy_c}{dx}$ is the camber line slope

The first family of airfoils designed in the above mentioned way is known as the NACA Four-Digit aerofoils. The explanation of the 4-digit NACA aerofoil is as follows [28, 32]:

a. The first digit specifies the maximum camber in percentage of the chord.

b. The second digit indicates the position of the maximum camber in tenths of chord.

c. The last two digits provide the maximum thickness of the airfoil in percentage of chord.

For example, the NACA 4412 airfoil chosen for this research has a maximum thickness of 12% with a camber of 4% located 40% back from the airfoil leading edge.

3.7 Geometric Parameters of Wing

Aircraft wing can be defined by several geometric parameters such as span (b), wing surface area or planform(S), root chord (C_{root}), tip chord (C_{tip}), etc. as shown in Figure 3.8. Other important parameters are discussed below:

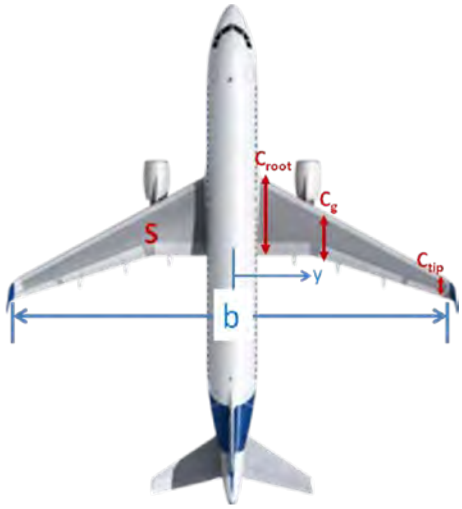

Figure 3.8: Wing Geometric Parameters

3.7.1 Mean geometric chord (C_g)

The mean geometric chord is the chord of a rectangular wing having the same span and the same area as the original wing. It can be found for any general wing in the following way:

$$C_g = \frac{\int_0^{b/2} c(y)dy}{\int_0^{b/2} dy} = \frac{2}{b}\int_0^{b/2} c(y)dy = \frac{S}{b} \tag{3.8}$$

3.7.2 Mean aerodynamic chord (C_{MAC})

The mean aerodynamic chord is (loosely) the chord of a rectangular wing with the span, (not area) that has the same aerodynamic properties with regarding the pitching moment characteristics as the original wing. It can be found for any general wing in the following way:

$$C_{MAC} = \frac{\int_0^{b/2} [c(y)]^2 dy}{\int_0^{b/2} c(y) dy} = \frac{2}{S} \int_0^{b/2} [c(y)]^2 dy \tag{3.9}$$

3.7.3 Aspect ratio (AR)

The aspect ratio is the wing span divided by the mean geometric chord. It is a measure of how long and narrow a wing is. A square wing would have an aspect ratio of 1. Aspect ratio can be calculated in following ways:

$$AR = \frac{b}{C_g} = \frac{b^2}{S} \tag{3.10}$$

2.7.4 Tapper ratio (λ)

It is the ratio of the tip chord to the root chord and is expressed as follows:

$$\lambda = \frac{C_{tip}}{C_{root}} \tag{3.11}$$

3.8 Familiarization with Different Wing Planforms

There are various types of wing planforms which are either successfully used in different aircrafts or still in the process of researches for viable uses. The planforms can be determined according to various factors as discussed below:

3.8.1 According to aspect ratio (AR)

The aspect ratio is the span divided by the mean or average chord. It is a measure of how long and slender the wing appears when seen from above or below.

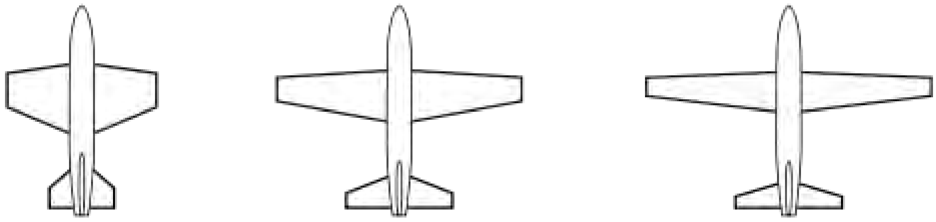

Low AR Moderate AR High AR

Figure 3.9: Wing Planforms according to AR

3.8.2 According to wing sweep

Wings may be swept back or forward swept. A small degree of sweep is sometimes used to adjust the centre of lift when the wing cannot be attached in the ideal position for some reason, such as a pilot's visibility from the cockpit. Some wings may vary the wing sweep during flight:

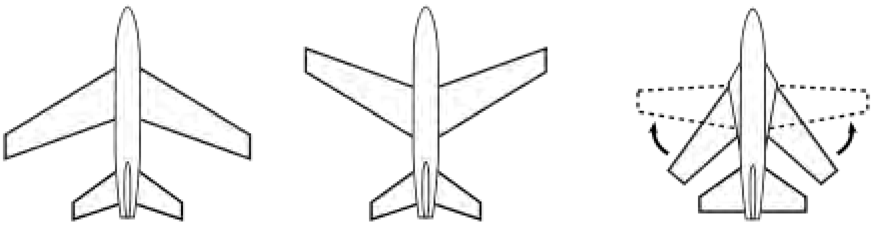

Swept Back Forward Swept Variable Sweep (Swing-Wing)

Figure 3.10: Wing Planforms according to Wing Sweep

3.8.3 According to chord variation along span

The wing chord may be varied along the span of the wing, for both structural and aerodynamic reasons. By varying the chord length along the span, the types of planforms are as follows:

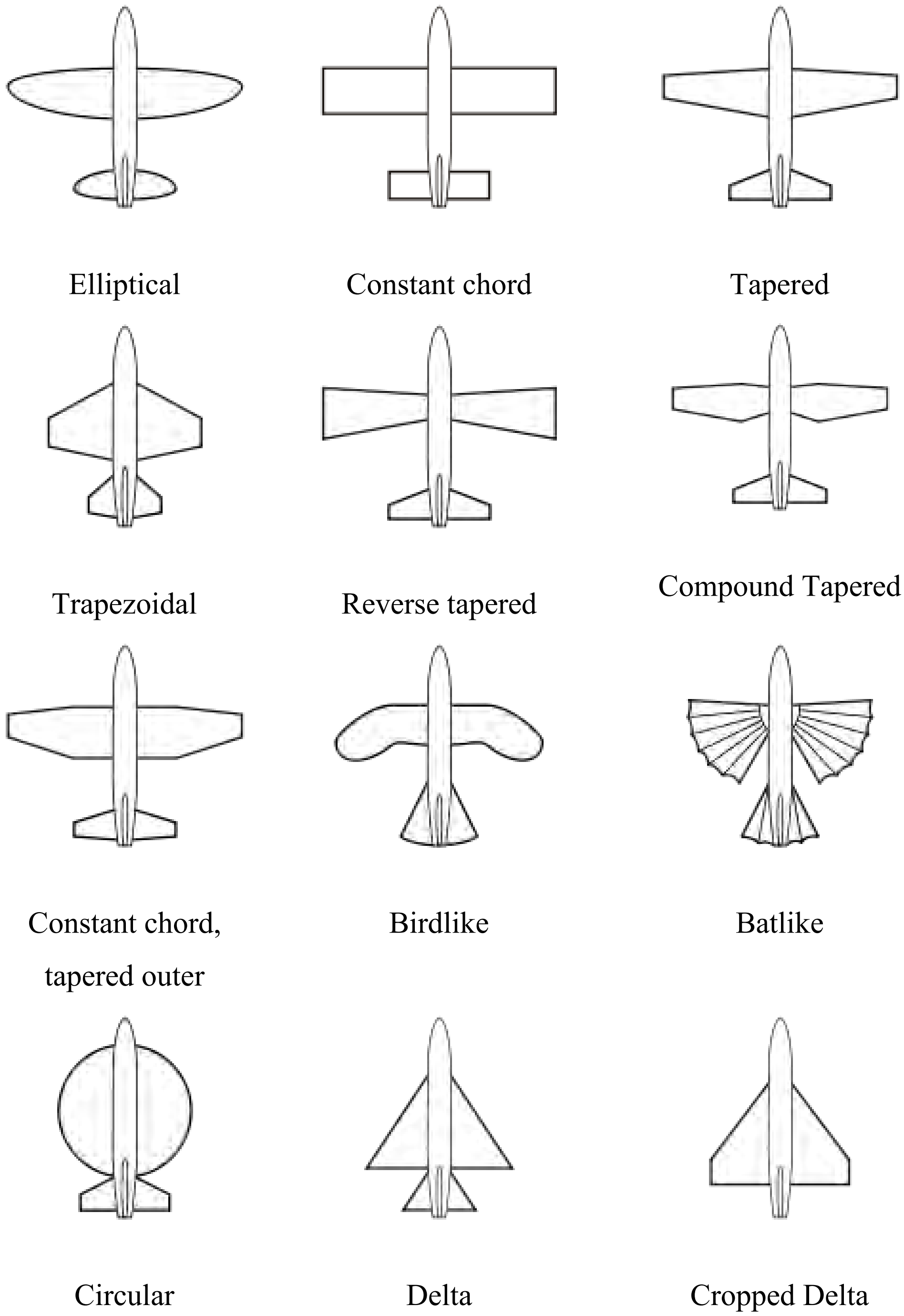

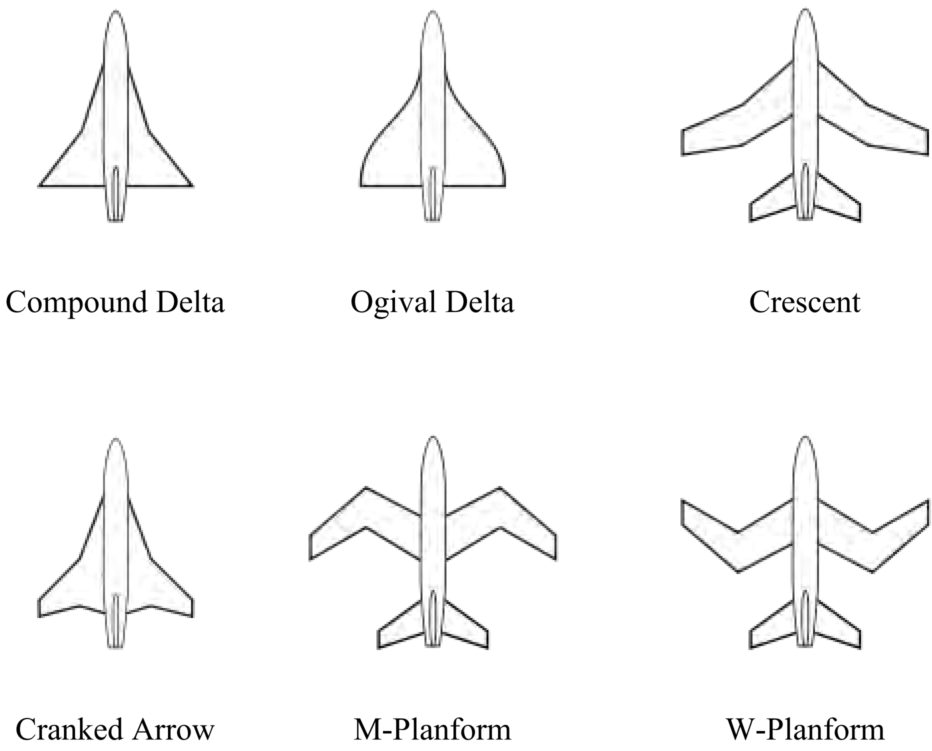

Figure 3.10: Wing Planforms according to Chord Variation

3.8.4 Variable planforms

There are also various types of wings having variable planforms such as telescopic wing, extending wing, bi directional wing, folding wing, etc. In telescoping wing, the outer section of wing telescopes over or within the inner section of wing, varying span, aspect ratio and wing area. In extending wing or expanding wing, part of the wing retracts into the main aircraft structure to reduce drag and low-altitude buffet for high-speed flight and is extended only for takeoff, low-speed cruise and landing. Bi-directional wing is a proposed design in which a low-speed wing and a high-speed wing are laid across each other in the form of a cross. The aircraft would take off and land with the low-speed wing facing the airflow, then rotate a quarter-turn so that the high-speed wing faces the airflow for supersonic flight.

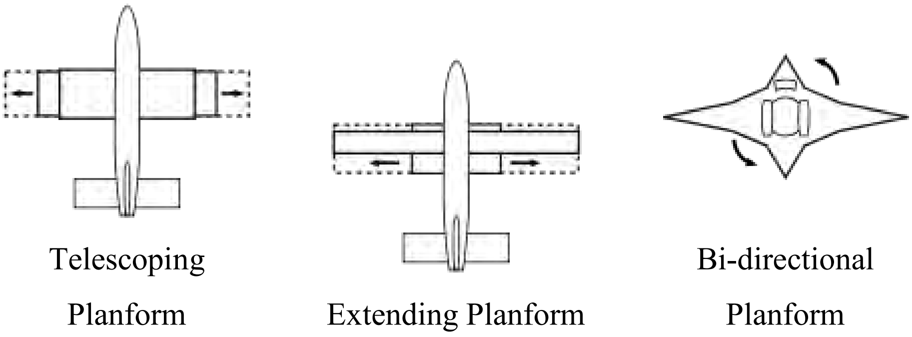

Figure 3.11: Variable Wing Planforms

3.8.5 Wing-body combinations

Some designs have no clear join between wing and fuselage (body of the aircraft) such as flying wing, blended wing body (BWB) and lifting body. In flying wing, the aircraft has no distinct fuselage or horizontal tail (although fins and pods, blisters, etc. may be present) whereas in BWB, a smooth transition occurs between wing and fuselage, with no hard dividing line. BWB design reduces wetted area and can also reduce interference between airflow over the wing root and any adjacent body and thus reduces drag. In case of lifting body, the aircraft lacks identifiable wings but relies on the fuselage (usually at high speeds or high angles of attack) to provide aerodynamic lift.

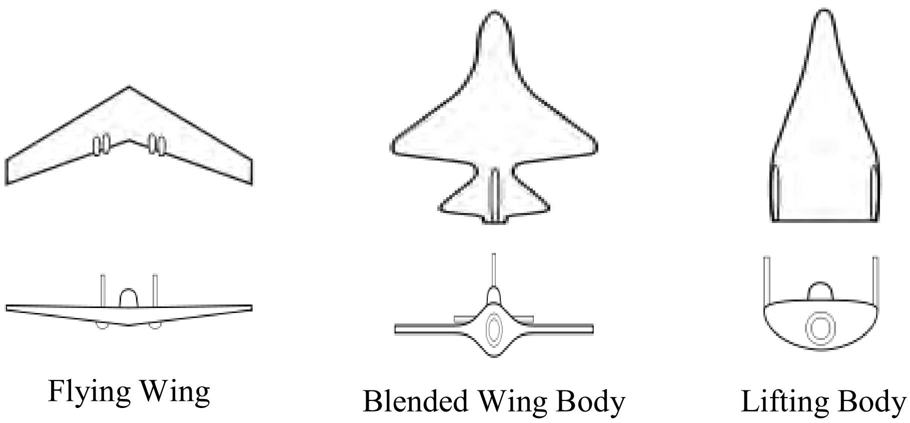

Figure 3.12: Wing Planforms due to Wing-Body Combinations

4. MATHEMATICAL MODELING

4.1 Determination of Pressure Coefficient

Pressure, by itself, is a dimensional quantity. But in the aerodynamic literature, it is very common to find pressures given in terms of C_P rather than the pressure itself. Figure 4.1 shows the pressure distribution at any point over the surface in terms of the pressure coefficient, C_P, which is defined as follows:

$$c_p = \frac{p_{local} - p_\infty}{\frac{1}{2}\rho U_\infty^2} \tag{4.1}$$

Where, $\frac{1}{2}\rho U_\infty^2$ is the free stream dynamic pressure head

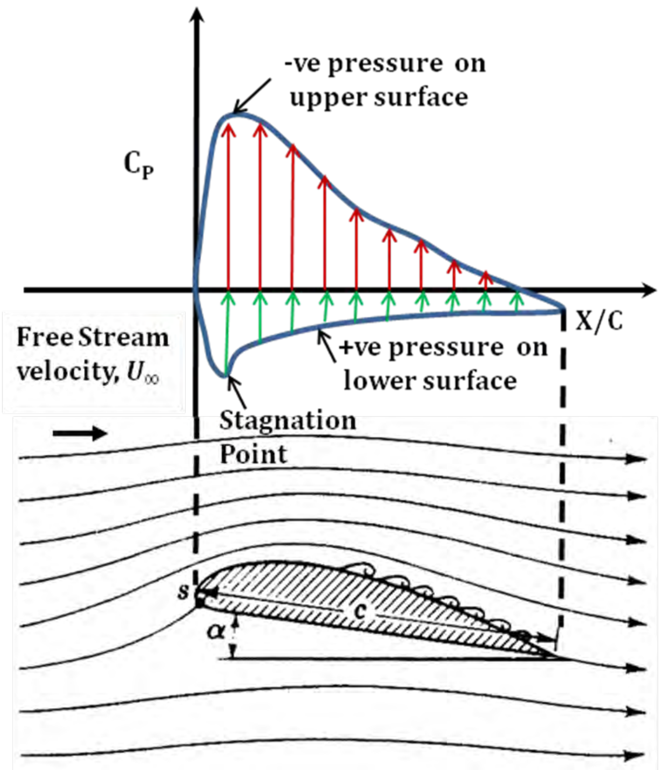

Figure 4.1: Pressure Distribution over an Aerofoil's Surface in terms of C_P

Thus, surface pressure coefficient, C_p can be calculated from the static pressure by the following formula [33].

$$c_{p,i} = \frac{p_i - p_\infty}{\frac{1}{2}\rho U_\infty^2} \tag{4.2}$$

Where, P_i is the surface static pressure at any designated point *i*.

Values of C_p at any point over the aerofoil surface can be approximated from the corresponding boundary values by using the first order Lagrange interpolation and extrapolation:

$$c_p(x) = \frac{(x - x_1)}{(x_0 - x_1)} c_{p,o} + \frac{(x - x_0)}{(x_1 - x_0)} c_{p,1} \tag{4.3}$$

4.2 Estimation of Aerodynamic Force Coefficients from C_P

The aerodynamic forces and moments on the body are due to only two basic sources such as *the pressure distribution* over the body surface and *the Shear stress distribution* over the body surface [12]. No matter how complex the body shape may be, the aerodynamic forces and moments on the body are due entirely to the above two basic sources. The *only* mechanisms nature has for communicating a force to a body moving through a fluid are pressure and shear stress distributions on the body surface. Both pressure *p* and shear stress τ have dimensions of force per unit area (pounds per square foot or newtons per square meter). As sketched in Figure 4.2, *p* acts *normal* to the surface, and τ acts *tangential* to the surface. Shear stress is due to the "tugging action" on the surface, which is caused by friction between the body and the air.

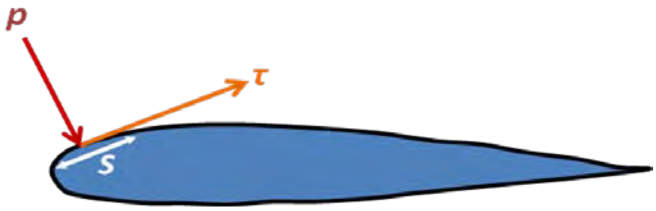

Figure 4.2: Illustration of Pressure and shear Stress on Aerofoil Surface

The net effect of the p and τ distributions integrated over the complete body surface is a resultant aerodynamic force R on the body. In turn, the resultant R can be split into components, two sets of which are shown in Figure 4.3. In Figure 4.3, U_∞ is the *relative wind,* defined as the flow velocity far ahead of the body. The flow far away from the body is called the f*ree stream,* and hence U_∞ is also called the free stream velocity. In Figure 4.3, by definition,

L = lift = component of R perpendicular to U_∞

D = drag = component of R parallel to U_∞

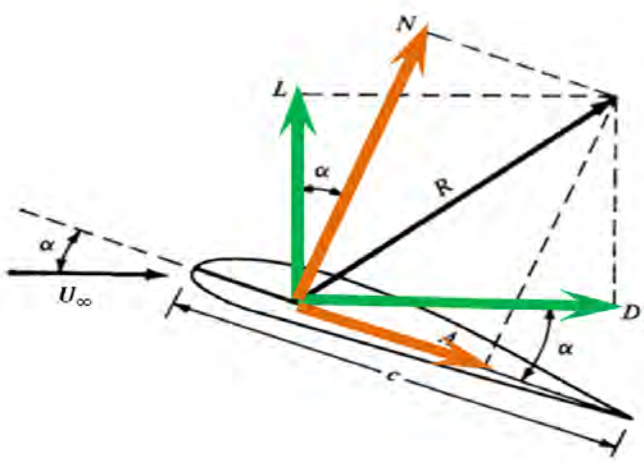

Figure 4.3: Resultant Aerodynamic Force and its Components

The chord c is the linear distance from the leading edge to the trailing edge of the body. Sometimes, R is split into components perpendicular and parallel to the chord, as also shown in Figure 4.3. By definition,

N = normal force = component of R perpendicular to c

A = axial force = component of R parallel to c

The angle of attack α is defined as the angle between c and U. Hence, α is also the angle between L and N and between D and A. The geometrical relation between these two sets of components is found from Figure 4.3 as:

$$L = NCos\alpha - ASin\alpha \tag{4.4}$$

$$D = NSin\alpha + ACos\alpha \tag{4.5}$$

The integration of the pressure and shear stress distributions can be done to obtain the aerodynamic forces and moments [24, 34]. Let us consider the two dimensional body sketched in Figure 4.4. The chord line is drawn horizontally, and hence the relative wind is inclined relative to the horizontal by the angle of attack α. An xy coordinate system is oriented parallel and perpendicular, respectively, to the chord. The distance from the leading edge measured along the body surface to an arbitrary point A on the upper surface is s_u; similarly, the distance to an arbitrary point B on the lower surface is s_l. The pressure and shear stress on the upper surface are denoted by p_u and τ_u, respectively; both p_u and τ_u, are functions of s_u. Similarly, p_l and τ_l are the corresponding quantities on the lower surface and are functions of s_l.

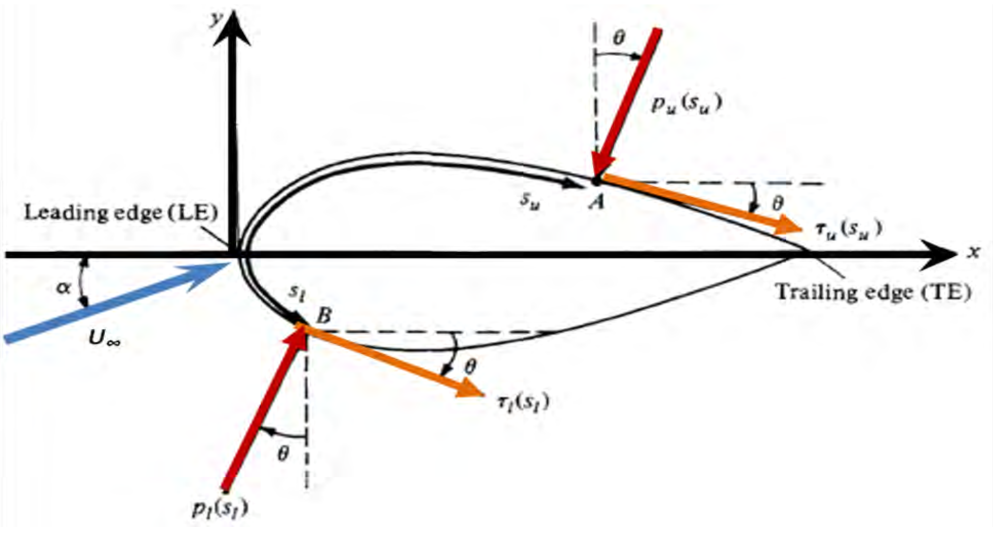

Figure 4.4: Nomenclature for Integration of *p* and *τ* Distribution

At a given point, the pressure is normal to the surface and is oriented at an angle θ relative to the perpendicular; shear stress is tangential to the surface and is oriented at the same angle θ relative to the horizontal. In Figure 4.4, the sign convention for θ is positive when measured *clockwise* from the vertical line to the direction of p and from the horizontal line to the direction of τ. In Figure 4.4, all thetas are shown in their positive direction.

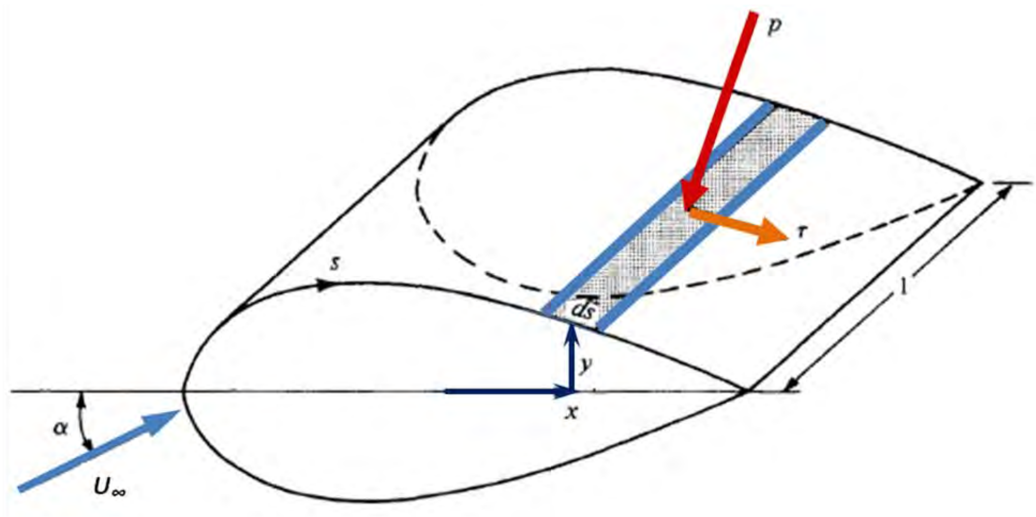

Figure 4.5: Aerodynamic Force on an Element of the Body Surface

Now let us consider the two-dimensional shape in Figure 4.4 as a cross section of an infinitely long cylinder of uniform section. A unit span of such a cylinder is shown in Figure 4.5. Let us consider an elemental surface area *dS* of this cylinder, where *dS* = *(ds)(l)* as shown by the shaded area. We are interested in the contribution to the total normal force N' and the total axial force A' due to the pressure and shear stress on the elemental area *dS*. The primes on N' and A' denote force per unit span. Examining both Figures 4.4 and 4.5, it is seen that the elemental normal and axial forces acting on the elemental surface *d*S on the *upper* body surface are

$$dN'_u = -p_u ds_u Cos\theta - \tau_u ds_u Sin\theta \tag{4.6}$$

$$dA'_u = -p_u ds_u Sin\theta + \tau_u ds_u Cos\theta \tag{4.7}$$

On the *lower* body surface, we have

$$dN'_l = p_l ds_l Cos\theta - \tau_l ds_l Sin\theta \quad (4.8)$$

$$dA'_l = p_l ds_l Sin\theta + \tau_l ds_l Cos\theta \quad (4.9)$$

In these equations, the positive clockwise convention for θ must be followed. For example, consider again Figure 4.4. Near the leading edge of the body, where the slope of the upper body surface is positive, τ is inclined upward, and hence it gives a positive contribution to N'. For an upward inclined τ, θ would be counterclockwise, hence negative. Therefore, in Equation (4.6), $Sin\ \theta$ would be negative, making the shear stress term (the last term) a positive value, as it should be in this instance.

The total normal and axial forces *per unit span* are obtained by integrating Equations (4.6) to (4.9) from the leading edge (LE) to the trailing edge (TE):

$$N' = -\int_{LE}^{TE} (p_u Cos\theta + \tau_u Sin\theta) ds_u + \int_{LE}^{TE} (p_l Cos\theta - \tau_l Sin\theta) ds_l \quad (4.10)$$

$$A' = \int_{LE}^{TE} (-p_u Sin\theta + \tau_u Cos\theta) ds_u + \int_{LE}^{TE} (p_l Sin\theta - \tau_l Cos\theta) ds_l \quad (4.11)$$

In turn, the total lift and drag per unit span can be obtained by inserting Equations (4.10) and (4.11) into (4.4) and (4.5).

There are quantities of an even more fundamental nature than the aerodynamic forces themselves. These are *dimensionless force coefficients*. We have already defined a dimensional quantity called the free stream *dynamic pressure* as $q_\infty = ½\rho U_\infty^2$. In addition, let s be a reference area and l be a reference length. The dimensionless force coefficients are defined as follows:

Lift coefficient: $$C_L = \frac{L}{q_\infty S} \quad (4.12)$$

Drag coefficient: $$C_D = \frac{D}{q_\infty S}$$ (4.13)

Normal force coefficient: $$C_N = \frac{N}{q_\infty S}$$ (4.14)

Axial force coefficient: $$C_A = \frac{A}{q_\infty S}$$ (4.15)

In the above coefficients, the reference area S and reference length *I* are chosen to pertain to the given geometric body shape; for different shapes, S and *I* may be different things. For example, for an airplane wing, S is the planform area, and *I* is the mean chord length, as illustrated in Figure 4.6.

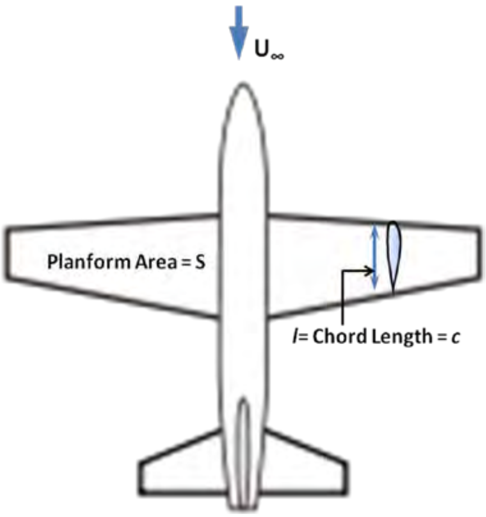

Figure 4.6: Reference Area and Length for Airplane

The symbols in capital letters listed above, i.e., C_L , C_D, C_N, and C_A , denote the force coefficients for a complete three-dimensional body such as an airplane or a finite wing. In contrast, for a two-dimensional body, the forces are per unit span. For these two dimensional bodies, it is conventional to denote the aerodynamic coefficients by lowercase letters as follows:

$$c_l = \frac{L'}{q_\infty c} \quad \text{and} \quad c_d = \frac{D'}{q_\infty c}$$

Where, the reference area S = *c(1)* = c.

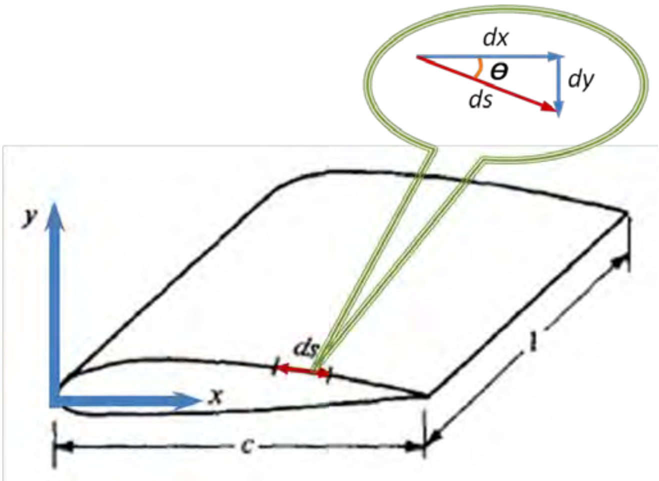

Figure 4.7: Geometrical Relationship of Differential Lengths

The most useful forms of Equations (4.10) and (4.11) are in terms of the dimensionless coefficients introduced above. From the geometry shown in Figure 4.7,

$$dx = dx\ Cos\ \theta$$

$$dy = -ds\ Sin\ \theta$$

$$S = c(1)=c$$

Substituting the above expressions of *dx, dy and S* into Equations (4.10) and (4.11), dividing by q_∞, we obtain the following integral forms for the force and moment coefficients:

$$c_n = \frac{1}{c}\int_0^c (c_{p,l} - c_{p,u})dx + \frac{1}{c}\int_0^c \left(c_{f,u}\frac{dy_u}{dx} + c_{f,l}\frac{dy_l}{dx}\right)dx \qquad (4.16)$$

$$c_a = \frac{1}{c}\int_0^c (c_{p,u}\frac{dy_u}{dx} - c_{p,l}\frac{dy_l}{dx})dx + \frac{1}{c}\int_0^c \left(c_{f,u} + c_{f,l}\right)dx \qquad (4.17)$$

Here, y_u is directed above the x axis, and hence is positive, whereas y_l is directed below the x axis, and hence is negative. Also, dy/dx on both the upper and lower surfaces follow the usual rule from calculus, i.e., positive for those portions of the body with a positive slope and negative for those portions with a negative slope. When shear stress due to viscous effect is neglected, an integration of a pressure distribution over an airfoil chord for both upper and lower surfaces is known to provide normal and axial force acting on an airfoil section [24, 34] as follows:

$$c_n = \frac{1}{c}\int_0^c (c_{p,l} - c_{p,u})dx \tag{4.18}$$

$$c_a = \frac{1}{c}\int_0^c (c_{p,u}\frac{dy_u}{dx} - c_{p,l}\frac{dy_l}{dx})dx \tag{4.19}$$

The known pressure coefficients from the experiment can be calculated for the normal and axial force by using a numerical integration of the above equations in the Trapezoidal approximating forms.

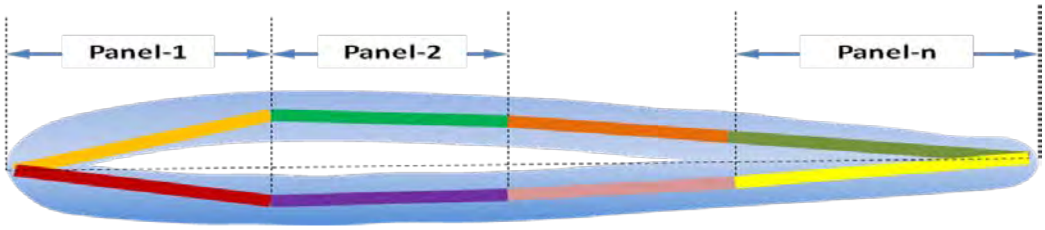

Figure 4.8: Paneling of the Wing Surface

As shown in Figure 4.8, both the surfaces of the wing section can be divided into small panels corresponding to a total of gaps between each pressure tap location [34]. When n is a number of panels, the equations can be converted to:

$$c_n = \sum_{i=1}^{n}\left[\left(c_{p,l,i} - c_{p,u,i}\right)\Delta\left(\frac{x_i}{c}\right)\right] \tag{4.20}$$

$$c_a = \sum_{i=1}^{n}\left[\left(c_{p,u,i}\frac{\Delta y_{u,i}}{\Delta x_i} - c_{p,l,i}\frac{\Delta y_{l,i}}{\Delta x_i}\right)\Delta\left(\frac{x_i}{c}\right)\right] \tag{4.21}$$

The interpolated and extrapolated pressure coefficients would be applied to Equation (3.20) and (3.21) in order to get the normal and axial force at a section of interest. Lift and drag coefficient can be obtained from:

$$c_l = c_n Cos\alpha - c_a Sin\alpha \tag{4.22}$$

$$c_d = c_n Sin\alpha + c_a Cos\alpha \tag{4.23}$$

The ove r-all va lue of t he c oefficients f or t he whole w ing can be f ound out b y averaging the same values of each segments of the wing along the span.

5. EXPERIMENTAL SETUP AND METHODOLOGY

5.1 Design and Construction

The aerodynamic characteristics (C_L, C_D and L/D) can be calculated from the surface pressure distribution of the wing as discussed in the previous chapter. To obtain the pressure distribution over the surfaces, wooden wing models are prepared with a specific aerofoil, suitable fixture is prepared to set the models in the wind tunnel and a multi-tube manometer is fabricated to take the pressure readings from the surfaces of the wing models.

5.1.1 Wing models

Using NACA 4412 aerofoil, wooden models for three wings are prepared having the same span (245 mm) and equal surface area (31115 mm^2) as shown in Figure 5.1.

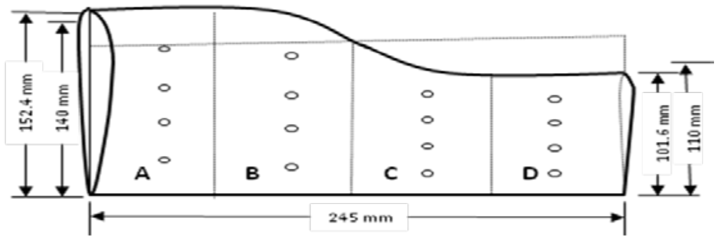

(a) Curved Leading Edge Planform

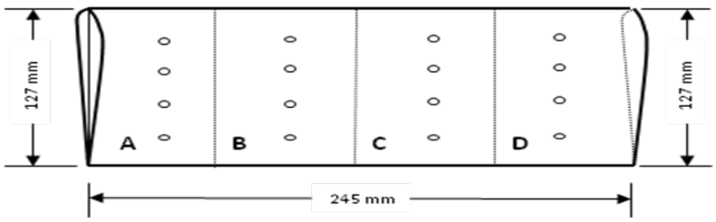

(b) Rectangular Planform (Reference)

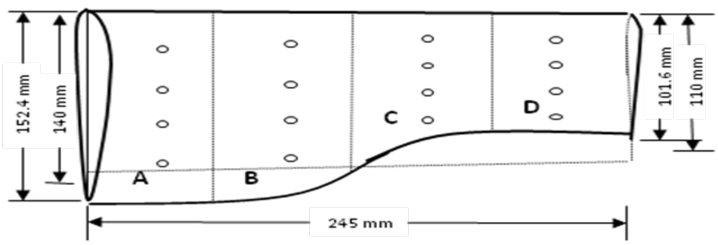

(c) Curved Trailing Edge Planform

Figure 5.1: Experimental Wing Models

Each model is provided with 32 pressure tapings along the span and chord (16 at upper surface & 16 at lower surface). Along the span the wings are divided into four equal segments (61.25 mm). For rectangular wing, the chord length is same (127 mm) for all the four segments but for the curved edge wings, the average chord length is different for different segments along the span (for segment A - 152.4 mm, for segment B- 140 mm, for segment C- 110 mm and for segment D- 101.6 mm). Thus, the ratio of root chord to tip chord of the curved edge planforms is 1.5. Four pressure tapping points at upper surface and four pressure tapping points at lower surface are made at 20% , 40 %, 60 % and 80% of the average chord length of each segment of all the wing models.

5.1.2 Pressure measuring device

The arrangement of multi-tube manometer for measuring the pressures is shown in Figure 5.2. The multi-tube manometer mainly consists of a water tank and 36 manometer glass tubes connected to the tapping points in wing model surfaces. The water tank is used to store the distilled water. Each limb is fitted with a scale graduated in mm to measure the difference of water height. The static pressure is calculated from the difference in water height.

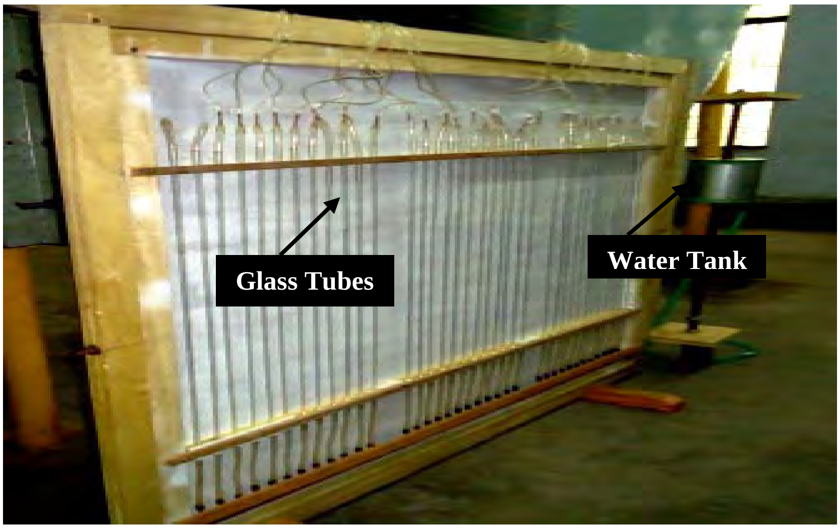

Figure 5. 2: Multi-tube Manometer

5.1.3 Fixture for altering angle of attack

The details of wind tunnel are shown in Figure 5.3. A fixture is fabricated and fixed in the test section of the wind tunnel as shown in Figure 5.4. The fixture facilitates the wing models to rotate and fix at any angle of attack. The wing models are tested at angle of attack from -4° to 24° with a step of 4°. Each model is rotated and fixed at the desired angle by seeing the preset scales (in degrees) pasted on the frame.

5.2 Experimental Setup

5.2.1 Wind tunnel

The experiment is carried out in a 700mm×700mm closed circuit wind tunnel as shown in Figure 5.3 available at turbulence lab of Department of Mechanical Engineering, BUET.

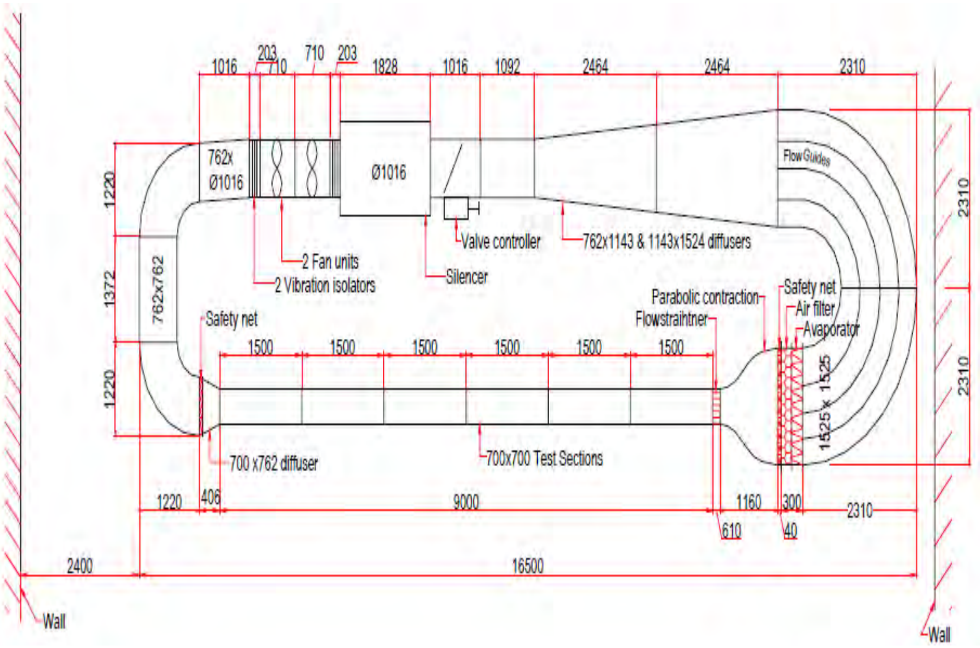

Figure 5. 3: Schematic Diagram of the Wind Tunnel at BUET's Turbulence Lab [35]

The wind speed is created by the two 700mm counter rotating fans. At the discharge of the fans there is a silencer to reduce the sound level. From the silencer air flow passes through the flow controlling butterfly valve, diffuser and the plenum chamber to stabilize the flow to certain level. The fan motors are powered by 400 V-3Φ-50Hz power supply through motor speed controller. Thus the wind speed in the tunnel can be varied both by controlling the fan motor speed as well as by controlling the butterfly valve [35]. To facilitate the present experiment in the open air condition the diffuser at the end of the test section is taken out and the discharge side of the test section is fitted with a 700mm×700mm discharge duct and a 1000mm×1000mm to 762mm×762mm bell mouth entry is added at the return duct to have smooth entry. Thus the 406mm open flow field created between the discharge duct and bell mouth entry become the experimental space as shown in Figure 5.4 where desired velocity is obtained.

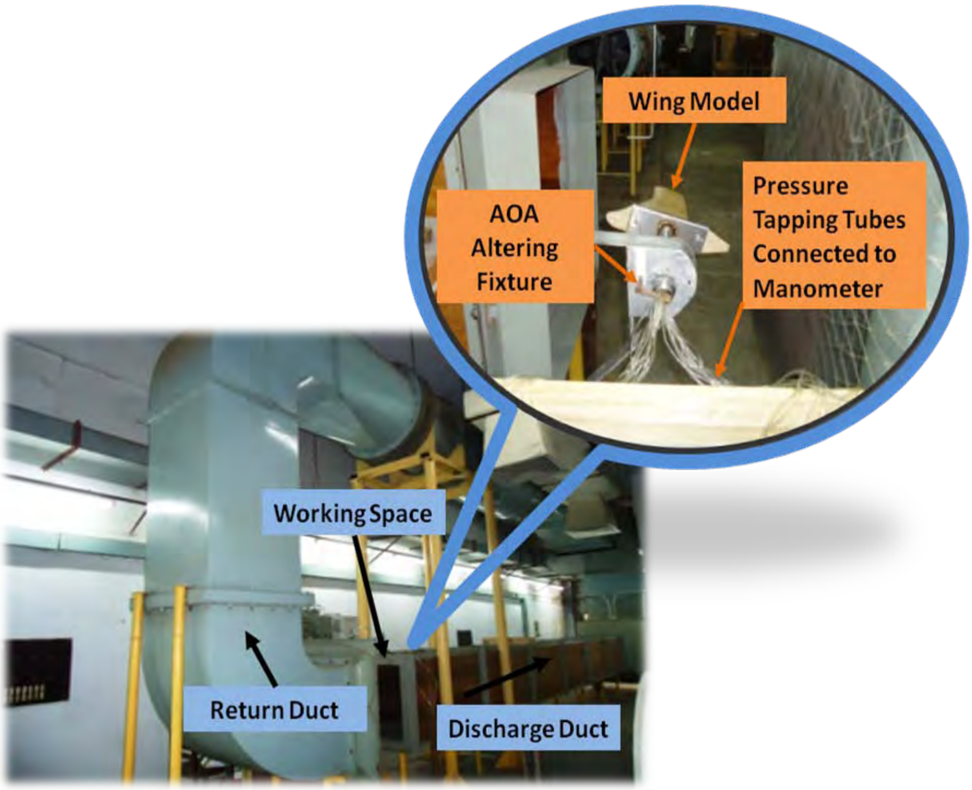

Figure 5. 4: Photograph of Experimental Set-up

5.2.2 Experimental parameters

All the experimental data are taken at room temperature of 35C and at air speed of 23.71 m/s (85.35 kph) and the air flow is considered incompressible throughout the experiment. Specific density of both air and water corresponding to room temperature is assumed to be 1.145 kg/m^3 and 994 kg/m^3 respectively.

5.3 Methodology

a. At first, the static pressure at different angles of attack (α = -4˚, 0˚, 4˚, 8˚, 12˚, 16˚, 20˚ & 24˚) are measured from both upper and lower surfaces of the wing models through different pressure tapings by using a multi-tube manometer during wind tunnel testing.

b. From the static pressure data, the respective coefficient of pressure (C_p) is calculated using equation (4.1) to (4.3).

c. The values of C_p of both surfaces of individual planforms are plotted in C_p versus %C graph to observe the pressure pattern of different segments of each planform along the chord length.

d. C_L and C_D of all the wing planforms at every angle of attack are determined from equation (4.20) to (4.23).

e. L/D at different angle of attack for all the wing models are obtained from the ratio of C_L to C_D at respective angle of attack.

f. At last, the lift characteristics, drag characteristics and lift to drag ratio of the wing planforms are analyzed and compared with each other from C_L versus α, C_D versus α and L/D versus α graphs.

6. RESULTS AND DISCUSSION

6.1 Data Collection and Analysis

To analyze aerodynamic characteristics of the wings with curved leading edge (L.E.) planform and curved trailing edge (T.E.) planform, the pressure coefficients of both upper and lower surfaces were measured through the wind tunnel testing. Then the pressure coefficients are plotted along chordwise positions (% C) at every angle of attack for each of the four segments. The pressure coefficients of a rectangular wing planform are also measured through the wind tunnel testing and those data are plotted in the same way in all the graphs as reference. Then surface pressure distribution of all the wing planforms are discussed making comparison with each other at every segment for every angle of attack. The resulting data, computed in terms of the normal and axial forces on the wing models, are used to determine coefficient of lift (C_L), coefficient of drag (C_D) and lift to drag ratio (L/D) of individual wing. Finally, lift characteristics, drag characteristics and lift to drag ratio for all three wing planforms are discussed making comparison with each other from C_L versus α, C_D versus α and L/D versus α plots respectively. Calculated values of pressure coefficients of all three planforms from -4° to 24° angles of attack are shown in Appendix-I. Uncertainties of experimental results are also analyzed in light of the procedure suggested by Cimbala [36]. The details of uncertainty analysis are shown in Appendix-II.

6.2 Surface Pressure Distribution

Pressure distribution of both upper and lower surfaces along the chord length of four segments (Segment-A, B, C and D) of three experimental wing planforms are plotted for -4^0, 0^0, 4^0, 8^0, 12^0, 16^0, 20^0 and 24^0 angle of attack. In the graphs, the horizontal axis represents the percentage of the chord length (%C) and the vertical axis represents the surface pressure coefficient (C_p). The vertical axis above the zero line (horizontal axis) represents the negative pressure coefficients or suction pressure coefficients and the vertical axis below the zero line represents the positive pressure coefficients. In the following sub-paragraphs, the said graphs are discussed in detail.

6.2.1 Pressure distribution at -4° angle of attack

Surface pressure distribution at -4° angle of attack for four segments of rectangular, curved L.E. and curved T.E. planforms are shown in Figure 6.1, 6.2, 6.3 and 6.4 respectively. In all the four figures, both upper and lower surface pressure coefficient, C_{pu} and C_{pl} are plotted along the chord. In Figure 6.1, it is observed that both upper and lower surface pressure of all the three planforms near the root (segment-A) are almost at the suction side. The lower surfaces are having more suction pressure than the upper surfaces near the leading edge up to 30~35 % C but from 40% C up to the trailing edge, the suction pressure of upper surfaces are greater than the suction pressure of lower surfaces. It is also observed that the lower surface pressure decreases from 10% C to 40% C rapidly and then decreases slowly up to 90% C for all the three planforms. For curved L.E. and curved T.E. planforms, the upper surface pressure increases up to 40% C and then slowly decreases up to 90% C but for rectangular planform the upper surface pressure remains almost constant throughout the chord length.

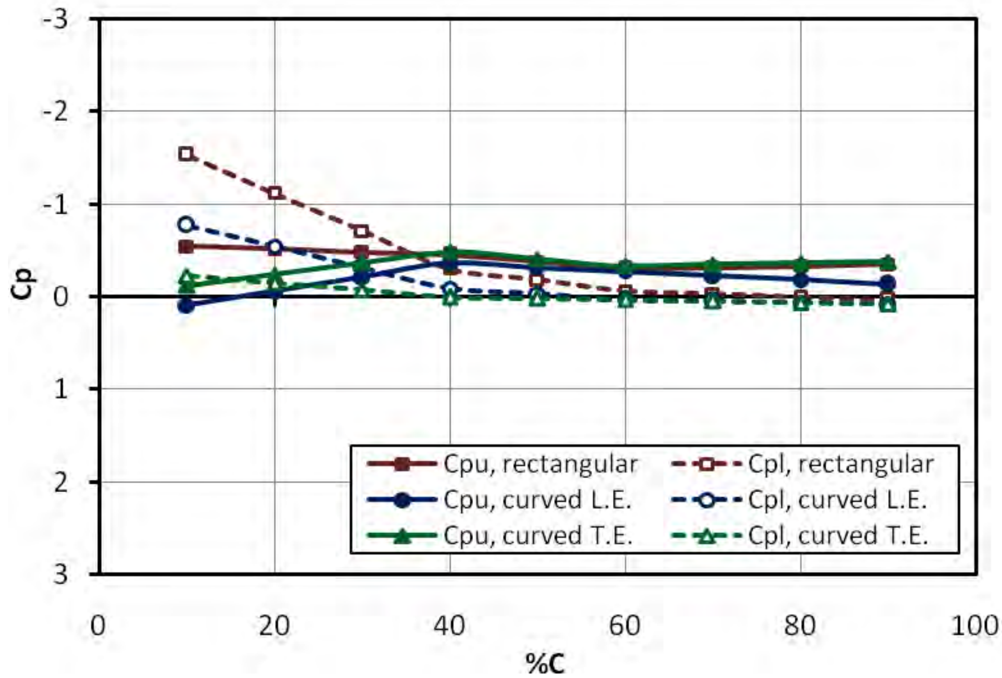

Figure 6.1: C_p Distribution of Segment-A at α = -4°

In Figure 6.2, upper and lower surface pressure distribution for segment-B of the three planforms are shown. The graph shows that both upper and lower surface pressure of all the three planforms at segment B are also almost at the suction side. For rectangular and curved L.E. planforms, the lower surfaces are having more suction pressure than the upper surfaces near the leading edge up to 30 % C but from 30 % C up to the trailing edge, the suction pressures of upper surfaces are greater than the suction pressure of lower surfaces. For curved T.E. planform, the suction pressure of the upper surface is greater than the suction pressure of the lower surface throughout the chord length (from leading edge to trailing edge). Up to 60 % C , the lower surface pressure curve is at the highest for rectangular planform, lowest for curved T.E. planform and in between for curved L.E. planform. Beyond 60 % C up to the trailing edge, the said curves are almost overlapping each other following the similar pattern.

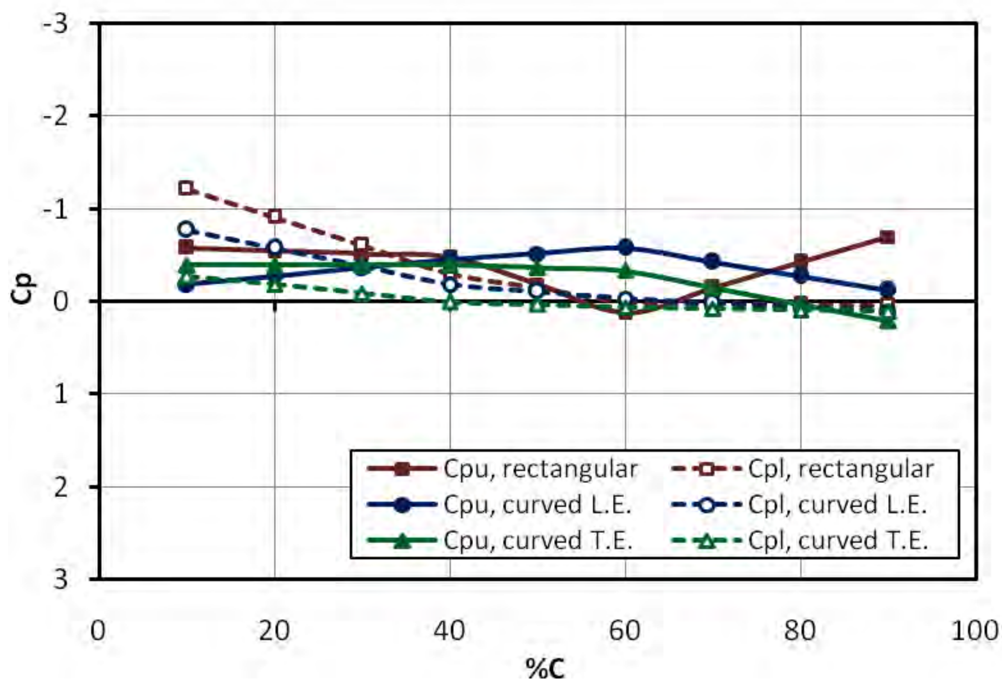

Figure 6.2: C_p Distribution of Segment-B at α = -4°

Up to 40 % C, the upper surface pressure curve of rectangular planform remain at the highest, curved L.E. planform at the lowest and curved T.E. planform is in between the rectangular and curved L.E. planforms. But from 40~80 % C, the upper surface pressure of curved L.E. planform is at the highest level, rectangular planform at the lowest and for curved T.E. planform it is in between rectangular and curved L.E. planforms. Again, from 80 % C towards the trailing edge, the upper surface pressure curve of the rectangular planform tends to reach to the higher level than the curved L.E. and curved T.E. planform.

Figure 6.3 shows the upper and lower surface pressure distribution for segment-C of the three planforms. For rectangular planform, the lower surface is having more suction pressure than the upper surface up to 40% C. The lower surface pressure decreases rapidly from 10% C to 40% C and then further decreases slowly up to the trailing edge.

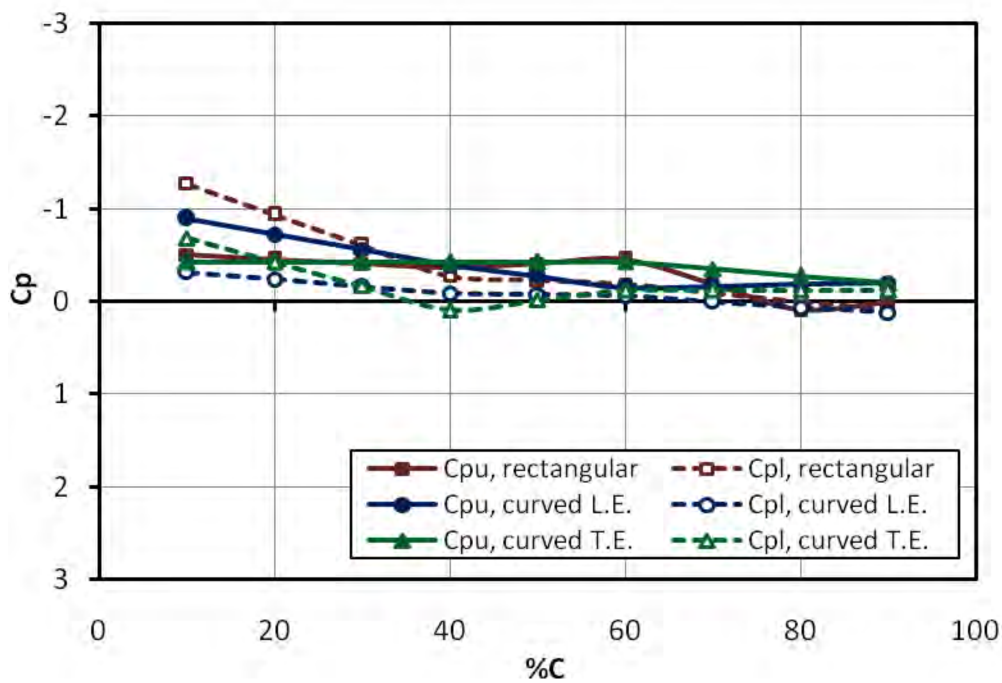

Figure 6.3: C_p Distribution of Segment-C at α = -4°

But the upper surface pressure remains constant from the leading edge up to 60% C and then slowly decreases up to the trailing edge. For curved L.E. planform, the upper surface is having more suction pressure than the lower surface throughout the chord length and both surfaces' pressure gradually decrease from the leading edge towards the trailing edge. The difference between the upper surface and lower surface pressure of curved L.E. planform is highest at 10% C and this difference gradually decreases up to 60% C and again increases slightly from 60% C to 90% C. For Curved T.E. planform, the lower surface suction pressure is greater than the upper surface suction pressure only up to 20% C and from 20% C up to the trailing edge upper surface is having greater suction pressure than the lower surface. The difference between the upper and lower surface pressure of the curved T.E. planform is observed at 40% C.

The surface pressure distributions for segment-D of the three planforms are shown in Figure 6.4. For rectangular planform, the lower surface is having more suction pressure than the upper surface only up to 20% C. The lower surface pressure decreases rapidly from 10% C to 40% C and then further decreases slowly up to the trailing edge. The upper surface pressure decreases slowly from 10% C up to 60% C and then increases up to the trailing edge. For curved L.E. planform, the upper surface is having more suction pressure than the lower surface throughout the chord length and both surfaces' pressure gradually decrease from the leading edge towards the trailing edge. The difference between the upper surface and lower surface pressure of curved L.E. planform is having the highest value from 60% C to 90% C. For Curved T.E. planform, the lower surface suction pressure is also greater than the upper surface suction pressure throughout the chord length. The difference between the upper and lower surface pressure of the curved T.E. planform is observed at 10% C. This difference gradually decreases up to 40% C and then slowly increases up to the trailing edge. The overall pressure difference between the two surfaces is highest for curved T.E. planform, lowest for rectangular planform and in between the highest and the lowest for curved L.E. planform in segment-D.

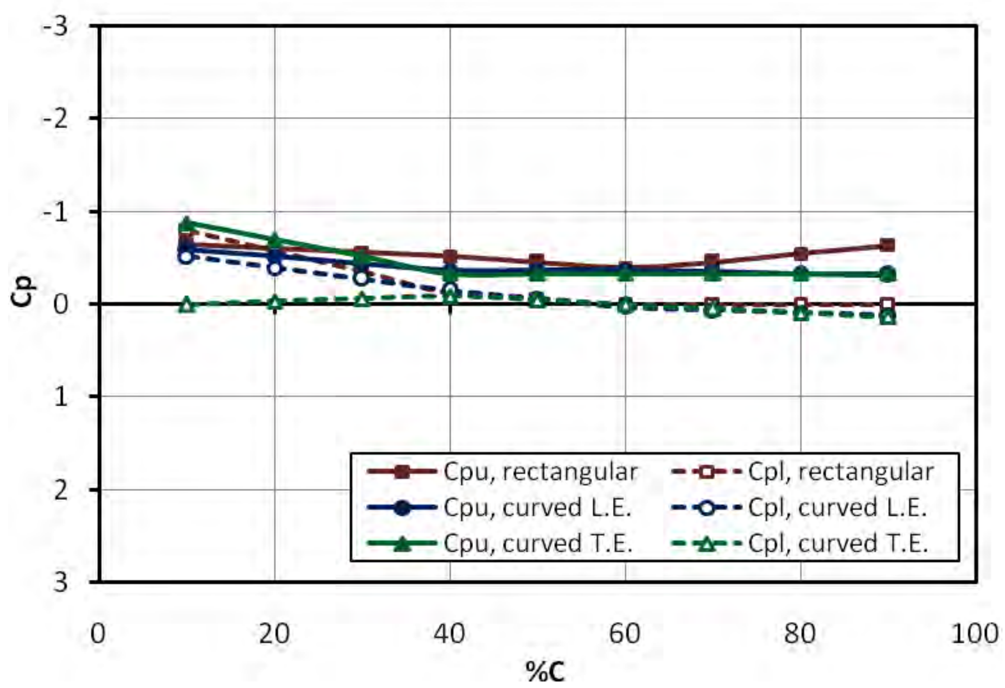

Figure 6.4: C_p Distribution of Segment-D at α = -4°

6.2.2 Pressure distribution at 0° angle of attack

Both upper and lower surface pressure coefficient, C_{pu} and C_{pl} at 0° angle of attack for four segments of rectangular, curved L.E. and curved T.E. planforms are plotted along the chord and shown in Figure 6.5, 6.6, 6.7 and 6.8 respectively.

The surface pressure distributions for segment-A of the three planforms at 0° angle of attack are shown in Figure 6.5. From the figure it is observed that upper surface of the rectangular planform is having higher suction pressure than it's lower surface pressure. For curved L.E. and curved T.E. planforms, the upper surface suction pressure is lower than the pressure of the lower surface up to 20% C but beyond 20%C up to the trailing edge upper surface suction pressure is higher than the lower surface pressure. The lower surface pressure of all the three planforms decreases from leading edge to trailing edge but the rate of reduction is higher up to 40% C. For rectangular planform, the upper surface pressure decreases gradually from leading edge to trailing edge. For both curved L.E. and curved T.E. planforms, upper surface pressure increases from the leading edge up to 40% C, then decreases towards the trailing edge. But the upper surface suction pressure of curved T.E. planform is higher than that of the curved L.E. planform and lower surface of curved T.E. planform is having greater positive pressure than the curved L.E. planform. The difference between the upper surface and lower surface pressure of both curved L.E. and curved T.E. planforms become maximum at 40% C.

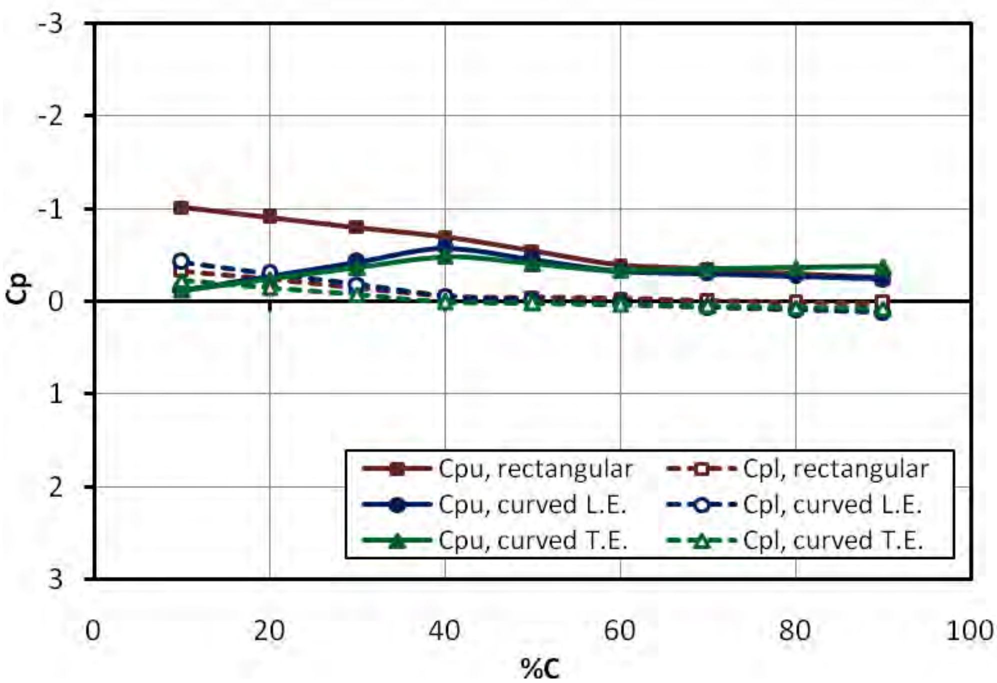

Figure 6.5: C_p Distribution of Segment-A at α = 0˚

The surface pressure distributions for segment-B of the three planforms at 0˚ angle of attack are shown in Figure 6.6. From the figure it is observed that upper surface of all the three planforms are having higher suction pressure than the lower surface pressure of the respective planforms except in case of rectangular planform at 60% C. At 60% C, the upper surface of the rectangular planform is having the positive pressure instead of suction pressure. For rectangular planform, the upper surface pressure decreases from 10% C and reaches to the positive value at 60% C, then again increases up to the trailing edge. The lower surface pressure remains almost constant throughout the chord. For curved L.E. planform, upper surface pressure increases slowly from the leading edge up to 60% C, then decreases towards the trailing edge rapidly. The lower surface pressure decreases from leading edge to trailing edge. The difference between the upper surface and lower surface pressure of curved L.E. planform becomes maximum at 60% C. In case of curved T.E. the upper surface pressure remains almost constant up to 60% C and then decreases towards the trailing edge. The lower surface pressure decreases from leading edge to trailing edge. The upper surface suction pressure of curved L.E. planform is higher than that of the curved T.E. planform and lower surface of both curved L.E. and curved T.E. planforms are having almost same pressure throughout the chord.

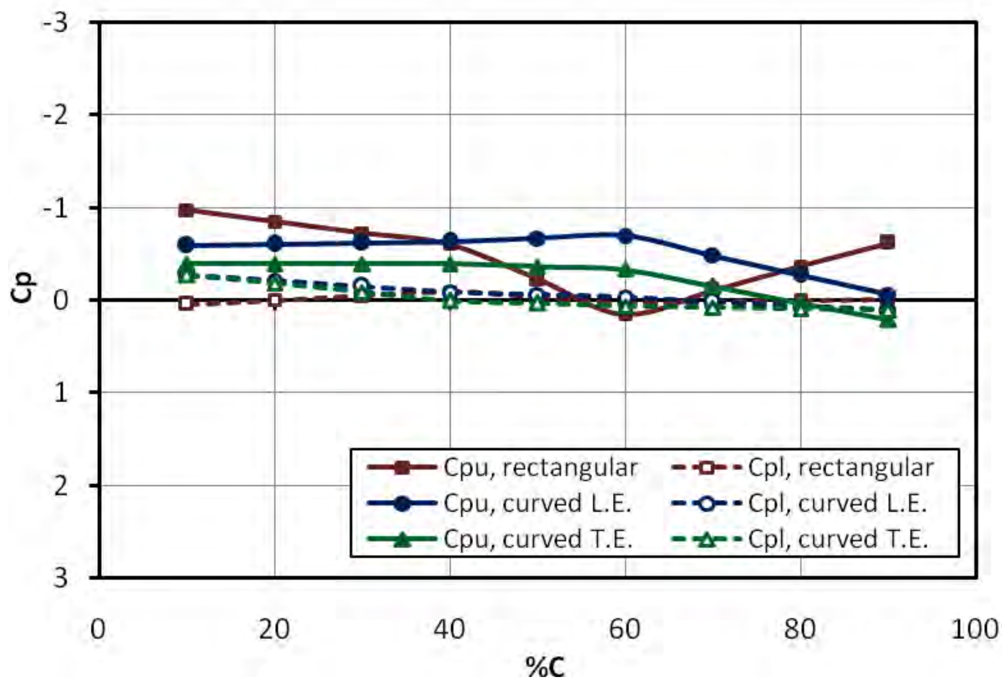

Figure 6.6: C_p Distribution of Segment-B at $\alpha = 0^\circ$

Figure 6.7 shows the upper and lower surface pressure distribution for segment-C of the three planforms. For rectangular planform, the lower surface is having more suction pressure than the upper surface up to 80% C. The lower surface pressure increases from 10 % C to 40 % C and then decreases slowly up to the trailing edge. For curved L.E. planform, the upper surface suction pressure is more than that of the lower surface. The upper surface pressure gradually reduces from leading edge to trailing edge. The lower surface pressure gradually decreases up to 40% C and then again increases. For curved T.E. planform, the upper surface suction pressure is lower than that of the lower surface up to 20% C and from 20% C to trailing edge the upper surface pressure is higher than the pressure of the lower surface. The upper surface pressure slowly increases from 10% C to 60% C and then gradually decreases up to the trailing edge. From 10% C the lower surface suction pressure rapidly decreases and reaches to the positive value at 40% C and again increases up to the trailing edge.

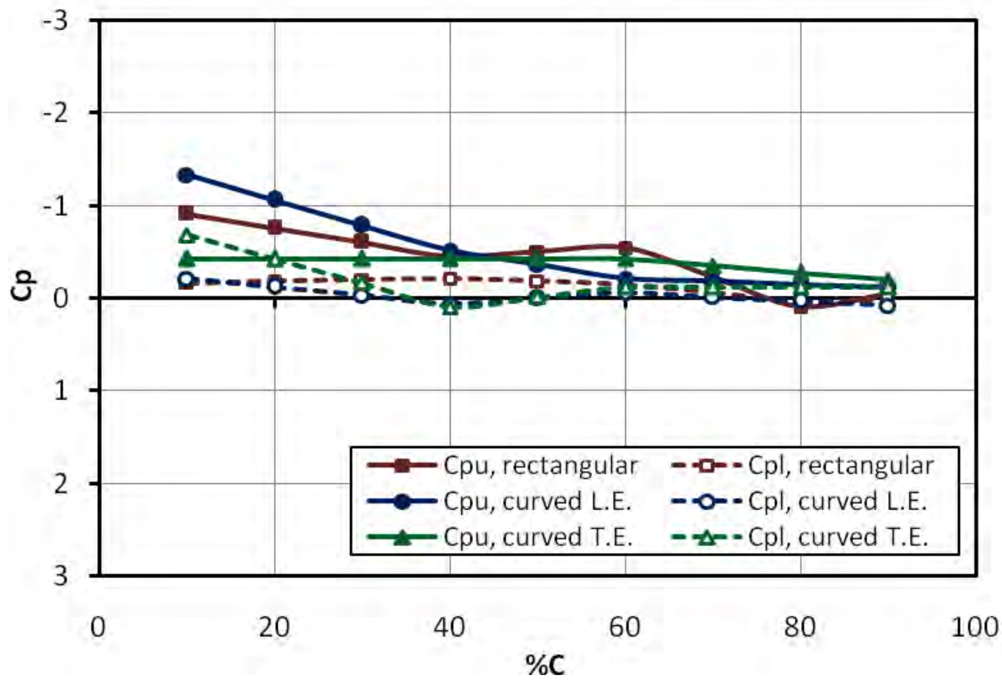

Figure 6.7: C_p Distribution of Segment-C at $\alpha = 0^{\circ}$

The surface pressure distributions for segment-D of the three planforms at 0° angle of attack are shown in Figure 6.8. From the figure it is observed that upper surface of all the three planforms are having higher suction pressure than the lower surface pressure of the respective planforms. For rectangular planform, the upper surface pressure decreases from 10% C to 60% C and then again increases up to the trailing edge. The lower surface pressure also reduces up to 60% C and then remains almost constant up to the trailing edge. For curved L.E. planform, both the upper and lower surface pressure decreases from the leading edge to the trailing edge. The difference between the upper surface and lower surface pressure of curved L.E. planform is observed maximum at 10% C. In case of curved T.E. planform, the upper surface pressure decreases up to 60% C and then remains almost constant up to the trailing edge. The lower surface pressure increases slightly from leading edge to 40% C and finally reaches to the positive value at 90% C. Out of the three planforms, the upper surface of the curved T.E. planform is having the lowest suction pressure but it's lower surface is having the highest pressure.

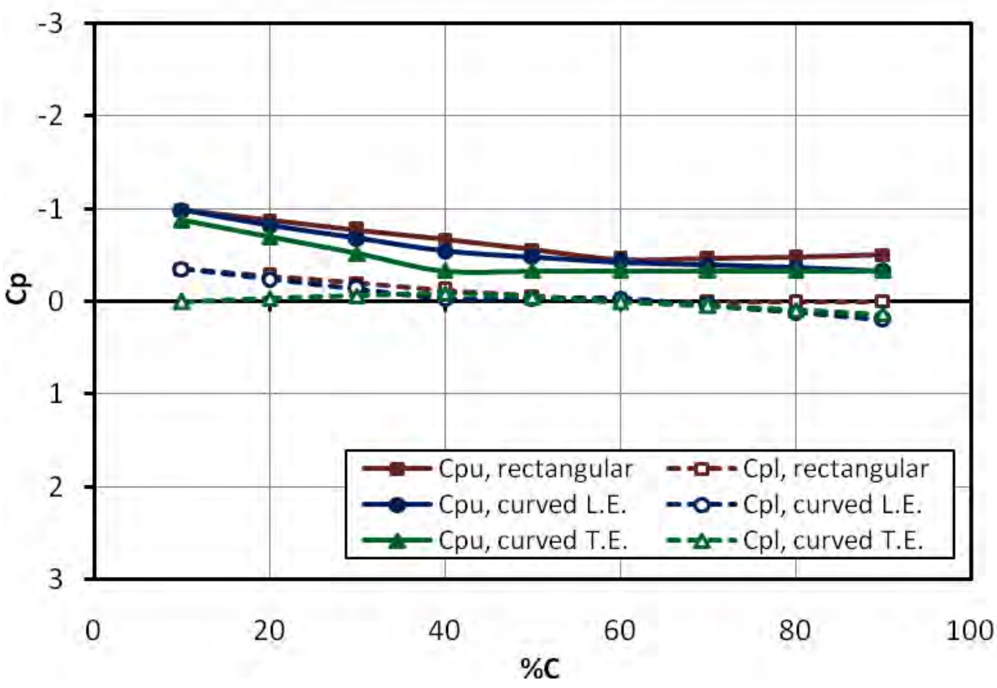

Figure 6.8: C_p Distribution of Segment-D at $\alpha = 0^{\circ}$

6.2.3 Pressure distribution at 4° angle of attack

Figure 6.9, 6.10, 6.11 and 6.12 show the pressure distribution of both upper and lower surface of rectangular, curved L.E. and curved T.E. planforms at 0° angle of attack for four segments respectively.

From Figure 6.9 it is observed that pressure difference between the upper and lower surface of rectangular planform in segment-A is the highest amongst all the three planforms. Because, the upper surface pressure of the rectangular planform is higher than that of curved L.E. and curved T.E. planforms up to 40% C. Another observation is that the pressure difference between the two surface of curved T.E. planform is greater than that of curved L.E. planform because of greater pressure difference near the trailing edge of curved T.E. planform.

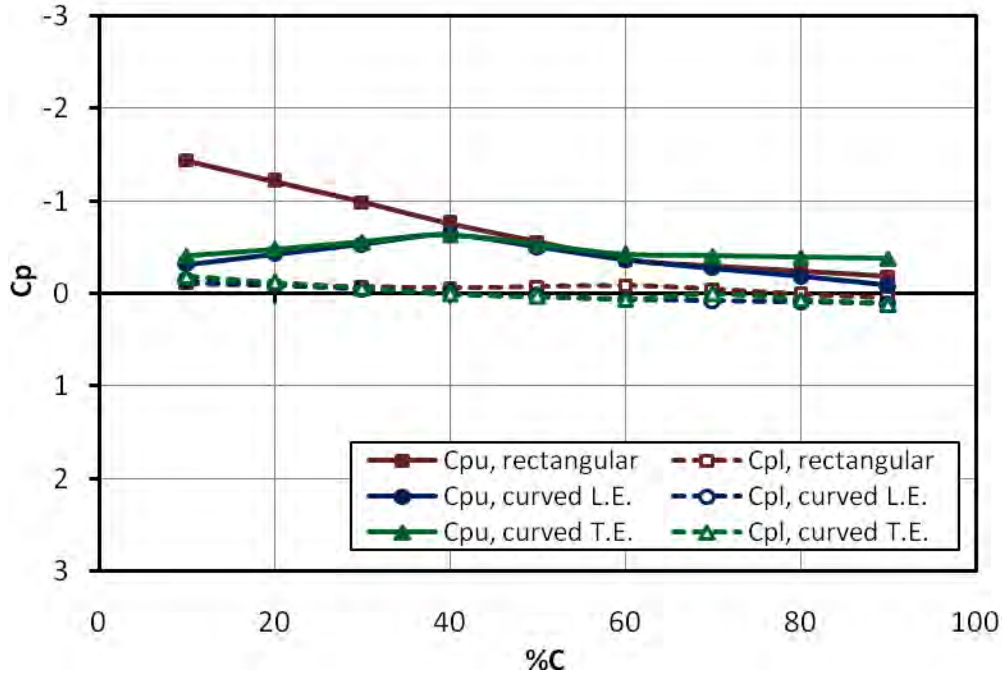

Figure 6.9: C_p Distribution of Segment-A at $\alpha = 4^{\circ}$

In Figure 6.10, it is observed that the upper surface pressure of the rectangular planform in segment-B rapidly decreases from the highest suction pressure at 10% C to the positive pressure at 60% C then again the pressure reaches to the suction side at 90% C. But in case of both curved L.E. and curved T.E. planforms, the upper surface pressure always remain at suction side. The differene between upper and lower surface pressure is observed lowest for rectangular planform and highest for curved T.E. planform. The upper surface pressure of both curved L.E. and curved T.E. planforms decrease very slowly from 10% C to 60% C and then decreases rapidly up to 90% C. The upper surface pressure of curved L.E. planform is lower than the upper surface pressure of curved T.E. planform. The lower surface of curved L.E. planform is having lower positive pressure than that of curved T.E. planform.

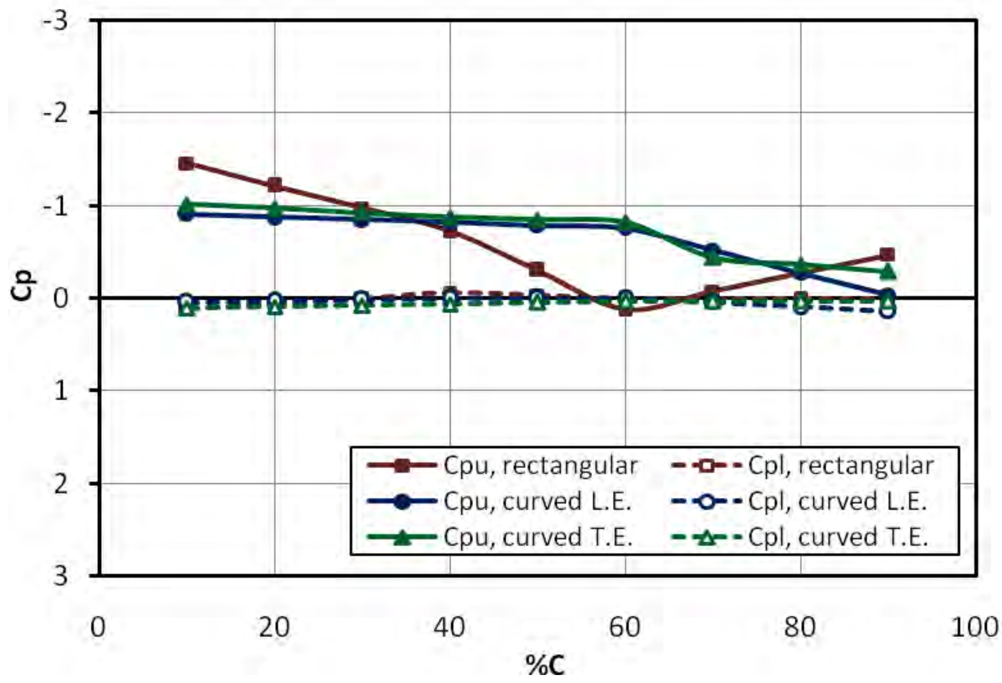

Figure 6.10: C_p Distribution of Segment-B at $\alpha = 4^{\circ}$

Figure 6.11 shows the pressure distribution of segment-C of all the three planforms. From the figure, it is observed that the upper surface suction pressure is highest for curved T.E. planform throughout the chord and lowest for the rectangular planform. The lower surface pressure of curved T.E. planform is also highest amongst the three planforms. The lower surface pressure for rectangular planform mostly remains at the suction side whereas the lower surface pressure of both curved L.E. and curved T.E. planform remain at the positive pressure side. As a result, the pressure difference between the upper and lower surface of curved T.E. is also at the highest level. In Figure 6.12, almost similar type of pressure distribution of all three planforms for segment-D are observed as in segment-C. But the difference between two surfaces pressure of respective planforms is lower than that of segment-C.

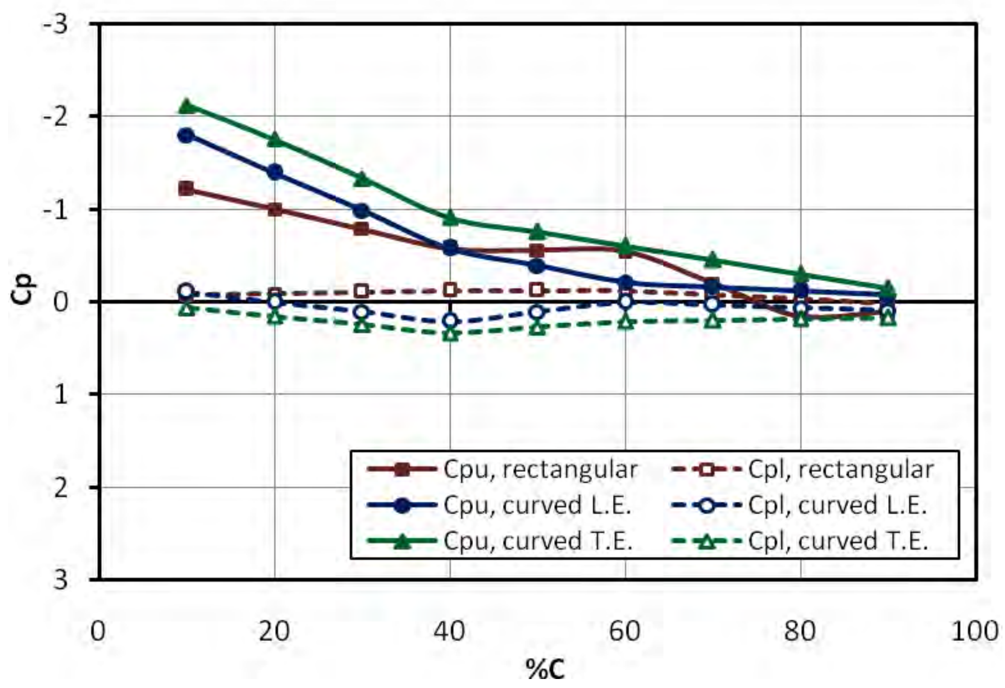

Figure 6.11: C_p Distribution of Segment-C at $\alpha = 4^{\circ}$

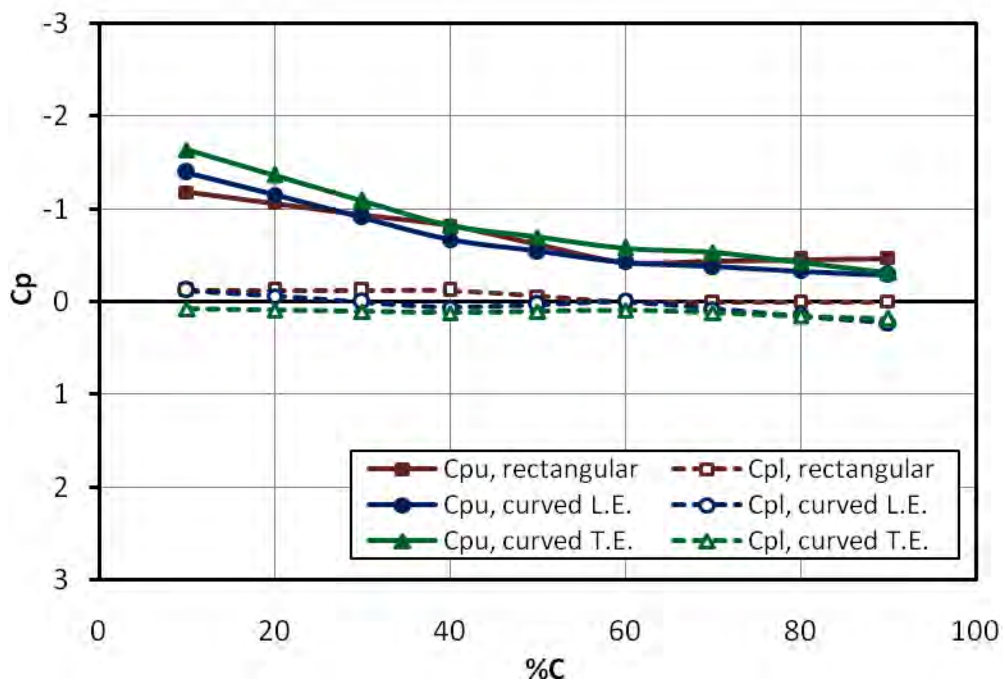

Figure 6.12: C_p Distribution of Segment-D at α = 4°

6.2.4 Pressure distribution at 8° angle of attack

Both upper and lower surface pressure coefficient, C_{pu} and C_{pl} at 8° angle of attack for four segments of rectangular, curved L.E. and curved T.E. planforms are plotted along the chord and shown in Figure 6.13, 6.14, 6.15 and 6.16 respectively.

The surface pressure distributions for segment-A of the three planforms at 8° angle of attack are shown in Figure 6.13. From the figure it is observed that upper surface of all the three planforms are having higher suction pressure than the lower surface pressure of the respective planforms. For rectangular planform, the lower surface pressure decreases slowly from 10% C to 40% C, then further decreases slowly up to 60% C and again increases up to the trailing edge. The upper surface pressure decreases gradually from leading edge to trailing edge. For both curved L.E. and curved T.E. planforms, upper surface pressure increases from the leading edge up to 40% C, then decreases towards the trailing edge and the lower surface pressure decreases from leading edge to trailing edge. The difference between the upper surface and lower surface pressure of curved L.E. planform becomes maximum at 40% C. But the upper surface suction pressure of curved T.E. planform is higher than that of the curved L.E. planform and lower surface of curved T.E. planform is having greater positive pressure than the curved L.E. planform.

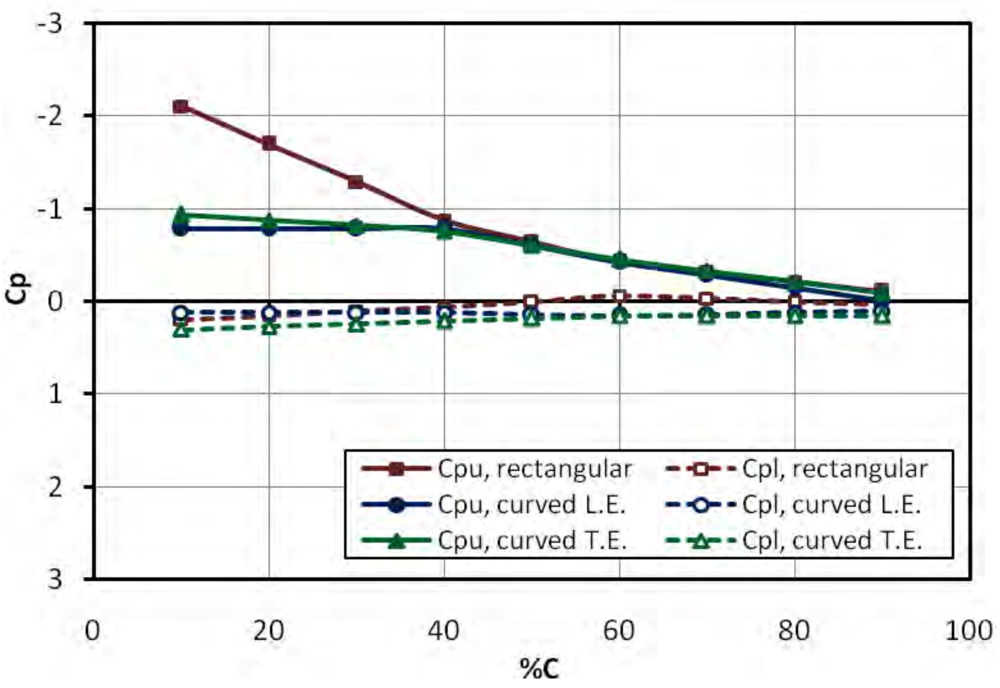

Figure 6.13: C_p Distribution of Segment-A at α = 8°

In Figure 6.14, it is observed that the upper surface pressure of the rectangular planform in segment-B rapidly decreases from the highest suction pressure at 10% C to the positive pressure at 60% C then again the pressure rises to the suction side at 90% C. But in case of both curved L.E. and curved T.E. planforms, the upper surface pressure always remain at suction side. The differene between upper and lower surface pressure is observed lowest for rectangular planform and highest for curved T.E. planform. The upper surface pressure of both curved L.E. and curved T.E. planforms decrease from 10% C to 90% C. The upper surface pressure of curved L.E. planform is lower than the upper surface pressure of curved T.E. planform. The lower surface of curved L.E. planform is having lower positive pressure than that of curved T.E. planform.

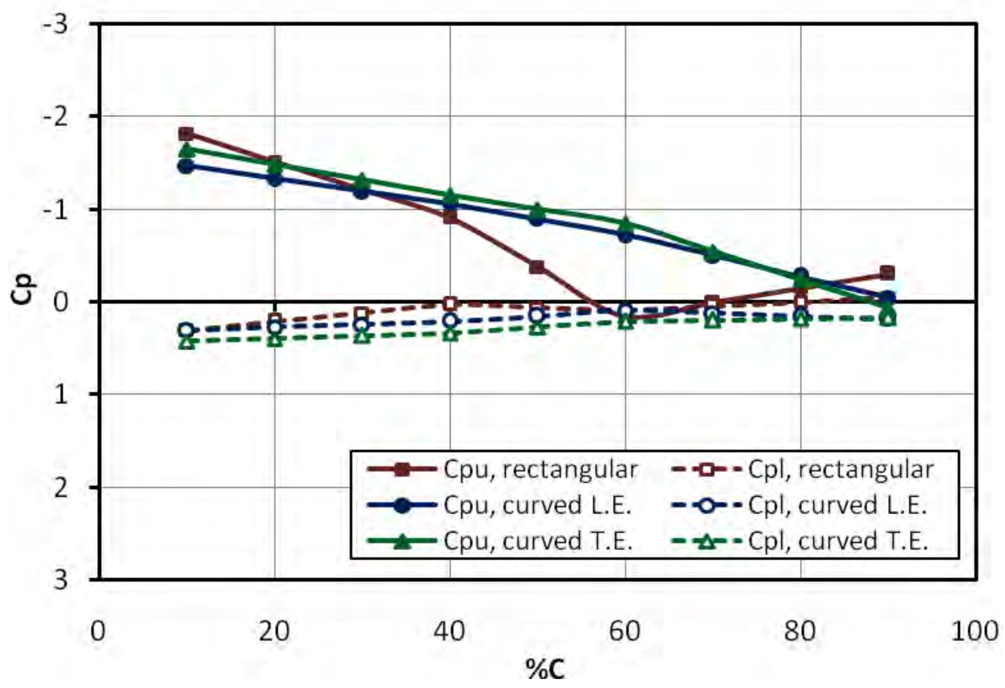

Figure 6.14: C_p Distribution of Segment-B at $\alpha = 8^{\circ}$

Figure 6.15 and Figure 6.16 show the pressure distribution of segment-C and segment-D of all the three planforms respectively. From the figures, it is observed that the upper surface suction pressure is highest for curved T.E. planform throughout the chord and lowest for the rectangular planform. The lower surface pressure of curved T.E. planform is also highest amongst the three planforms. The lower surface pressure for rectangular planform mostly remains at the suction side whereas the lower surface pressure of both curved L.E. and curved T.E. planform remain at the positive pressure side. As a result, the pressure difference between the upper and lower surface of curved T.E. is also at the highest level. In segment-D, the difference between two surfaces' pressure of respective planforms are lower than those of segment-C.

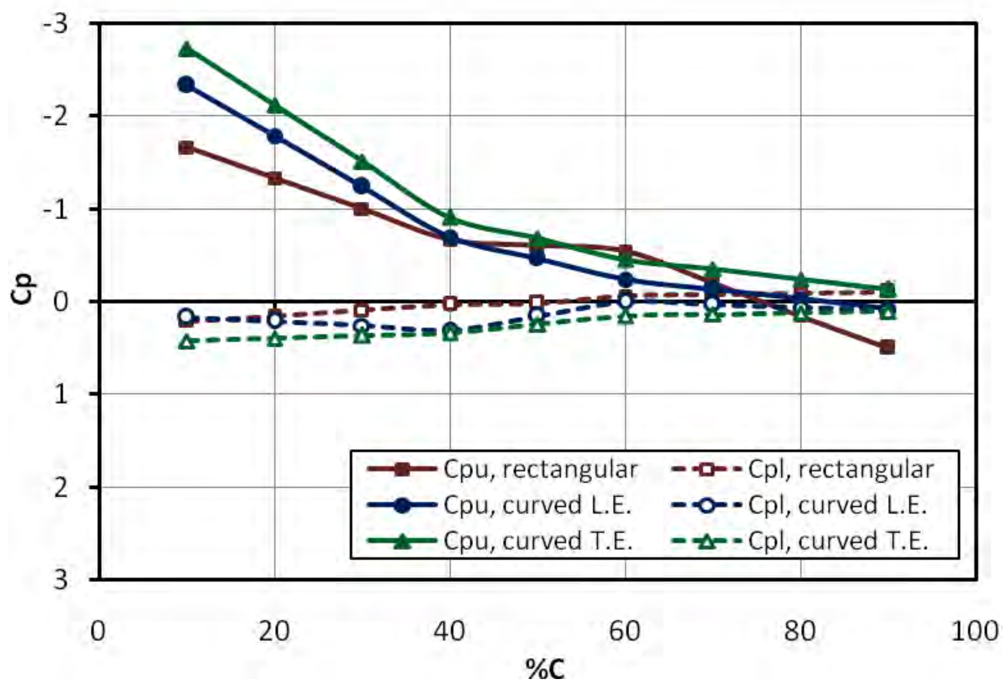

Figure 6.15: C_p Distribution of Segment-C at $\alpha = 8^{\circ}$

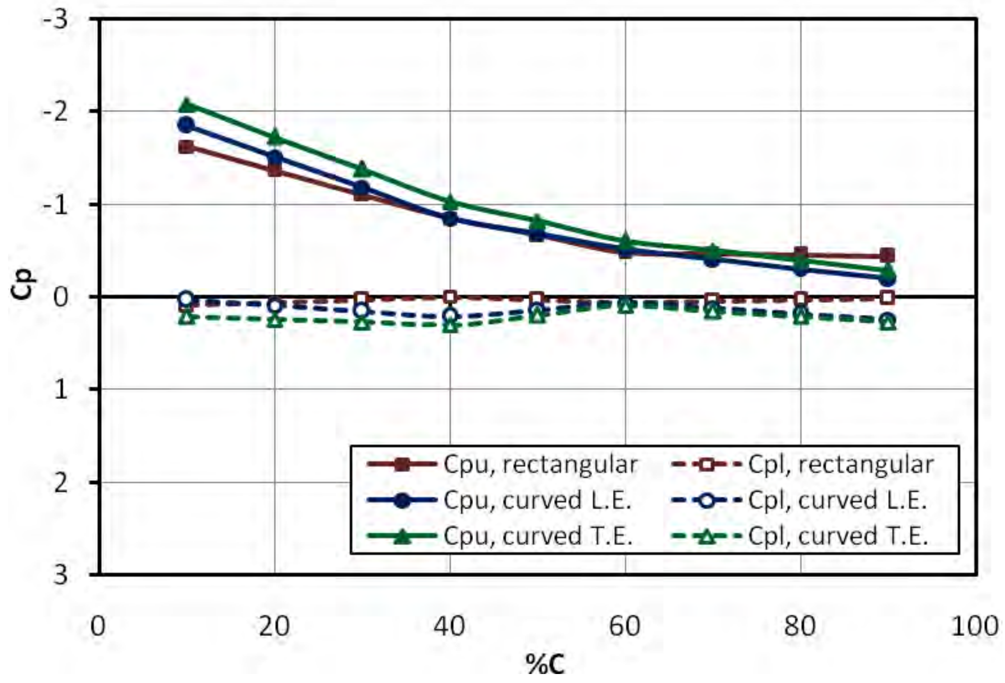

Figure 6.16: C_p Distribution of Segment-D at $\alpha = 8^{\circ}$

6.2.5 Pressure distribution at 12° angle of attack

Surface pressure distribution at 12° angle of attack for four segments of rectangular, curved L.E. and curved T.E. planforms are plotted along the chord and shown in Figure 6.17, 6.18, 6.19 and 6.20 respectively.

The surface pressure distributions for segment-A of the three planforms at 12° angle of attack are shown in Figure 6.17. From the figure it is observed that upper surface of all the three planforms are having higher suction pressure than the lower surface pressure of the respective planforms. For rectangular planform, the lower surface pressure increases slowly from 10% C up to the trailing edge. The upper surface pressure decreases gradually from leading edge to trailing edge. For curved L.E. planform, upper surface pressure increases from the leading edge up to 40% C, then decreases towards the trailing edge and the lower surface pressure increases from leading edge to trailing edge.

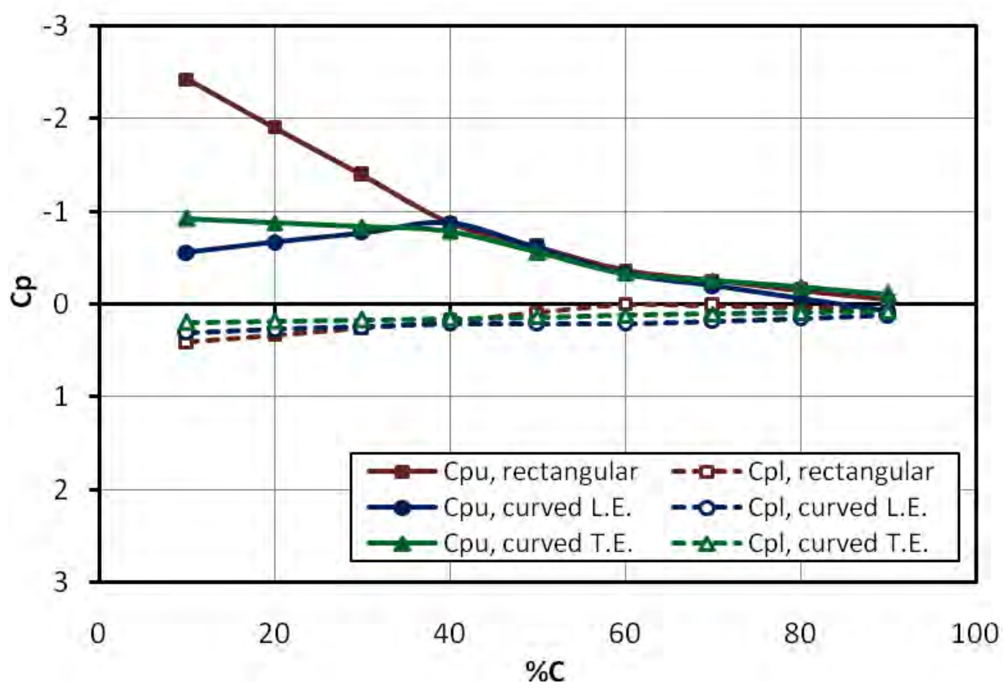

Figure 6.17: C_p Distribution of Segment-A at $\alpha = 12^{\circ}$

For curved T.E. planform, upper surface pressure decreases from 10% C towards the trailing edge and the lower surface pressure increases from leading edge to trailing edge. The difference between upper surface and lower surface pressure is observed maximum for rectangular planform. The upper surface suction pressure of curved T.E. planform is higher than that of the curved L.E. planform up to 30% C and lower surface of curved T.E. planform is having slightly lower positive pressure than the curved L.E. planform.

Figure 6.18, Figure 6.19 and Figure 6.20 show the pressure distribution of segment-B, segment-C and segment-D of all the three planforms respectively. From Figure 6.18, it is observed that the upper surface suction pressure of all three planforms reduces from leading edge to trailing edge and the lower surface positive pressure reduces from leading edge to trailing edge in segment-B. Thus the pressure difference between upper and lower surface is maximum near the trailing edge at 10% C. Also, the overall pressure difference between upper and lower surface is maximum for rectangular planform and lowest for curved T.E. planform in segment-B. But in segment-C, the difference between upper and lower surface pressure becomes maximum for curved T.E. planform as shown in Figure 6.19. Because in segment-C, the upper surface suction pressure of rectangular planform and curved L.E. planform reduces rapidly from leading edge up to trailing edge but for curved T.E. planform, the upper surface pressure reduces very slowly up to the trailing edge. In segment-D, overall pressure difference between upper and lower surface of all the three planforms seems equal as shown in Figure 6.20. From Figure 6.20, it is also observed that the upper surface suction pressure of all the three planforms reduces more rapidly up to 40% C and the lower surface positive pressure increases rapidly up to 60% C. From 60% C to 90% C, the difference between two surfaces' pressure of individual planform changes very slowly.

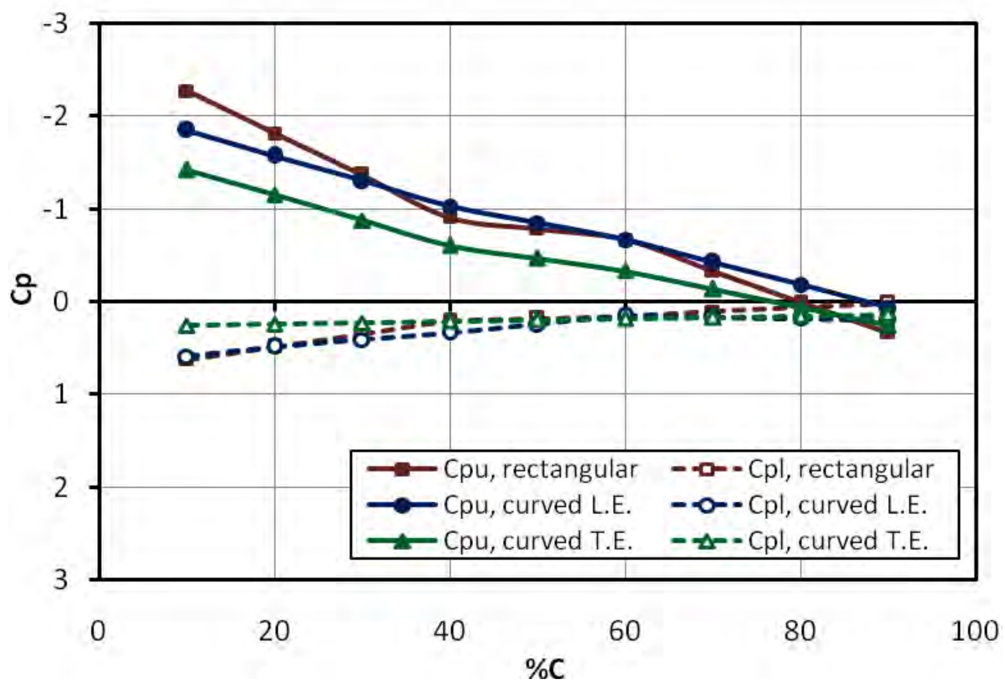

Figure 6.18: C_p Distribution of Segment-B at $\alpha = 12^{\circ}$

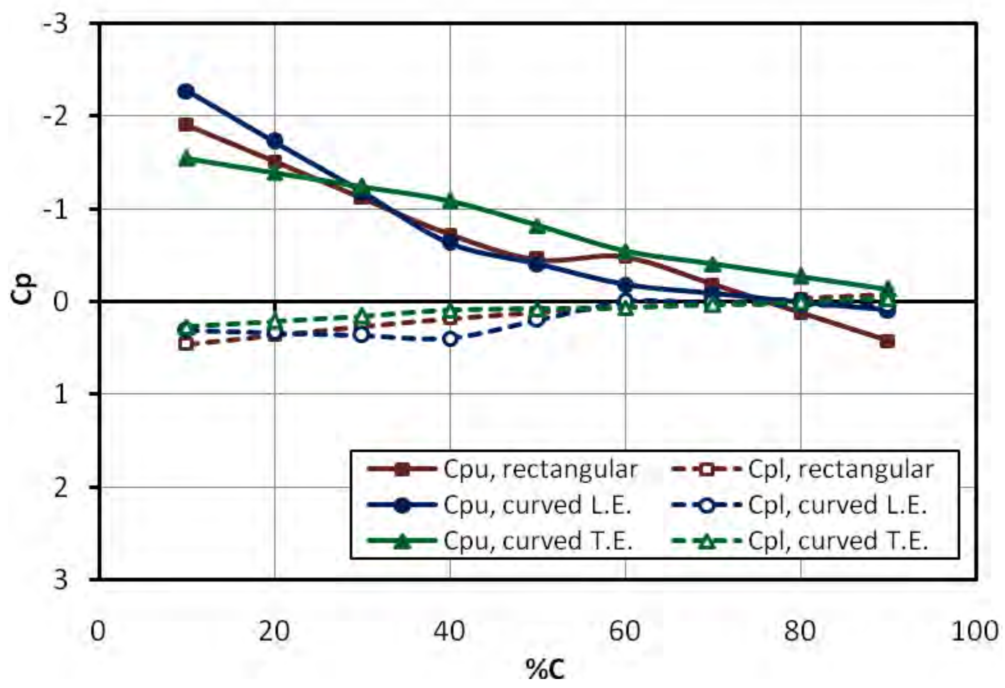

Figure 6.19: C_p Distribution of Segment-C at $\alpha = 12^{\circ}$

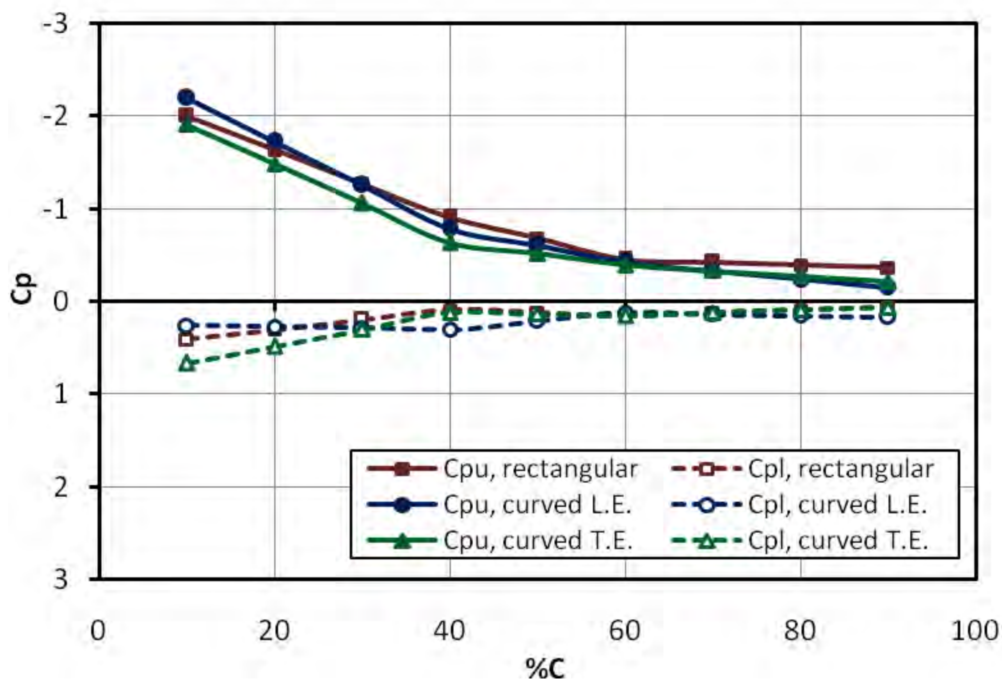

Figure 6.20: C_p Distribution of Segment-D at α = 12°

6.2.6 Pressure distribution at 16° angle of attack

Surface pressure distribution along the chord at 16° angle of attack for four segments of rectangular, curved L.E. and curved T.E. planforms are shown in Figure 6.21, 6.22, 6.23 and 6.24 respectively.

Pressure distribution along the chord for segment-A is shown in Figure 6.21. From the graph it is observed that upper surface suction pressure of rectangular planform decreases from 10% C to 40% C rapidly, then decreases slowly up to 60% C and again increases up to 90% C. The lower surface positive pressure gradually decreases up to 60% C and finally reaches to the suction side from 60% C to 90% C. For curved L.E. planform, the upper surface suction pressure reduces gradually from leading edge to trailing edge and its lower surface positive pressure increases gradually from leading edge to trailing edge. For curved T.E. planform, the upper and lower surface pressure curves follow the similar pattern as those of curved L.E. planform. But upper surface of curved T.E. planform is having greater suction pressure than that of curved L.E. planform and the lower surface of curved T.E. planform is having greater positive pressure than that of the curved L.E. planform. Thus, curved T.E. planform is having greater pressure difference between its two surfaces than that of curved L.E. planform. From the graph it is evident that the pressure difference between two surfaces of curved T.E. planform is also higher than the pressure difference between the surfaces of rectangular planform.

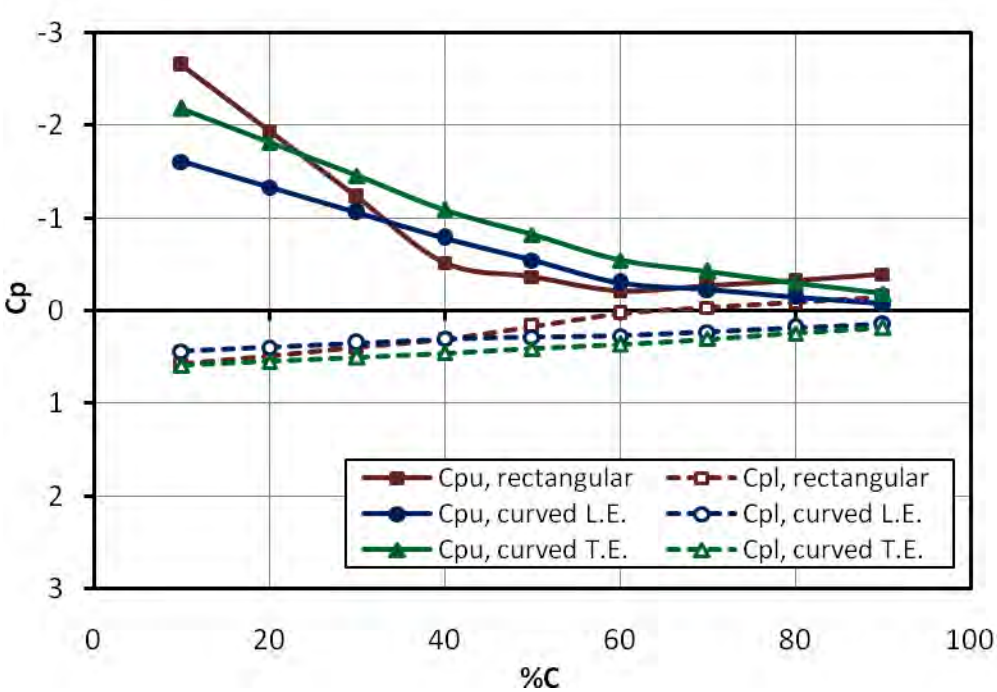

Figure 6.21: C_p Distribution of Segment-A at $\alpha = 16^{\circ}$

Similarly, Figure 6.22, 6.23 and 6.24 shows the surface pressure distribution of segment B, C and D respectively for all the three planforms at 16° angle of attack. From the figures it is observed that pressure difference between the surfaces of curved T.E. planform is higher than that of other two planforms in segment B, C and D.

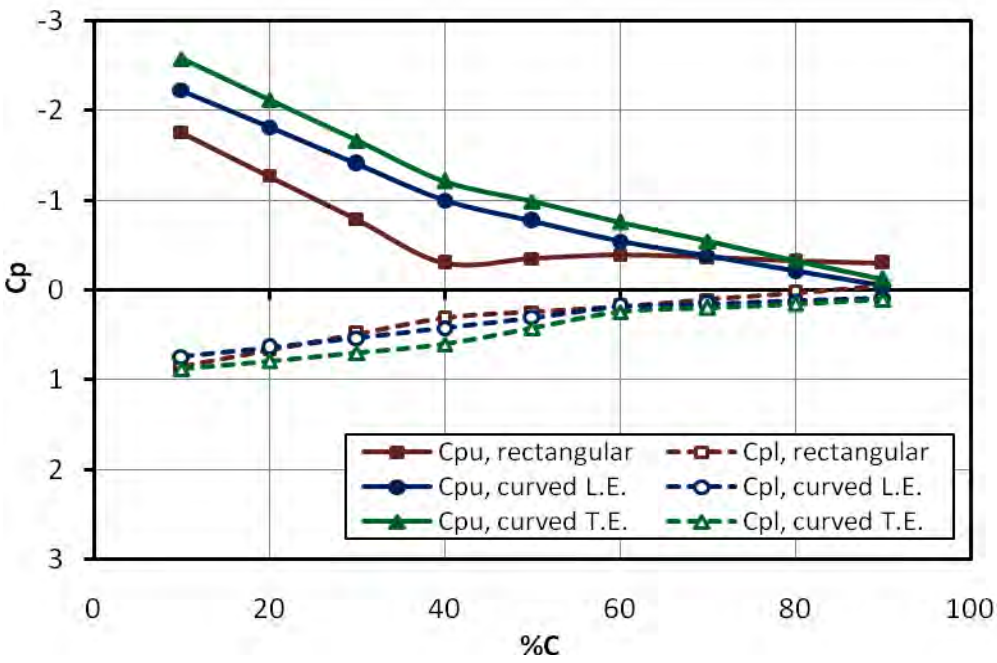

Figure 6.22: C_p Distribution of Segment-B at α = 16°

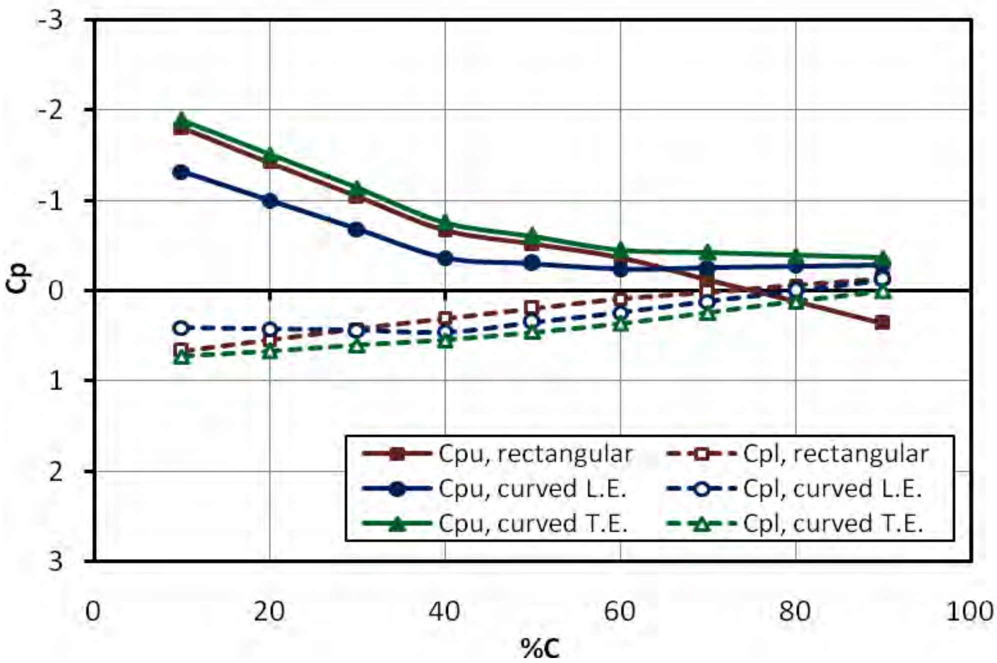

Figure 6.23: C_p Distribution of Segment-C at α = 16°

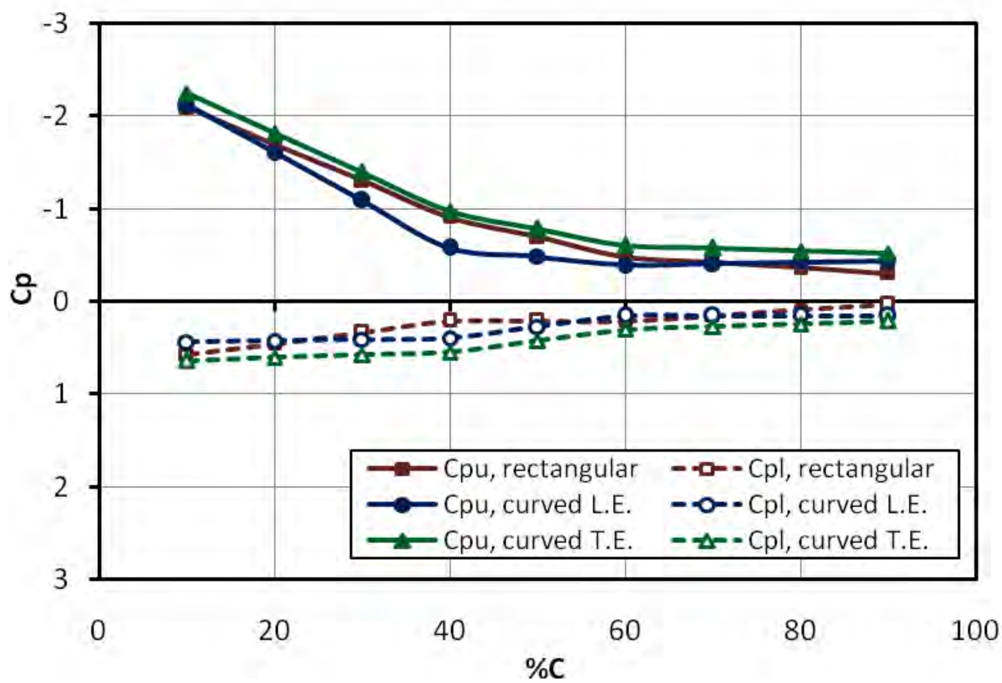

Figure 6.24: C_p Distribution of Segment-D at $\alpha = 16^{\circ}$

6.2.7 Pressure distribution at 20° angle of attack

Figure 6.25, 6.26, 6.27 and 6.28 shows the surface pressure distribution along the chord at 20° angle of attack for four segments of rectangular, curved L.E. and curved T.E. planforms respectively. From all the four figures, it is observed that in all the four segments, the upper surface suction pressure of the rectangular planform is very much lower than the upper surface suction pressure at previous angle of attack (16° and below) as shown in the previous figures. For curved L.E. planform and curved T.E. planform, the reduction in upper surface suction pressure is noticed comparatively less than those at the previous angle of attack. In Figure 6.25 and Figure 6.26, the difference between the upper and lower surface pressure of curved L.E. planform is observed maximum for segment-A and segment-B. But in segment-C and segment-D, the said difference is maximum for curved T.E. planform as shown in Figure 6.27 and Figure 6.28.

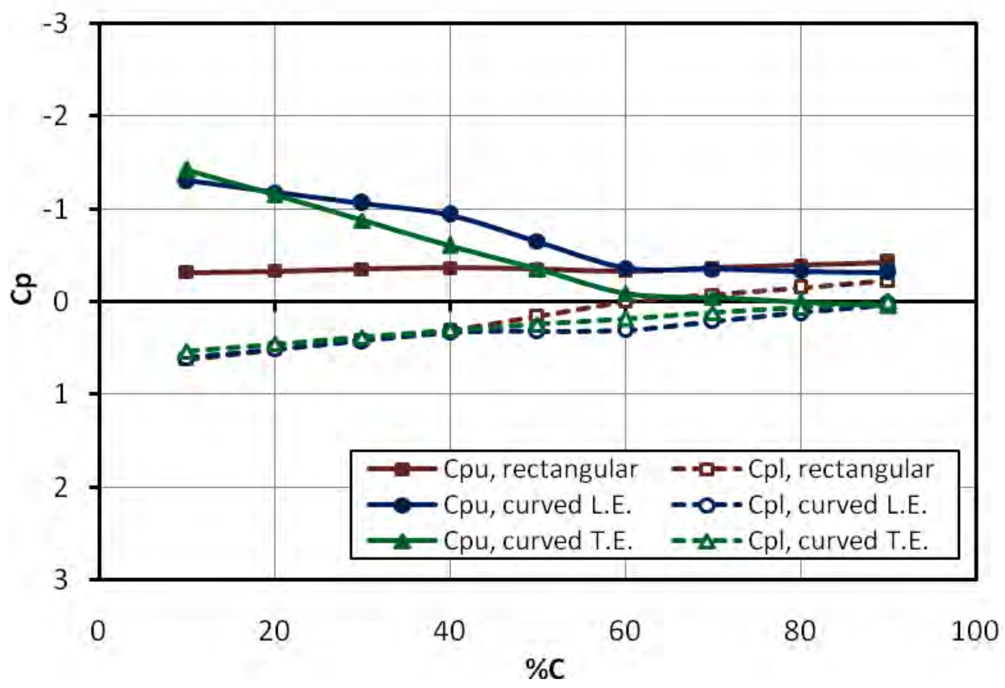

Figure 6.25: C_p Distribution of Segment-A at $\alpha = 20^{\circ}$

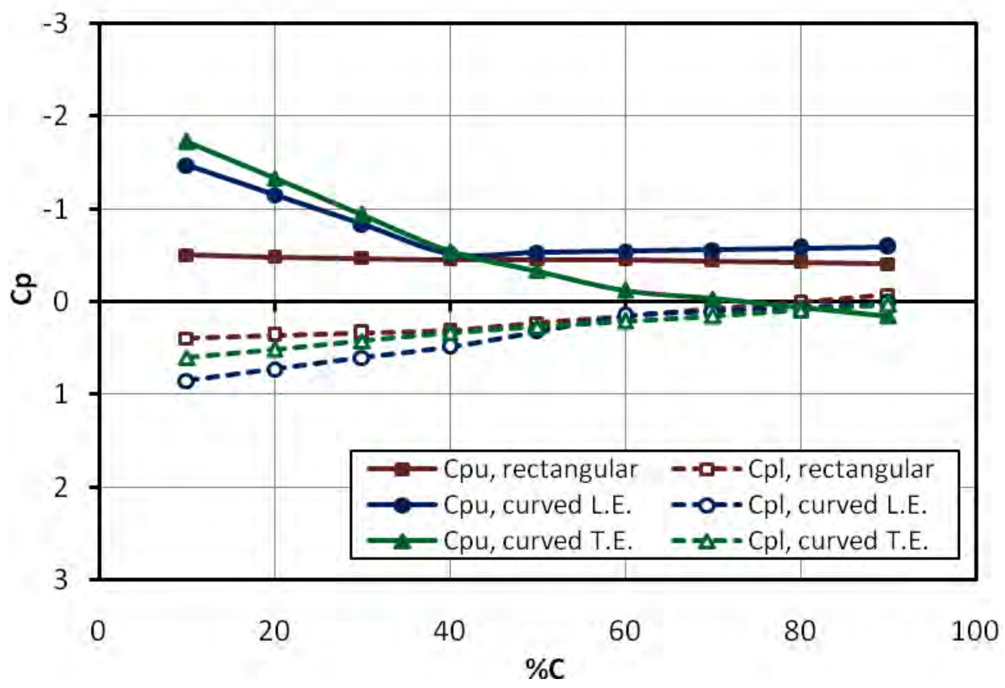

Figure 6.26: C_p Distribution of Segment-B at $\alpha = 20^{\circ}$

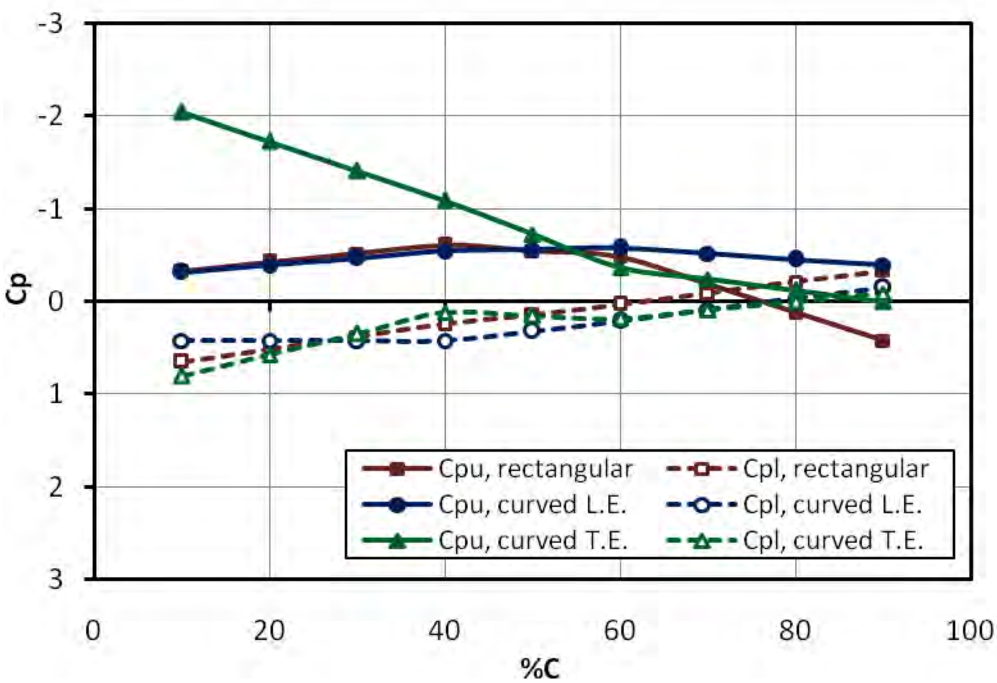

Figure 6.27: C_p Distribution of Segment-C at α = 20°

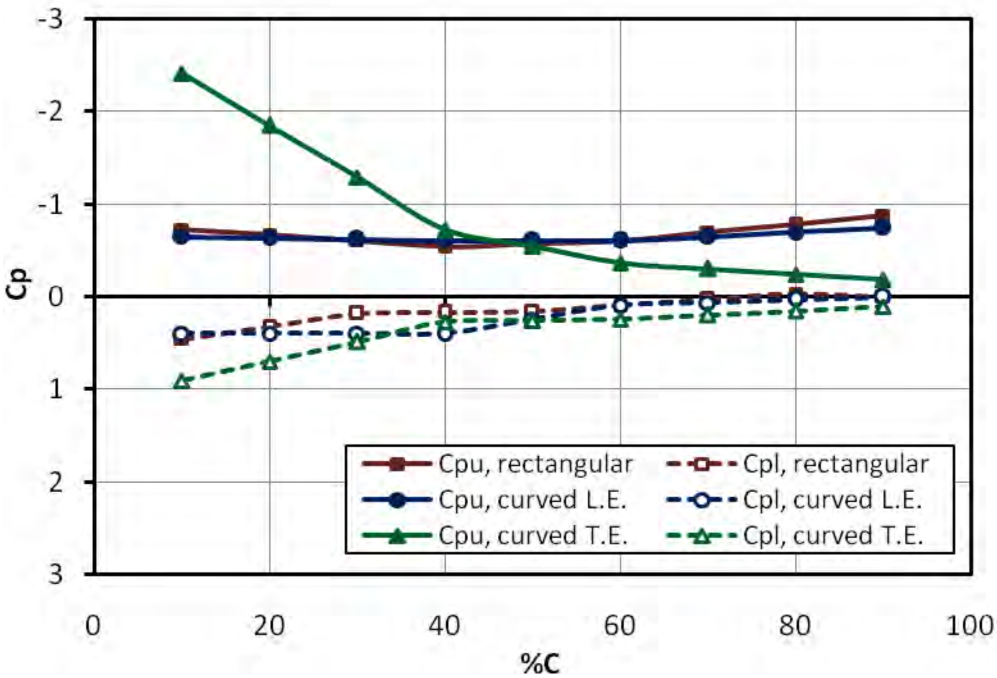

Figure 6.28: C_p Distribution of Segment-D at α = 20°

In comparison to the pressure difference of the surfaces of curved L.E. planform in segment-A and segment-B, the pressure difference of the surfaces of curved T.E. planform in segment-C and segment-D are higher. Another observation is made from Figure 6.27 and Figure 6.28 is that the upper surface pressure curve of rectangular planform and curved L.E. planform follow almost similar pattern in segment-C and segment-D.

6.2.8 Pressure distribution at 24° angle of attack

Figure 6.29, 6.30, 6.31 and 6.32 shows the surface pressure distribution along the chord at 24° angle of attack for four segments of all the three planforms respectively.

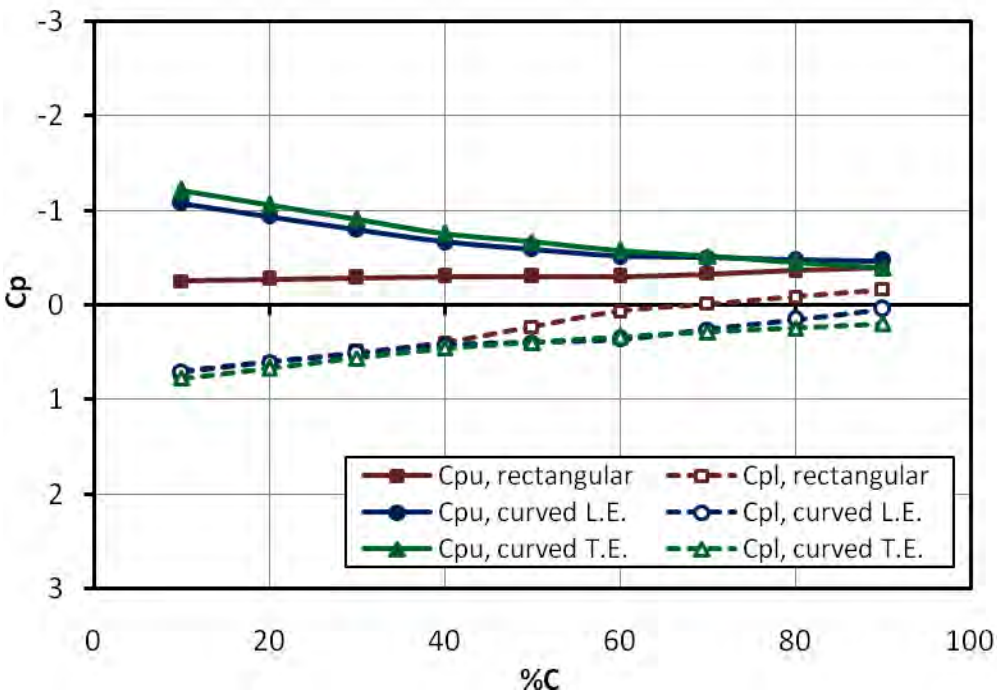

Figure 6.29: C_p Distribution of Segment-A at α = 24°

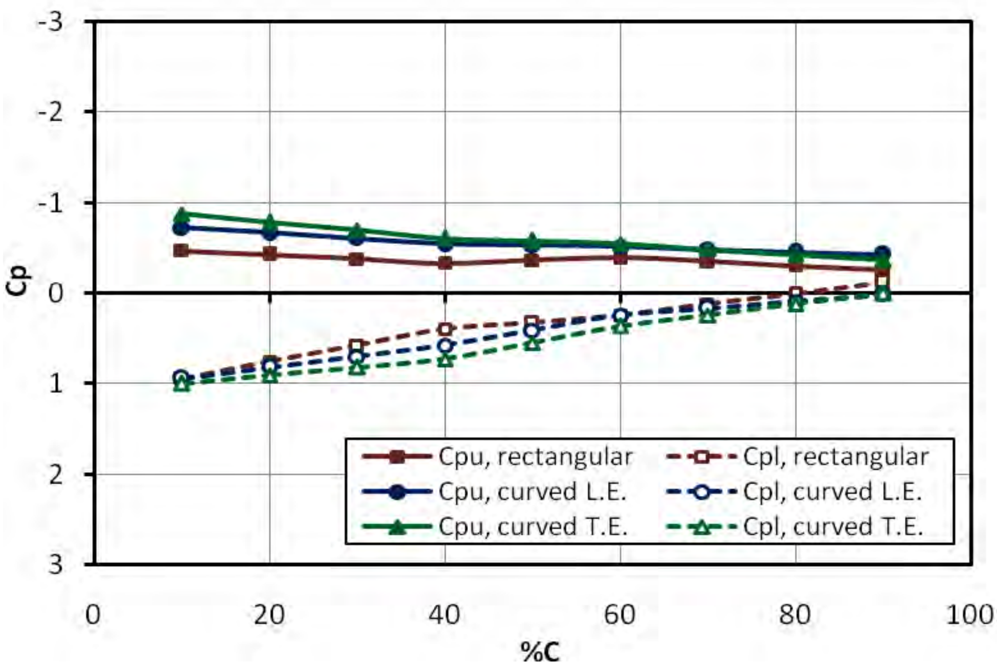

Figure 6.30: C_p Distribution of Segment-B at α = 24°

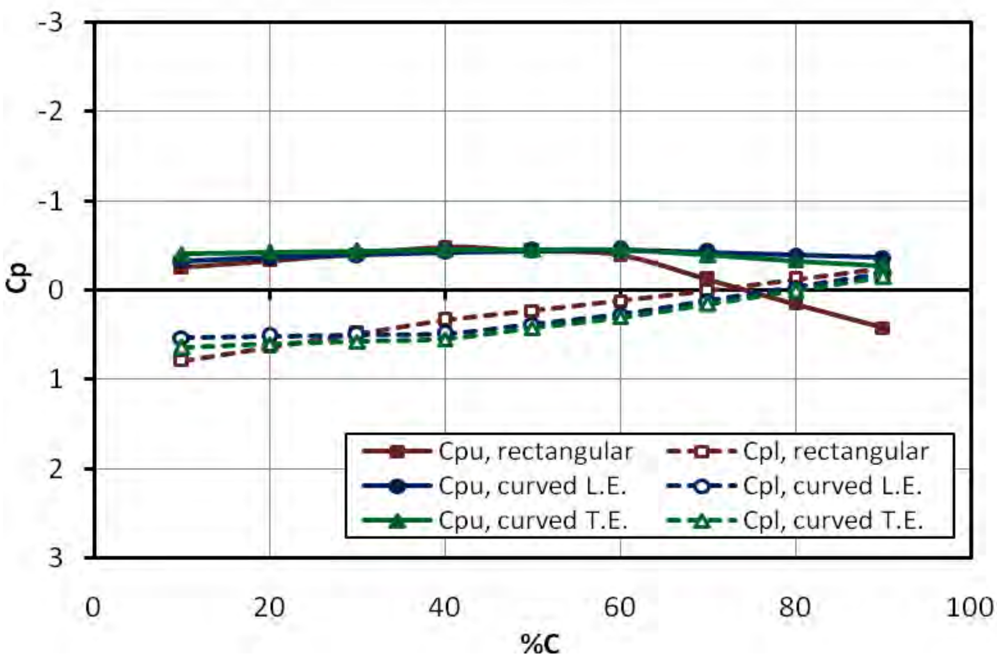

Figure 6.31: C_p Distribution of Segment-C at α = 24°

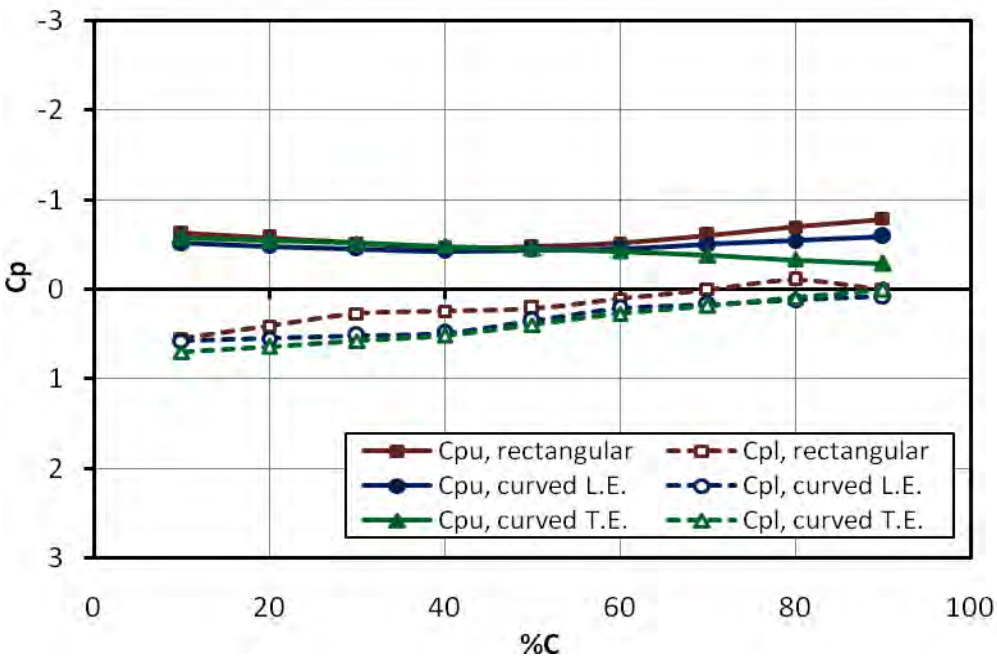

Figure 6.32: C_p Distribution of Segment-D at $\alpha = 24^\circ$

In a ll t he a bove f our f igures, i t i s obs erved t hat t he pr essure di fference between upper and lower surface of all the planforms are very less compared to those at previous angles of attack. But among three planforms, curved T.E. planform i s ha ving hi gher pr essure di fference between upp er and l ower surfaces at 24˚ angle of attack as observed in Figure 6.29-6.32.

6.3 Lift Characteristics

Variations of lift coefficient with angle of attack for three wing planforms are shown in Figure 6.33. It is observed that the lift coefficient curve rises from -4˚ angle of attack up to 16˚ angle of attack for all the planforms and then falls rapidly beyond 16˚ angle of attack. Thus, the c ritical angle of at tack of all t he t hree planforms remain around 16˚ beyond which the stall occurs. Lift coefficient curve for curved T.E. planforms is observed much higher than that of the curved L.E. planform and the r ectangular pl anform. The di fference b etween the v alues of lift coefficient of curved T.E. planform and other two planforms are observed highest at 16˚ angle of attack.

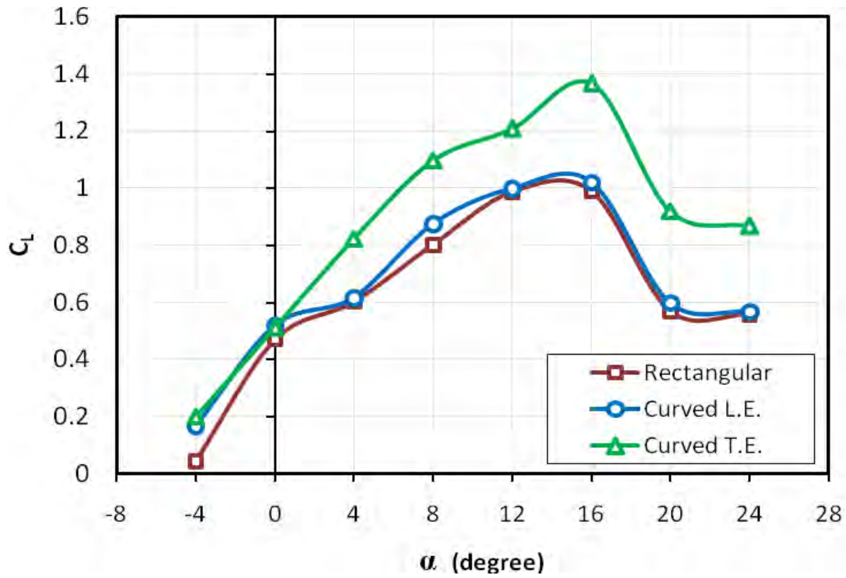

Figure 6.33: Variation of Lift Coefficient with Angle of Attack

6.4 Drag Characteristics

In Figure 6.34, the variation of drag coefficient for all the wing planforms are plotted against different angle of attack and it is observed that the values of drag coefficient for curved T.E. planform are much lower than that of the rectangular wing planform and curved L.E. planform. The significant reduction of drag of curved T. E. planform is observed from 8˚ to 24˚ angle of attack.

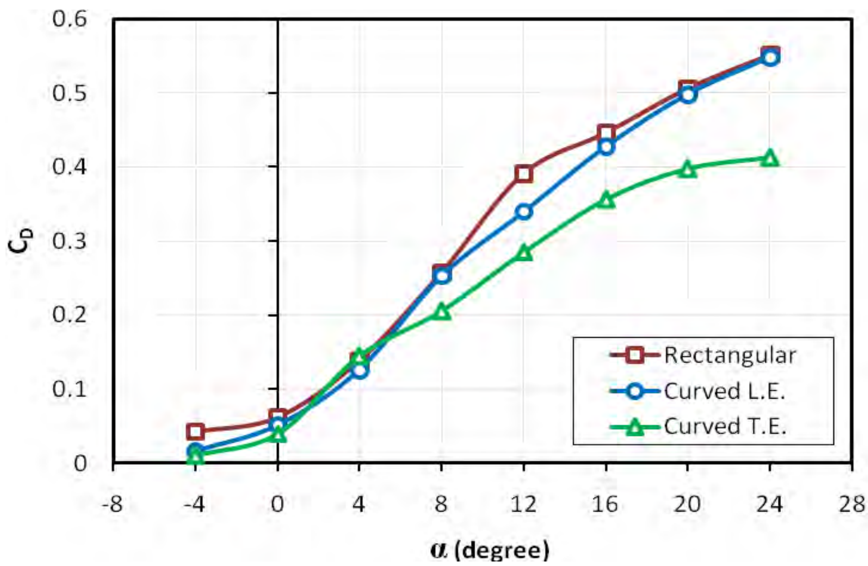

Figure 6.34: Variation of Drag Coefficient with Angle of Attack

6.5 Lift to Drag Ratio

The values of lift to drag ratio are plotted for various angle of attack in Figure 6.35. The figure shows that the lift to drag ratio of curved L.E. wing is higher than that of the rectangular wing. It is also observed from the graph that the lift to drag ratio of curved T .E. pl anform is hi gher t han t hat of t he c urved L.E. pl anform and t he rectangular planform for all angles of attack. For -4˚ angle of attack, lift to drag ratio of c urved T .E. wing pl anform i s obs erved s ignificantly higher t han other t wo planforms.

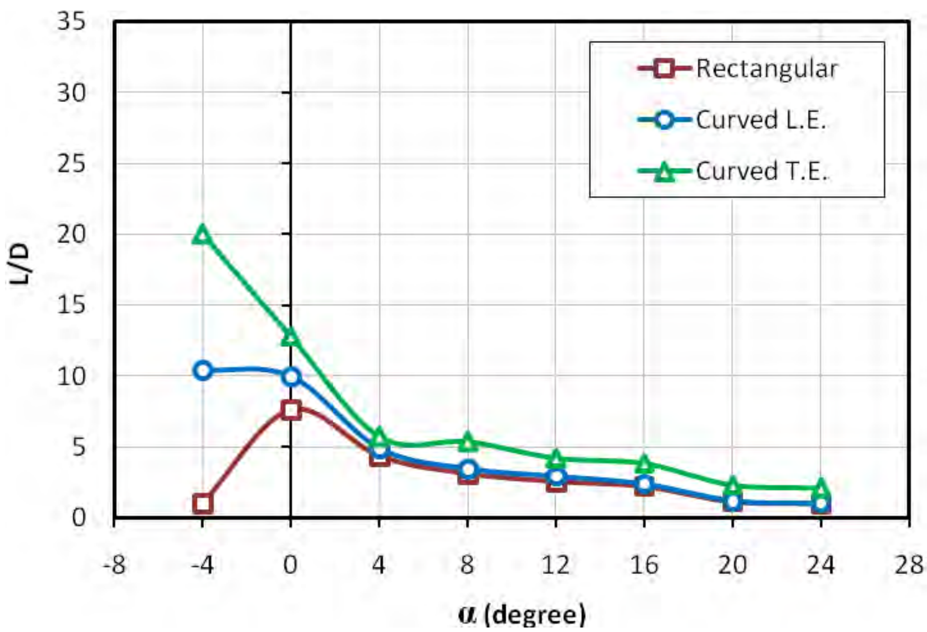

Figure 6.35: Variation of Lift to Drag Ratio with Angle of Attack

7. CONCLUSION AND RECOMMENDATIONS

7.1 Conclusion

In this research, curved boundary is incorporated at the leading edge and trailing edge of two separate wing planforms in such a way that the surface area from the middle of the wing towards the root increases and towards the tip the area decreases in the same rate. But the overall surface area of the wings remain same as of the rectangular planform. The overall outcome of the research may be summarized as follows:

a. From the analysis of surface pressure distribution, it is observed that the difference in upper and lower surface pressure of the curved-edge wing planforms near the root (in segment-A and segment-B) are higher than the pressure difference near the tip (in segment-C and segment-D). Thus, the curved-edge wing planforms can produce more lift due to increased surface area near the root of the wings.

b. It is also observed that near the tip (in segment-C and segment-D), the difference between upper and lower surface pressure of curved-edge planforms is comparatively higher than that of the rectangular planform. This phenomenon happened as tip loss of the curved-edge wing planforms is reduced due to reduction of chord length at the tip.

c. From the analysis of variation of lift coefficient with angle of attack, it is observed that the critical angle of attack for curved-edge planforms remain around 16˚ as of the rectangular planform. So, stalling occurs after 16˚ angle of attack for all three wing planforms.

d. The curved trailing edge planform exhibits the best lift characteristics among the three planforms and the curved leading edge planform exhibits better lift characteristics than the rectangular planform. Analyzing the drag coefficient versus angle of attack curves, it is found that the drag is lowest for the curved trailing edge planform among the three experimental wings. The curved leading edge planform also produces less drag than the rectangular planform. As a result, the lift to drag ratio is best for the curved trailing edge planform.

7.2 Recommendations for Future Work

The author would like to make the following recommendations for future work in this field:

a. Position and nature of the leading edge and trailing edge curve may be changed by varying the ratio of root chord to tip chord and wind tunnel test of those curved-edge planforms may be carried out to investigate aerodynamic characteristics.

b. The research may be conducted at higher wind tunnel speed to analyze the variation of aerodynamic characteristics of curved-edge planforms with the variation of air speed or Mach number.

c. Flaps may be incorporated at any suitable location at the leading edge and/trailing edge to analyze the aerodynamic characteristics of curved-edge wing planforms with and without flaps.

d. The coefficient of moment of the curved-edge wing planforms may be determined and compared with that of the rectangular planform to analyze the aerodynamic stability characteristics of the wings.

e. Aerofoil section other than NACA 4412 may be used for the curved-edge wing planforms.

f. Different aerofoils may be used at different segments of the same curved-edge planform to investigate its aerodynamic characteristics.

REFERRENCES

[1] Lynch, F.T., "Commercial Transports-Aerodynamic Design for Cruise Performance Efficiency," Chapter II in Transonic Aerodynamics, David Nixon, Ed., Progress in Astronautics and Aeronautics, Vol. 81, AIAA, New York, 1982, pp. 81-144.

[2] Hossain, A., Rahman, A., Iqbal, A.K.M.P., Ariffin, M., and Mazian, M., "Drag Analysis of an Aircraft Wing Model with and without Bird Feather like Winglet", International Journal of Aerospace and Mechanical Engineering, Vol. 6, No.1, 2012, pp.8-13.

[3] Dwivedi, Y.D., Prasad, M.S., and Dwivedi, S., "Experimental Aerodynamic Static Stability Analysis of Different Wing Planforms", International Journal of Advancements in Research & Technology, Vol. 2, No. 6, June 2013, pp.60-63.

[4] Mineck, R.E., and Vijgen, P.M.H.W., "Wind-Tunnel Investigation of Aerodynamic Efficiency of Three Planar Elliptical Wings with Curvature of Quarter-Chord Line", NASA Technical Paper 3359, October 1993, pp. 1-20.

[5] Recktenwald, B., "Aerodynamics of a Circular Planform Aircraft", American Institute of Aeronautics and Astronautics 022308, 2008, pp.1-7.

[6] Wakayama, S., "Subsonic Wing Planform Design Using Multidisciplinary Optimization", Journal of Aircraft, Vol. 32, No. 4, July-August 1995, pp. 746-753.

[7] Paulo, F.R., Bento, S.M., Roberto, M.G., and Pedro, P., "Wing Planform Optimization of a Transport Aircraft", 22^{nd} Applied Aerodynamics Conference, 16-19 August 2004, Rhode Island, U.S.A., pp.1-14.

[8] Mahmud, M.S., "Analysis of Effectiveness of an Airfoil with Bi-camber Surface", International Journal of Engineering and Technology, Vol. 3, No. 5, May 2013, pp.569-577.

[9] Kandwal, S., and Singh, S., "Computational Fluid Dynamics Study of Fluid Flow and Aerodynamic Forces on an Airfoil", International Journal of Engineering and Technology, Vol. 1, No. 7, September 2012, pp.1-8.

[10] Robert, M.P., "The Variation with Reynolds Number of Pressure Distribution over an Airfoil Section", NACA Report No. 613, pp.65-84.

[11] Sharma, A., "Evaluation of Flow Behavior around an Airfoil Body", M. Engg thesis, Department of Mechanical Engineering, Thapar University, Patiala-147004, India, July 2012, pp.1-60.

[12] Ismail, L.W., "Investigation of Load and Pressure Distribution on Wing with Wake Rollup for Low Speed Aircraft", Al-Khwarizmi Engineering Journal, Vol. 4, No. 2, 2008, pp. 59-68.

[13] Wells, A. J., "Experimental Investigation of an Airfoil with Co-Flow Jet Flow Control", M Sc Thesis, University of Florida, 2005.

[14] Demasi, L., "Aerodynamic Analysis of Non-conventional Wing Configurations for Aero-elastic Applications", Ph D Dissertation, Politecnico di Torino, April 2004.

[15] McArthur, J., "Aerodynamics of Wings at Low Reynolds Numbers: Boundary Layer Separation and Reattachment", Ph D Dissertation, University of Southern California, December 2008.

[16] Alam, G. M. J., "Interference Effect and Flow Pattern of Four Biplane Configurations using NACA 0024 Profile", Proceedings of the International Conference on Mechanical Engineering 2011, 18-20 December 2011, Dhaka, Bangladesh.

[17] Hassan, I. A., Darwish, A. S., and Jaffal, H. M., "Theoretical and Experimental Study of a Forward Swept Wing", Anbar Journal for Engineering Sciences, Vol.3, No.2, 2010, pp. 15-30.

[18] Ahmed, M. R., "Aerodynamics of a Cambered Airfoil in Ground Effect", International Journal of Fluid Mechanics Research, Vol. 32, No. 2, 2005, pp. 157-183.

[19] Walter, D. J., "Study of Aerofoils at High Angle of Attack, in Ground Effect", M Sc thesis, School of Aerospace, Mechanical & Manufacturing Engineering, RMIT University, Australia, September 2007.

[20] Al-Kayiem, H. H. and Kartigesh, A.K., "An Investigation on the Aerodynamic Characteristics of 2-D Airfiol in Ground Collision", Journal of Engineering Science and Technology, Vol. 6, No. 3, 2011, pp. 369 – 381.

[21] Janiszewska, J. M., "Three Dimensional Aerodynamics of a Simple Wing in Oscillation Including Effects of Vortex Generators", Ph D Dissertation, Graduate School of Ohio State University, 2004.

[22] Arora, P. R., Hossain, A., Edi, P., Jaafar, A. A., Younis, T. S., and Saleem, M., "Drag Reduction in Aircraft Model using Elliptical Winglet", Journal of The Institution of Engineers, Malaysia, Vol. 66, No. 4, December 2005, pp. 1-8.

[23] Mashud, M., and Hossain, M. F., "Experimental Study of Flow Separation Control of an Airfoil by Suction and Injection", Proceedings of the 13th Asian Congress of Fluid Mechanics, 17-21 December 2010, Dhaka, Bangladesh, pp. 166-169.

[24] Anderson, J.D., “Fundamentals of Aerodynamics”, McGraw-Hill Series in Aeronautical and Aerospace Engineering, 3rd Edition, pp. 15-22.

[25] Kermode, A. C., “Flight without Formula”, Pitman, 8th edition 1970.

[26] Clancy, L. J., “Aerodynamics”, John Wiley, New York, 1975.

[27] Laurence, K. L. Jr. and Poteat, M. I., “Aerodynamic Characteristics of several NACA airfoil sections at seven Reynolds number from $0.7x10^6$ to $9.0x10^6$”, Langley Memorial Aeronautical Laboratory, 1948.

[28] Abbott, I. H. and Doenhoff, A. E. V., “Theory of Wing Sections including a Summary of Aerofoil Data”, Dover Publications, Inc, New York, 1959.

[29] Eppler, R., “Airfoil Design and Data”, Springer-Verlag, Berlin, 1990.

[30] Abbott, I. H., Von Doenhoff, A. E. V., and Stivers, L. S., “Summary of Aerofoil Data”, NACA Report No. 824, 1945.

[31] Sadraey, M. H., “ Aircraft Design: A Systems Engineering Approach”, Wiley publications, October 2012, pp. 170-178.

[32] Ramesh, P., “Numerical and experimental investigation of the effect of geometry modification on the aerodynamic characteristics of a NACA 64(2)-415 wing”, M Sc Thesis, Royal Institute of Technology, Stockholm, Sweden, 2013.

[33] White, F.M., “Fluid Mechanics”, McGraw-Hill Series in Mechanical Engineering, 4th Edition, 1999, pp. 526.

[34] Devenport, W.J. and Schetz, J. A., “The Investigation of an Inboard-Winglet Application to a Roadable Aircraft”, M Sc in Aerospace Engineering Thesis, Virginia Polytechnic Institute and State University, May 2002, pp. 24-26.

[35] Mainuddin, M., and Ali, M.A.T., “Experimental Investigation of Lift to Drag Ratio between Volumetric Equivalent Fuselages”, Proceedings of the 4th BSME-ASME International Conference on Thermal Engineering, 27-29 December 2008, Dhaka, Bangladesh, pp.383-390.

[36] Cimbala, J. M., “Experimental Uncertainty Analysis”, Online Edition, 30 January 2013, pp. 1-4.

APPENDIX-I

Table 1: Calculated Values of Pressure Coefficients at -4° Angle of Attack

	%C	Cpu, rect	Cpl, rect	Cpu, curved L.E.	Cpl, curved L.E.	Cpu, curved T.E.	Cpl, curved T.E.
Segment-A	10	-0.545454545	-1.53030303	0.090909091	-0.772727273	-0.121212121	-0.227272727
	20	-0.515151515	-1.121212121	-0.060606061	-0.545454545	-0.242424242	-0.151515152
	30	-0.484848485	-0.712121212	-0.212121212	-0.318181818	-0.363636364	-0.075757576
	40	-0.454545455	-0.303030303	-0.363636364	-0.090909091	-0.484848485	0
	50	-0.378787879	-0.181818182	-0.318181818	-0.03030303	-0.409090909	0.015151515
	60	-0.303030303	-0.060606061	-0.272727273	0.03030303	-0.333333333	0.03030303
	70	-0.318181818	-0.03030303	-0.227272727	0.045454545	-0.348484848	0.045454545
	80	-0.333333333	0	-0.181818182	0.060606061	-0.363636364	0.060606061
	90	-0.348484848	0.03030303	-0.136363636	0.075757576	-0.378787879	0.075757576
	%C	Cpu, rect	Cpl, rect	Cpu, curved L.E.	Cpl, curved L.E.	Cpu, curved T.E.	Cpl, curved T.E.
Segment-B	10	-0.575757576	-1.212121212	-0.181818182	-0.772727273	-0.393939394	-0.272727273
	20	-0.545454545	-0.909090909	-0.272727273	-0.575757576	-0.393939394	-0.181818182
	30	-0.515151515	-0.606060606	-0.363636364	-0.378787879	-0.393939394	-0.090909091
	40	-0.484848485	-0.303030303	-0.454545455	-0.181818182	-0.393939394	0
	50	-0.181818182	-0.151515152	-0.515151515	-0.106060606	-0.363636364	0.03030303
	60	0.121212121	0	-0.575757576	-0.03030303	-0.333333333	0.060606061
	70	-0.151515152	0.015151515	-0.424242424	0.015151515	-0.151515152	0.075757576
	80	-0.424242424	0.03030303	-0.272727273	0.060606061	0.03030303	0.090909091
	90	-0.696969697	0.045454545	-0.121212121	0.106060606	0.212121212	0.106060606
	%C	Cpu, rect	Cpl, rect	Cpu, curved L.E.	Cpl, curved L.E.	Cpu, curved T.E.	Cpl, curved T.E.
Segment-C	10	-0.5	-1.272727273	-0.893939394	-0.318181818	-0.424242424	-0.681818182
	20	-0.454545455	-0.939393939	-0.727272727	-0.242424242	-0.424242424	-0.424242424
	30	-0.409090909	-0.606060606	-0.560606061	-0.166666667	-0.424242424	-0.166666667
	40	-0.363636364	-0.272727273	-0.393939394	-0.090909091	-0.424242424	0.090909091
	50	-0.409090909	-0.227272727	-0.272727273	-0.075757576	-0.424242424	-0.015151515
	60	-0.454545455	-0.181818182	-0.151515152	-0.060606061	-0.424242424	-0.121212121
	70	-0.181818182	-0.090909091	-0.166666667	0	-0.348484848	-0.121212121
	80	0.090909091	0	-0.181818182	0.060606061	-0.272727273	-0.121212121
	90	0	0.090909091	-0.196969697	0.121212121	-0.196969697	-0.121212121
	%C	Cpu, rect	Cpl, rect	Cpu, curved L.E.	Cpl, curved L.E.	Cpu, curved T.E.	Cpl, curved T.E.
Segment-D	10	-0.651515152	-0.803030303	-0.590909091	-0.515151515	-0.878787879	0
	20	-0.606060606	-0.575757576	-0.515151515	-0.393939394	-0.696969697	-0.03030303
	30	-0.560606061	-0.348484848	-0.439393939	-0.272727273	-0.515151515	-0.060606061
	40	-0.515151515	-0.121212121	-0.363636364	-0.151515152	-0.333333333	-0.090909091
	50	-0.454545455	-0.060606061	-0.363636364	-0.060606061	-0.333333333	-0.045454545
	60	-0.393939394	0	-0.363636364	0.03030303	-0.333333333	0
	70	-0.454545455	0	-0.348484848	0.060606061	-0.333333333	0.045454545
	80	-0.545454545	0	-0.333333333	0.090909091	-0.333333333	0.090909091
	90	-0.636363636	0	-0.318181818	0.121212121	-0.333333333	0.136363636

Table 2: Calculated Values of Pressure Coefficients at 0˚ Angle of Attack

	%C	Cpu, rect	Cpl, rect	Cpu, curved L.E.	Cpl, curved L.E.	Cpu, curved T.E.	Cpl, curved T.E.
Segment-A	10	-1.0151515	-0.33333	-0.121212121	-0.424242424	-0.121212121	-0.227272727
	20	-0.9090909	-0.24242	-0.272727273	-0.303030303	-0.242424242	-0.151515152
	30	-0.8030303	-0.15152	-0.424242424	-0.181818182	-0.363636364	-0.075757576
	40	-0.6969697	-0.06061	-0.575757576	-0.060606061	-0.484848485	0
	50	-0.5454545	-0.04545	-0.454545455	-0.015151515	-0.409090909	0.015151515
	60	-0.3939394	-0.0303	-0.333333333	0.03030303	-0.333333333	0.03030303
	70	-0.3484848	-0.01515	-0.303030303	0.060606061	-0.348484848	0.045454545
	80	-0.3030303	0	-0.272727273	0.090909091	-0.363636364	0.060606061
	90	-0.2575758	0.015152	-0.242424242	0.121212121	-0.378787879	0.075757576
	%C	Cpu, rect	Cpl, rect	Cpu, curved L.E.	Cpl, curved L.E.	Cpu, curved T.E.	Cpl, curved T.E.
Segment-B	10	-0.969697	0.045455	-0.590909091	-0.272727273	-0.393939394	-0.272727273
	20	-0.8484848	0	-0.606060606	-0.212121212	-0.393939394	-0.181818182
	30	-0.7272727	-0.04545	-0.621212121	-0.151515152	-0.393939394	-0.090909091
	40	-0.6060606	-0.09091	-0.636363636	-0.090909091	-0.393939394	0
	50	-0.2272727	-0.0303	-0.666666667	-0.060606061	-0.363636364	0.03030303
	60	0.15151515	0.030303	-0.696969697	-0.03030303	-0.333333333	0.060606061
	70	-0.1060606	0.015152	-0.484848485	0.015151515	-0.151515152	0.075757576
	80	-0.3636364	0	-0.272727273	0.060606061	0.03030303	0.090909091
	90	-0.6212121	-0.01515	-0.060606061	0.106060606	0.212121212	0.106060606
	%C	Cpu, rect	Cpl, rect	Cpu, curved L.E.	Cpl, curved L.E.	Cpu, curved T.E.	Cpl, curved T.E.
Segment-C	10	-0.9090909	-0.16667	-1.333333333	-0.212121212	-0.424242424	-0.681818182
	20	-0.7575758	-0.18182	-1.060606061	-0.121212121	-0.424242424	-0.424242424
	30	-0.6060606	-0.19697	-0.787878788	-0.03030303	-0.424242424	-0.166666667
	40	-0.4545455	-0.21212	-0.515151515	0.060606061	-0.424242424	0.090909091
	50	-0.5	-0.18182	-0.363636364	0	-0.424242424	-0.015151515
	60	-0.5454545	-0.15152	-0.212121212	-0.060606061	-0.424242424	-0.121212121
	70	-0.2272727	-0.06061	-0.181818182	-0.015151515	-0.348484848	-0.121212121
	80	0.09090909	0.030303	-0.151515152	0.03030303	-0.272727273	-0.121212121
	90	-0.0454545	0	-0.121212121	0.075757576	-0.196969697	-0.121212121
	%C	Cpu, rect	Cpl, rect	Cpu, curved L.E.	Cpl, curved L.E.	Cpu, curved T.E.	Cpl, curved T.E.
Segment-D	10	-0.9848485	-0.34848	-0.984848485	-0.348484848	-0.878787879	0
	20	-0.8787879	-0.27273	-0.818181818	-0.242424242	-0.696969697	-0.03030303
	30	-0.7727273	-0.19697	-0.681818182	-0.136363636	-0.515151515	-0.060606061
	40	-0.6666667	-0.12121	-0.545454545	-0.03030303	-0.333333333	-0.090909091
	50	-0.5606061	-0.06061	-0.484848485	-0.03030303	-0.333333333	-0.045454545
	60	-0.4545455	0	-0.424242424	-0.03030303	-0.333333333	0
	70	-0.469697	0	-0.393939394	0.045454545	-0.333333333	0.045454545
	80	-0.4848485	0	-0.363636364	0.121212121	-0.333333333	0.090909091
	90	-0.5	0	-0.333333333	0.196969697	-0.333333333	0.136363636

Table 3: Calculated Values of Pressure Coefficients at 4° Angle of Attack

	%C	Cpu, rect	Cpl, rect	Cpu, curved L.E.	Cpl, curved L.E.	Cpu, curved T.E.	Cpl, curved T.E.
Segment-A	10	-1.439393939	-0.106060606	-0.318181818	-0.136363636	-0.409090909	-0.181818182
	20	-1.212121212	-0.090909091	-0.424242424	-0.090909091	-0.484848485	-0.121212121
	30	-0.984848485	-0.075757576	-0.53030303	-0.045454545	-0.560606061	-0.060606061
	40	-0.757575758	-0.060606061	-0.636363636	0	-0.636363636	0
	50	-0.560606061	-0.075757576	-0.5	0.03030303	-0.53030303	0.03030303
	60	-0.363636364	-0.090909091	-0.363636364	0.060606061	-0.424242424	0.060606061
	70	-0.303030303	-0.045454545	-0.272727273	0.075757576	-0.409090909	0
	80	-0.242424242	0	-0.181818182	0.090909091	-0.393939394	0.060606061
	90	-0.181818182	0.045454545	-0.090909091	0.106060606	-0.378787879	0.121212121
	%C	Cpu, rect	Cpl, rect	Cpu, curved L.E.	Cpl, curved L.E.	Cpu, curved T.E.	Cpl, curved T.E.
Segment-B	10	-1.454545455	0.121212121	-0.909090909	0.045454545	-1.015151515	0.106060606
	20	-1.212121212	0.060606061	-0.878787879	0.03030303	-0.96969697	0.090909091
	30	-0.96969697	0	-0.848484848	0.015151515	-0.924242424	0.075757576
	40	-0.727272727	-0.060606061	-0.818181818	0	-0.878787879	0.060606061
	50	-0.303030303	-0.03030303	-0.787878788	0	-0.848484848	0.045454545
	60	0.121212121	0	-0.757575758	0	-0.818181818	0.03030303
	70	-0.075757576	0	-0.515151515	0.045454545	-0.439393939	0.03030303
	80	-0.272727273	0	-0.272727273	0.090909091	-0.363636364	0.03030303
	90	-0.46969697	0	-0.03030303	0.136363636	-0.287878788	0.03030303
	%C	Cpu, rect	Cpl, rect	Cpu, curved L.E.	Cpl, curved L.E.	Cpu, curved T.E.	Cpl, curved T.E.
Segment-C	10	-1.212121212	-0.075757576	-1.803030303	-0.106060606	-2.121212121	0.060606061
	20	-1	-0.090909091	-1.393939394	0	-1.757575758	0.151515152
	30	-0.787878788	-0.106060606	-0.984848485	0.106060606	-1.333333333	0.242424242
	40	-0.575757576	-0.121212121	-0.575757576	0.212121212	-0.909090909	0.333333333
	50	-0.560606061	-0.121212121	-0.393939394	0.106060606	-0.757575758	0.272727273
	60	-0.545454545	-0.121212121	-0.212121212	0	-0.606060606	0.212121212
	70	-0.196969697	-0.075757576	-0.166666667	0.03030303	-0.454545455	0.196969697
	80	0.151515152	-0.03030303	-0.121212121	0.060606061	-0.303030303	0.181818182
	90	0.106060606	0.015151515	-0.075757576	0.090909091	-0.151515152	0.166666667
	%C	Cpu, rect	Cpl, rect	Cpu, curved L.E.	Cpl, curved L.E.	Cpu, curved T.E.	Cpl, curved T.E.
Segment-D	10	-1.181818182	-0.121212121	-1.393939394	-0.121212121	-1.636363636	0.075757576
	20	-1.060606061	-0.121212121	-1.151515152	-0.060606061	-1.363636364	0.090909091
	30	-0.939393939	-0.121212121	-0.909090909	0	-1.090909091	0.106060606
	40	-0.818181818	-0.121212121	-0.666666667	0.060606061	-0.818181818	0.121212121
	50	-0.621212121	-0.060606061	-0.545454545	0.03030303	-0.696969697	0.106060606
	60	-0.424242424	0	-0.424242424	0	-0.575757576	0.090909091
	70	-0.439393939	0	-0.378787879	0.075757576	-0.53030303	0.121212121
	80	-0.454545455	0	-0.333333333	0.151515152	-0.424242424	0.151515152
	90	-0.46969697	0	-0.287878788	0.227272727	-0.318181818	0.181818182

Table 4: Calculated Values of Pressure Coefficients at 8° Angle of Attack

	%C	Cpu, rect	Cpl, rect	Cpu, curved L.E.	Cpl, curved L.E.	Cpu, curved T.E.	Cpl, curved T.E.
Segment-A	10	-2.106060606	0.196969697	-0.787878788	0.121212121	-0.939393939	0.303030303
	20	-1.696969697	0.151515152	-0.787878788	0.121212121	-0.878787879	0.272727273
	30	-1.287878788	0.106060606	-0.787878788	0.121212121	-0.818181818	0.242424242
	40	-0.878787879	0.060606061	-0.787878788	0.121212121	-0.757575758	0.212121212
	50	-0.651515152	0	-0.606060606	0.136363636	-0.606060606	0.181818182
	60	-0.424242424	-0.060606061	-0.424242424	0.151515152	-0.454545455	0.151515152
	70	-0.318181818	-0.03030303	-0.287878788	0.136363636	-0.333333333	0.151515152
	80	-0.212121212	0	-0.151515152	0.121212121	-0.212121212	0.151515152
	90	-0.106060606	0.03030303	-0.015151515	0.106060606	-0.090909091	0.151515152
	%C	Cpu, rect	Cpl, rect	Cpu, curved L.E.	Cpl, curved L.E.	Cpu, curved T.E.	Cpl, curved T.E.
Segment-B	10	-1.818181818	0.303030303	-1.46969697	0.303030303	-1.651515152	0.424242424
	20	-1.515151515	0.212121212	-1.333333333	0.272727273	-1.484848485	0.393939394
	30	-1.212121212	0.121212121	-1.196969697	0.242424242	-1.318181818	0.363636364
	40	-0.909090909	0.03030303	-1.060606061	0.212121212	-1.151515152	0.333333333
	50	-0.378787879	0.060606061	-0.893939394	0.151515152	-1	0.272727273
	60	0.151515152	0.090909091	-0.727272727	0.090909091	-0.848484848	0.212121212
	70	0	0.045454545	-0.5	0.121212121	-0.545454545	0.196969697
	80	-0.151515152	0	-0.272727273	0.151515152	-0.242424242	0.181818182
	90	-0.303030303	-0.045454545	-0.045454545	0.181818182	0.060606061	0.166666667
	%C	Cpu, rect	Cpl, rect	Cpu, curved L.E.	Cpl, curved L.E.	Cpu, curved T.E.	Cpl, curved T.E.
Segment-C	10	-1.666666667	0.212121212	-2.333333333	0.166666667	-2.727272727	0.424242424
	20	-1.333333333	0.151515152	-1.787878788	0.212121212	-2.121212121	0.393939394
	30	-1	0.090909091	-1.242424242	0.257575758	-1.515151515	0.363636364
	40	-0.666666667	0.03030303	-0.696969697	0.303030303	-0.909090909	0.333333333
	50	-0.606060606	0.015151515	-0.46969697	0.151515152	-0.681818182	0.242424242
	60	-0.545454545	-0.060606061	-0.242424242	0	-0.454545455	0.151515152
	70	-0.196969697	-0.075757576	-0.136363636	0.03030303	-0.348484848	0.136363636
	80	0.151515152	-0.090909091	-0.03030303	0.060606061	-0.242424242	0.121212121
	90	0.5	-0.106060606	0.075757576	0.090909091	-0.136363636	0.106060606
	%C	Cpu, rect	Cpl, rect	Cpu, curved L.E.	Cpl, curved L.E.	Cpu, curved T.E.	Cpl, curved T.E.
Segment-D	10	-1.621212121	0.090909091	-1.848484848	0.03030303	-2.075757576	0.212121212
	20	-1.363636364	0.060606061	-1.515151515	0.090909091	-1.727272727	0.242424242
	30	-1.106060606	0.03030303	-1.181818182	0.151515152	-1.378787879	0.272727273
	40	-0.848484848	0	-0.848484848	0.212121212	-1.03030303	0.303030303
	50	-0.666666667	0.03030303	-0.681818182	0.136363636	-0.818181818	0.196969697
	60	-0.484848485	0.060606061	-0.515151515	0.060606061	-0.606060606	0.090909091
	70	-0.46969697	0.045454545	-0.409090909	0.121212121	-0.5	0.151515152
	80	-0.454545455	0.03030303	-0.303030303	0.181818182	-0.393939394	0.212121212
	90	-0.439393939	0.015151515	-0.196969697	0.242424242	-0.287878788	0.272727273

Table 5: Calculated Values of Pressure Coefficients at 12° Angle of Attack

	%C	Cpu, rect	Cpl,rect	Cpu, curved L.E.	Cpl, curved L.E.	Cpu, curved T.E.	Cpl, curved T.E.
Segment-A	10	-2.42424	0.409091	-0.560606061	0.303030303	-0.924242424	0.196969697
	20	-1.90909	0.333333	-0.666666667	0.272727273	-0.878787879	0.181818182
	30	-1.39394	0.257576	-0.772727273	0.242424242	-0.833333333	0.166666667
	40	-0.87879	0.181818	-0.878787879	0.212121212	-0.787878788	0.151515152
	50	-0.62121	0.090909	-0.606060606	0.212121212	-0.560606061	0.136363636
	60	-0.36364	0	-0.333333333	0.212121212	-0.333333333	0.121212121
	70	-0.25758	0.015152	-0.196969697	0.181818182	-0.257575758	0.106060606
	80	-0.15152	0.030303	-0.060606061	0.151515152	-0.181818182	0.090909091
	90	-0.04545	0.045455	0.075757576	0.121212121	-0.106060606	0.075757576
	%C	Cpu, rect	Cpl,rect	Cpu, curved L.E.	Cpl, curved L.E.	Cpu, curved T.E.	Cpl, curved T.E.
Segment-B	10	-2.27273	0.621212	-1.848484848	0.590909091	-1.424242424	0.257575758
	20	-1.81818	0.484848	-1.575757576	0.484848485	-1.151515152	0.242424242
	30	-1.36364	0.348485	-1.303030303	0.409090909	-0.878787879	0.227272727
	40	-0.90909	0.212121	-1.03030303	0.333333333	-0.606060606	0.212121212
	50	-0.78788	0.181818	-0.848484848	0.242424242	-0.46969697	0.196969697
	60	-0.66667	0.151515	-0.666666667	0.151515152	-0.333333333	0.181818182
	70	-0.33333	0.106061	-0.424242424	0.166666667	-0.136363636	0.166666667
	80	0	0.060606	-0.181818182	0.181818182	0.060606061	0.151515152
	90	0.333333	0.015152	0.060606061	0.196969697	0.257575758	0.136363636
	%C	Cpu, rect	Cpl,rect	Cpu, curved L.E.	Cpl, curved L.E.	Cpu, curved T.E.	Cpl, curved T.E.
Segment-C	10	-1.90909	0.454545	-2.272727273	0.303030303	-1.545454545	0.272727273
	20	-1.51515	0.363636	-1.727272727	0.333333333	-1.393939394	0.212121212
	30	-1.12121	0.272727	-1.181818182	0.363636364	-1.242424242	0.151515152
	40	-0.72727	0.181818	-0.636363636	0.393939394	-1.090909091	0.090909091
	50	-0.45455	0.121212	-0.409090909	0.196969697	-0.818181818	0.075757576
	60	-0.48485	0.060606	-0.181818182	0	-0.545454545	0.060606061
	70	-0.18182	0.015152	-0.090909091	0.015151515	-0.409090909	0.03030303
	80	0.121212	-0.0303	0	0.03030303	-0.272727273	0
	90	0.424242	-0.07576	0.090909091	0.045454545	-0.136363636	-0.03030303
	%C	Cpu, rect	Cpl,rect	Cpu, curved L.E.	Cpl, curved L.E.	Cpu, curved T.E.	Cpl, curved T.E.
Segment-D	10	-2	0.409091	-2.196969697	0.257575758	-1.909090909	0.666666667
	20	-1.63636	0.30303	-1.727272727	0.272727273	-1.484848485	0.484848485
	30	-1.27273	0.19697	-1.257575758	0.287878788	-1.060606061	0.303030303
	40	-0.90909	0.090909	-0.787878788	0.303030303	-0.636363636	0.121212121
	50	-0.68182	0.121212	-0.606060606	0.212121212	-0.515151515	0.136363636
	60	-0.45455	0.151515	-0.424242424	0.121212121	-0.393939394	0.151515152
	70	-0.42424	0.121212	-0.333333333	0.136363636	-0.333333333	0.121212121
	80	-0.39394	0.090909	-0.242424242	0.151515152	-0.272727273	0.090909091
	90	-0.36364	0.060606	-0.151515152	0.166666667	-0.212121212	0.060606061

Table 6: Calculated Values of Pressure Coefficients at 16° Angle of Attack

	%C	Cpu, rect	Cpl, rect	Cpu, curved L.E.	Cpl, curved L.E.	Cpu, curved T.E.	Cpl, curved T.E.
Segment-A	10	-2.651515152	0.575757576	-1.606060606	0.439393939	-2.181818182	0.590909091
	20	-1.939393939	0.484848485	-1.333333333	0.393939394	-1.818181818	0.545454545
	30	-1.227272727	0.393939394	-1.060606061	0.348484848	-1.454545455	0.5
	40	-0.515151515	0.303030303	-0.787878788	0.303030303	-1.090909091	0.454545455
	50	-0.363636364	0.166666667	-0.545454545	0.287878788	-0.818181818	0.409090909
	60	-0.212121212	0.03030303	-0.303030303	0.272727273	-0.545454545	0.363636364
	70	-0.272727273	-0.03030303	-0.227272727	0.227272727	-0.424242424	0.303030303
	80	-0.333333333	-0.090909091	-0.151515152	0.181818182	-0.303030303	0.242424242
	90	-0.393939394	-0.151515152	-0.075757576	0.136363636	-0.181818182	0.181818182
	%C	Cpu, rect	Cpl, rect	Cpu, curved L.E.	Cpl, curved L.E.	Cpu, curved T.E.	Cpl, curved T.E.
Segment-B	10	-1.757575758	0.848484848	-2.227272727	0.742424242	-2.575757576	0.878787879
	20	-1.272727273	0.666666667	-1.818181818	0.636363636	-2.121212121	0.787878788
	30	-0.787878788	0.484848485	-1.409090909	0.53030303	-1.666666667	0.696969697
	40	-0.303030303	0.303030303	-1	0.424242424	-1.212121212	0.606060606
	50	-0.348484848	0.242424242	-0.772727273	0.303030303	-0.984848485	0.424242424
	60	-0.393939394	0.181818182	-0.545454545	0.181818182	-0.757575758	0.242424242
	70	-0.363636364	0.106060606	-0.378787879	0.151515152	-0.545454545	0.196969697
	80	-0.333333333	0.03030303	-0.212121212	0.121212121	-0.333333333	0.151515152
	90	-0.303030303	-0.045454545	-0.045454545	0.090909091	-0.121212121	0.106060606
	%C	Cpu, rect	Cpl, rect	Cpu, curved L.E.	Cpl, curved L.E.	Cpu, curved T.E.	Cpl, curved T.E.
Segment-C	10	-1.803030303	0.666666667	-1.318181818	0.409090909	-1.893939394	0.727272727
	20	-1.424242424	0.545454545	-1	0.424242424	-1.515151515	0.666666667
	30	-1.045454545	0.424242424	-0.681818182	0.439393939	-1.136363636	0.606060606
	40	-0.666666667	0.303030303	-0.363636364	0.454545455	-0.757575758	0.545454545
	50	-0.515151515	0.196969697	-0.303030303	0.348484848	-0.606060606	0.454545455
	60	-0.363636364	0.090909091	-0.242424242	0.242424242	-0.454545455	0.363636364
	70	-0.121212121	0.015151515	-0.257575758	0.121212121	-0.424242424	0.242424242
	80	0.121212121	-0.060606061	-0.272727273	0	-0.393939394	0.121212121
	90	0.363636364	-0.136363636	-0.287878788	-0.121212121	-0.363636364	0
	%C	Cpu, rect	Cpl, rect	Cpu, curved L.E.	Cpl, curved L.E.	Cpu, curved T.E.	Cpl, curved T.E.
Segment-D	10	-2.090909091	0.575757576	-2.121212121	0.439393939	-2.242424242	0.636363636
	20	-1.696969697	0.454545455	-1.606060606	0.424242424	-1.818181818	0.606060606
	30	-1.303030303	0.333333333	-1.090909091	0.409090909	-1.393939394	0.575757576
	40	-0.909090909	0.212121212	-0.575757576	0.393939394	-0.96969697	0.545454545
	50	-0.696969697	0.212121212	-0.484848485	0.272727273	-0.787878788	0.424242424
	60	-0.484848485	0.212121212	-0.393939394	0.151515152	-0.606060606	0.303030303
	70	-0.424242424	0.151515152	-0.409090909	0.151515152	-0.575757576	0.272727273
	80	-0.363636364	0.090909091	-0.424242424	0.151515152	-0.545454545	0.242424242
	90	-0.303030303	0.03030303	-0.439393939	0.151515152	-0.515151515	0.212121212

Table 7: Calculated Values of Pressure Coefficients at 20˚ Angle of Attack

	%C	Cpu, rect	Cpl, rect	Cpu, curved L.E.	Cpl, curved L.E.	Cpu, curved T.E.	Cpl, curved T.E.
Segment-A	10	-0.31818182	0.621212121	-1.303030303	0.606060606	-1.424242424	0.53030303
	20	-0.33333333	0.515151515	-1.181818182	0.515151515	-1.151515152	0.454545455
	30	-0.34848485	0.409090909	-1.060606061	0.424242424	-0.878787879	0.378787879
	40	-0.36363636	0.303030303	-0.939393939	0.333333333	-0.606060606	0.303030303
	50	-0.34848485	0.151515152	-0.651515152	0.318181818	-0.348484848	0.242424242
	60	-0.33333333	0	-0.363636364	0.303030303	-0.090909091	0.181818182
	70	-0.36363636	-0.07575758	-0.348484848	0.212121212	-0.045454545	0.121212121
	80	-0.39393939	-0.15151515	-0.333333333	0.121212121	0	0.060606061
	90	-0.42424242	-0.22727273	-0.318181818	0.03030303	0.045454545	0
	%C	Cpu, rect	Cpl, rect	Cpu, curved L.E.	Cpl, curved L.E.	Cpu, curved T.E.	Cpl, curved T.E.
Segment-B	10	-0.5	0.393939394	-1.46969697	0.848484848	-1.727272727	0.606060606
	20	-0.48484848	0.363636364	-1.151515152	0.727272727	-1.333333333	0.515151515
	30	-0.46969697	0.333333333	-0.833333333	0.606060606	-0.939393939	0.424242424
	40	-0.45454545	0.303030303	-0.515151515	0.484848485	-0.545454545	0.333333333
	50	-0.45454545	0.227272727	-0.53030303	0.318181818	-0.333333333	0.272727273
	60	-0.45454545	0.151515152	-0.545454545	0.151515152	-0.121212121	0.212121212
	70	-0.43939394	0.075757576	-0.560606061	0.106060606	-0.03030303	0.151515152
	80	-0.42424242	0	-0.575757576	0.060606061	0.060606061	0.090909091
	90	-0.40909091	-0.07575758	-0.590909091	0.015151515	0.151515152	0.03030303
	%C	Cpu, rect	Cpl, rect	Cpu, curved L.E.	Cpl, curved L.E.	Cpu, curved T.E.	Cpl, curved T.E.
Segment-C	10	-0.33333333	0.651515152	-0.318181818	0.424242424	-2.045454545	0.803030303
	20	-0.42424242	0.515151515	-0.393939394	0.424242424	-1.727272727	0.575757576
	30	-0.51515152	0.378787879	-0.46969697	0.424242424	-1.409090909	0.348484848
	40	-0.60606061	0.242424242	-0.545454545	0.424242424	-1.090909091	0.121212121
	50	-0.54545455	0.136363636	-0.560606061	0.318181818	-0.727272727	0.151515152
	60	-0.48484848	0.03030303	-0.575757576	0.212121212	-0.363636364	0.181818182
	70	-0.18181818	-0.09090909	-0.515151515	0.090909091	-0.242424242	0.090909091
	80	0.121212121	-0.21212121	-0.454545455	-0.03030303	-0.121212121	0
	90	0.424242424	-0.33333333	-0.393939394	-0.151515152	0	-0.090909091
	%C	Cpu, rect	Cpl, rect	Cpu, curved L.E.	Cpl, curved L.E.	Cpu, curved T.E.	Cpl, curved T.E.
Segment-D	10	-0.72727273	0.454545455	-0.651515152	0.393939394	-2.409090909	0.909090909
	20	-0.66666667	0.318181818	-0.636363636	0.393939394	-1.848484848	0.696969697
	30	-0.60606061	0.181818182	-0.621212121	0.393939394	-1.287878788	0.484848485
	40	-0.54545455	0.166666667	-0.606060606	0.393939394	-0.727272727	0.272727273
	50	-0.57575758	0.151515152	-0.606060606	0.242424242	-0.545454545	0.257575758
	60	-0.60606061	0.090909091	-0.606060606	0.090909091	-0.363636364	0.242424242
	70	-0.6969697	0.03030303	-0.651515152	0.060606061	-0.303030303	0.196969697
	80	-0.78787879	-0.03030303	-0.696969697	0.03030303	-0.242424242	0.151515152
	90	-0.87878788	0	-0.742424242	0	-0.181818182	0.106060606

Table 8: Calculated Values of Pressure Coefficients at 24° Angle of Attack

	%C	Cpu, rect	Cpl, rect	Cpu, curved L.E.	Cpl, curved L.E.	Cpu, curved T.E.	Cpl, curved T.E.
Segment-A	10	-0.25757576	0.712121212	-1.075757576	0.696969697	-1.212121212	0.772727273
	20	-0.27272727	0.606060606	-0.939393939	0.606060606	-1.060606061	0.666666667
	30	-0.28787879	0.5	-0.803030303	0.515151515	-0.909090909	0.560606061
	40	-0.3030303	0.393939394	-0.666666667	0.424242424	-0.757575758	0.454545455
	50	-0.3030303	0.227272727	-0.590909091	0.393939394	-0.666666667	0.393939394
	60	-0.3030303	0.060606061	-0.515151515	0.363636364	-0.575757576	0.333333333
	70	-0.33333333	-0.015151515	-0.5	0.257575758	-0.515151515	0.287878788
	80	-0.36363636	-0.090909091	-0.484848485	0.151515152	-0.454545455	0.242424242
	90	-0.39393939	-0.166666667	-0.46969697	0.045454545	-0.393939394	0.196969697
	%C	Cpu, rect	Cpl, rect	Cpu, curved L.E.	Cpl, curved L.E.	Cpu, curved T.E.	Cpl, curved T.E.
Segment-B	10	-0.46969697	0.939393939	-0.727272727	0.939393939	-0.878787879	1
	20	-0.42424242	0.757575758	-0.666666667	0.818181818	-0.787878788	0.909090909
	30	-0.37878788	0.575757576	-0.606060606	0.696969697	-0.696969697	0.818181818
	40	-0.33333333	0.393939394	-0.545454545	0.575757576	-0.606060606	0.727272727
	50	-0.36363636	0.318181818	-0.53030303	0.409090909	-0.575757576	0.545454545
	60	-0.39393939	0.242424242	-0.515151515	0.242424242	-0.545454545	0.363636364
	70	-0.34848485	0.121212121	-0.484848485	0.166666667	-0.484848485	0.242424242
	80	-0.3030303	0	-0.454545455	0.090909091	-0.424242424	0.121212121
	90	-0.25757576	-0.121212121	-0.424242424	0.015151515	-0.363636364	0
	%C	Cpu, rect	Cpl, rect	Cpu, curved L.E.	Cpl, curved L.E.	Cpu, curved T.E.	Cpl, curved T.E.
Segment-C	10	-0.25757576	0.787878788	-0.333333333	0.53030303	-0.409090909	0.636363636
	20	-0.33333333	0.636363636	-0.363636364	0.515151515	-0.424242424	0.606060606
	30	-0.40909091	0.484848485	-0.393939394	0.5	-0.439393939	0.575757576
	40	-0.48484848	0.333333333	-0.424242424	0.484848485	-0.454545455	0.545454545
	50	-0.43939394	0.227272727	-0.439393939	0.378787879	-0.454545455	0.424242424
	60	-0.39393939	0.121212121	-0.454545455	0.272727273	-0.454545455	0.303030303
	70	-0.12121212	0	-0.424242424	0.121212121	-0.393939394	0.151515152
	80	0.151515152	-0.121212121	-0.393939394	-0.03030303	-0.333333333	0
	90	0.424242424	-0.242424242	-0.363636364	-0.181818182	-0.272727273	-0.151515152
	%C	Cpu, rect	Cpl, rect	Cpu, curved L.E.	Cpl, curved L.E.	Cpu, curved T.E.	Cpl, curved T.E.
Segment-D	10	-0.63636364	0.545454545	-0.515151515	0.575757576	-0.575757576	0.696969697
	20	-0.57575758	0.409090909	-0.484848485	0.545454545	-0.545454545	0.636363636
	30	-0.51515152	0.272727273	-0.454545455	0.515151515	-0.515151515	0.575757576
	40	-0.45454545	0.242424242	-0.424242424	0.484848485	-0.484848485	0.515151515
	50	-0.48484848	0.212121212	-0.439393939	0.348484848	-0.454545455	0.393939394
	60	-0.51515152	0.106060606	-0.454545455	0.212121212	-0.424242424	0.272727273
	70	-0.60606061	0	-0.5	0.166666667	-0.378787879	0.181818182
	80	-0.6969697	-0.106060606	-0.545454545	0.121212121	-0.333333333	0.090909091
	90	-0.78787879	0	-0.590909091	0.075757576	-0.287878788	0

APPENDIX-II

UNCERTAINTY ANALYSIS

Experimental uncertainty analysis provides a method for predicting the uncertainty of a variable based on its component uncertainties. Furthermore, unless otherwise specified, each of these uncertainties has a confidence level of 95%.

In this experiment, values of pressure coefficients on each surface points are calculated from the respective multi-tube manometer readings obtained during wind tunnel test. Then coefficient of lift and coefficient of drag is estimated from the surface pressure coefficients. As such, the uncertainty started from the initial measurement of manometer height and it propagates with the values of C_P, C_P and $C_{D.}$ The uncertainty in C_P, C_P and C_D can be estimated if their components' individual uncertainty is known.

The equation of C_p can be rewritten in terms of all its components from equation (4.2) as follows:

$$C_p = \frac{\rho_{water} \times g \times \Delta H_{multitubemanometer}}{\frac{1}{2}\rho_{air} \times U_{\infty}^{\;2}} = f\left(g, \rho_{water}, \rho_{air}, U_{\infty}, \Delta H_{multitubemanometer}\right)$$

Due to temperature rise during the experiment, the density of air is changed. So, uncertainty of 0.038 may be assumed as the uncertainty of ρ_{air} (diffence between the values of air density for 35̊C and 40˚C). Uncertainty in the measurement of height from the multi-tube manometer may be assumed 0.002(as the readings vary ±2mm or 0.002m from the actual reading). The uncertainties in other components of C_p can be neglected. So,

$$u_{\rho_{air}} = 0.038$$

$$u_{\Delta H} = 0.002$$

The expected uncertainty in C_p can be estimated from the following formula:

$$U_{C_P} = \sqrt{\left(u_{\rho_{air}} \frac{\partial C_p}{\partial \rho_{air}}\right)^2 + \left(u_{\Delta \mathrm{H}} \frac{\partial C_p}{\partial \Delta \mathrm{H}}\right)^2} \quad \ldots\ldots\ldots\ldots\ldots\ldots\ldots\ldots\ldots\ldots\ldots\ldots\ldots\ldots\ldots\ldots(1)$$

Let us consider the case of segment-A of rectangular wing at 0˚ AOA. There, at 20% chord on the upper surface, ΔH=-30 mm, ρ_{air}=1.145 kg/m^3 and corresponding C_p= -0.910. So, from equation (1),

$$\frac{\partial C_p}{\partial \rho_{air}} = \frac{-C_p}{\rho_{air}{}^2} = \frac{-(-0.910)}{(1.145)^2} = 0.694$$

$$\frac{\partial C_p}{\partial \Delta \mathrm{H}} = \frac{C_p}{\Delta \mathrm{H}} = \frac{(-0.910)}{(-0.03)} = 30.33$$

Putting the above two values and the component uncertainties in equation (1), we get the uncertainty of C_p as:

$$U_{C_p} = \sqrt{(0.694 \times 0.038)^2 + (30.33 \times 0.002)^2} = 0.07$$

So, the uncertainty in C_p is 7%. Similarly from the respective equation of C_L and $C_{D,}$ their corresponding uncertainty can be calculated considering the uncertainty of respective C_p values.